

University of Nebraska - Lincoln

DigitalCommons@University of Nebraska - Lincoln

---

Theses, Dissertations, and Student Research from  
Electrical & Computer Engineering

Electrical & Computer Engineering, Department of

---

12-2018

# Design and Analysis of Binary Driven Coherent M-ary Qam Transmitter for Next Generation Optical Networks

Naji Albakay

University of Nebraska-Lincoln, nalbakay@unomaha.edu

Follow this and additional works at: <http://digitalcommons.unl.edu/elecengtheses>



Part of the [Computer Engineering Commons](#), and the [Other Electrical and Computer Engineering Commons](#)

---

Albakay, Naji, "Design and Analysis of Binary Driven Coherent M-ary Qam Transmitter for Next Generation Optical Networks" (2018). *Theses, Dissertations, and Student Research from Electrical & Computer Engineering*. 99.  
<http://digitalcommons.unl.edu/elecengtheses/99>

This Article is brought to you for free and open access by the Electrical & Computer Engineering, Department of at DigitalCommons@University of Nebraska - Lincoln. It has been accepted for inclusion in Theses, Dissertations, and Student Research from Electrical & Computer Engineering by an authorized administrator of DigitalCommons@University of Nebraska - Lincoln.

DESIGN AND ANALYSIS OF BINARY DRIVEN COHERENT M-ARY  
QAM TRANSMITTER FOR NEXT GENERATION OPTICAL  
NETWORKS

by

Naji Albakay

A DISSERTATION

Presented to the Faculty of  
The Graduate College at the University of Nebraska  
In Partial Fulfillment of Requirements  
For the Degree of Doctor of Philosophy

Major: Computer Engineering

Under the Supervision of Professor Lim Nguyen

Lincoln, Nebraska

December, 2018

# DESIGN AND ANALYSIS OF BINARY DRIVEN COHERENT M-ARY QAM TRANSMITTER FOR NEXT GENERATION OPTICAL NETWORKS

Naji Albakay, PhD

University of Nebraska, 2018

Adviser: Lim Nguyen

This work presents a design for a binary driven optical square M-ary quadrature amplitude modulation (QAM) transmitter for high speed optical networks. The transmitter applies tandem quadrature phase shift keying (QPSK) modulators to eliminate the need for linear broadband amplifiers and high-resolution digital to analog converters (DACs), which are both required by conventional transmitters. The transmitter design could be scaled to any order of square M-ary QAM by simply adding more QPSK modulators in tandem. It also provides a Gray coded symbol constellation, insuring the lowest bit error rate possible during symbol recovery. We also provide the design for the coupling ratios of the optical couplers that take into account the insertion loss of the optical components, in order to generate a proper 16-QAM and 64-QAM symbol constellation with equally-spaced symbols. Additionally, we analyze the impact of coupling ratio errors as well as phase errors on the bit error rate (BER) performance and constellation diagrams.

The performance is tested using the OptiSystem simulation at 50 Gbaud and under presence of additive white Gaussian noise (AWGN), which demonstrated high quality symbol constellation and a BER performance similar to theoretical expectations. For 16-QAM, a BER better than  $10^{-4}$  and power penalty of about 2 dB are achieved for coupling ratio errors less than 10 %, or phase errors within  $\pm 7$  degrees. The 64-QAM transmitter, on the other

hand, demonstrated a BER better than  $10^{-4}$  and power penalty of about 1 dB for coupling ratio errors less than 4%, or phase errors within  $\pm 2$  degrees.

## ACKNOWLEDGMENT

I dedicate this dissertation to the memories of my father who taught me how to work hard and be successful, and to my mother for her tremendous support and unconditional love.

I would like to express my deep and sincere appreciation to my dissertation advisor Professor Lim Nguyen. This work would not have been possible without his tremendous support, encouragement, and valuable feedback and recommendations.

I am also grateful to my examination committee Professor Hamid Sharif, Professor Yaoqing Yang, and Professor Mahboub Baccouch for the time they dedicated to review my dissertation. A special thanks to Professor Hamid Sharif for his valuable advice and guidance during the period of my graduate program.

I would like to take this opportunity to thank the University of Nebraska-Lincoln for sponsoring me during my graduate study and providing me with this unique and wonderful experience. Finally, words are inadequate in offering my greatest thanks and appreciation to my family and friends for their support, encouragement, and good wishes.

## TABLE OF CONTENTS

CHAPTER 1 INTRODUCTION .....	1
1.1. Introduction .....	1
1.2. Background .....	1
1.3. Advantages of coherent optical transmission.....	4
1.4. Commercially available coherent optical systems .....	5
1.5. The need for coherent M-ary QAM transmission .....	6
1.6. State of the art optical modulation format.....	8
1.6.1. Polarization division multiplexing.....	9
1.6.2. Multi-carrier modulation .....	10
1.7. Conclusion.....	17
CHAPTER 2 MAIN COMPONENTS IN COHERENT OPTICAL TRANSMISSION SYSTEM.....	18
2.1. Introduction .....	18
2.2. Optical transmitter.....	19
2.2.1. Laser source.....	19
2.2.2. Modulator .....	22
2.3. Gray coding.....	32
2.4. Commercial MZM.....	33
2.4.1. MZM errors due to arm's length mismatch.....	34
2.4.2. MZM errors due to drift in the operating point .....	35
2.5. Optical fiber.....	37
2.5.1. Attenuation .....	38
2.5.2. Chromatic dispersion (CD).....	39
2.5.3. Polarization mode dispersion (PMD) .....	40
2.6. Coherent optical receiver .....	41
2.6.1. Heterodyne detector.....	42
2.6.2. Analog to digital converter (ADCs) .....	43
2.6.3. Digital signal processing (DSP) .....	43
2.7. Conclusion.....	44

CHAPTER 3: PROPOSED SCALABLE AND GRAY CODED OPTICAL M-ARY QAM TRANSMITTER DRIVEN BY BINARY ELECTRICAL SIGNALS .....	46
3.1. Introduction .....	46
3.2. Operating principles for 16-QAM transmitter .....	47
3.3. Generation of a Gray-coded 16-QAM constellation .....	50
3.4. Alternative configuration for a Gray-coded 16-QAM transmitter .....	52
3.5. Operating principles for 64-QAM transmitter .....	54
3.6. Conclusion.....	57
CHAPTER 4: DESIGNING THE COUPLING RATIOS FOR PROPER CONSTELLATIONS AND ANALYZING THE IMPACT OF COUPLING AND PHASE ERRORS .....	58
4.1. Introduction .....	58
4.2. Designing the coupling ratio for 16-QAM transmitter.....	58
4.3. Effect of coupling ratio error.....	60
4.4. Effect of phase errors .....	63
4.5. Designing the coupling ratio for 64-QAM transmitter.....	65
4.6. Effect of coupling ratios errors.....	68
4.7. Effect of phase errors on the 64-QAM transmitter .....	73
4.8. Conclusion.....	75
CHAPTER 5: SIMULATION SETUP AND RESULTS .....	76
5.1. Introduction .....	76
5.2. Simulation setup for 16-QAM transmitter .....	76
5.2.1. 16-QAM transmitter performance .....	79
5.2.2. Impact of coupling ratio errors on 16-QAM performance .....	81
5.2.3. Impact of phase errors on 16-QAM performance.....	84
5.3. 64-QAM simulation setup.....	86
5.3.1. 64-QAM transmitter performance .....	86
5.3.2. Effect of coupling ratio errors on 64-QAM performance.....	89
5.2.3. Effect of phase errors on 64-QAM performance .....	92
5.4. Conclusion.....	95
CHAPTER 6: CONCLUSION .....	96

REFERENCES ..... 100

## TABLE OF FIGURES

Fig.1. 1: (a) PDM-QPSK transceiver [36]; (b) QPSK constellation diagram.....	5
Fig.1. 2: Total traffic demand and available communication systems per year for North Americans core networks [52].....	7
Fig.1. 3: Orthogonal PDM wave [56]. .....	9
Fig.1. 4: (a) Super channel; (b) O-OFDM channel. ....	11
Fig.1. 5: Configuration of single I/Q M-ary QAM transmitter.....	14
Fig.1. 6: (a) Block diagram for TIQ scheme [79]; (b) Block diagram for RN-MZI scheme [80].....	15
Fig.1. 7: (a) Symbol transitions for TIQ scheme [79]; (b) Symbol transitions for RN-MZI scheme [80].....	16
Fig. 2. 1: Structure of coherent optical communication system. ....	18
Fig. 2. 2: Optical resonator .....	20
Fig. 2. 3: Intensity modulation.....	23
Fig. 2. 4: MZI configuration .....	24
Fig. 2. 5: Principles of phase modulation .....	26
Fig. 2. 6: (a) MZI with phase modulator embedded in one arm. ....	27
Fig. 2. 7: (a) MZI with phase modulator embedded in one arm. ....	29
Fig. 2. 9: (a) signal constellation at point A; (b) signal constellation at point B; (c) signal constellation at point C; (d) signal constellation at point D. ....	31
Fig. 2. 8: I/Q modulator .....	31

Fig. 2. 10: (a) Gray coded QPSK constellation; (b) Non-Gray coded QPSK constellation. .....	32
Fig. 2. 11: Commercial MZM.....	33
Fig. 2. 12: MZM transfer function.....	34
Fig. 2. 13: Bias control based on change in output optical power.....	35
Fig. 2. 14: Comparison between the power of first harmonic (dotted curve) and the second harmonic of the output optical power [93]......	36
Fig. 2. 15: Optical fiber structure.....	37
Fig. 2. 16: Attenuation profile for standard single mode fiber [94]......	38
Fig. 2. 17: Pulse spreading due to chromatic dispersion (CD) [95]......	39
Fig. 2. 18: Maximum allowable distance versus bit rate [96]......	40
Fig. 2. 19: Polarization mode dispersion (PMD) [98]. .....	41
Fig. 2. 20: Heterodyne detector.....	42
Fig. 2. 21: DSP block diagram.....	44
Fig. 3. 1: Optical circuit diagram for 16-QAM.....	47
Fig. 3.2: I/Q modulator. ....	48
Fig. 3.3: (a) BPSK 1; (b) BPSK 2; (c) BPSK 3; (d) QPSK signal.....	48
Fig. 3.4: (a) 4-QAM shifted to the first quadrant; (b) Non-Gray coded 16-QAM .....	49
Fig. 3.5: (a) 16-QAM precoder; (b) Gray coded 16-QAM.....	51
Fig. 3. 6: Alternative configuration for 16-QAM transmitter.....	52
Fig. 3. 7: (a) Output of QPSK1; (b) Offset constellation for D3, D4 the same; (c) Offset constellation for D3, D4 different; (d) Gray coded 16-QAM output of QPSK2.....	53

Fig. 3. 8: Optical circuit diagram for 64-QAM.....	54
Fig. 3. 9: Non-Gray coded 64-QAM.....	55
Fig. 3. 10: (a) 64-QAM precoder; (b) Gray coded 64-QAM constellation.....	56
Fig. 3.11: Optical circuit diagram for 256-QAM.....	57
Fig. 4. 1: Optical circuit diagram for 16-QAM optical transmitter. ....	58
Fig. 4. 2: (a) 4-QAM; (b) 4-QAM shifted to the first quadrant; (c) 16-QAM. ....	59
Fig. 4. 3: Effect of 10% errors in S1 on: (a) 4-QAM; (b) 4-QAM shifted to the first quadrant; (c) 16-QAM. ....	61
Fig. 4. 4: Rate of change of $P2/P3$ with $\alpha1$ .....	63
Fig. 4. 5: Optical circuit diagram for 16-QAM optical transmitter. ....	64
Fig. 4. 6: (a) shifted 4-QAM for $\Delta\emptyset16QAM = 5 \text{ degrees.}$ ; (b) 16-QAM for $\Delta\emptyset16QAM = 5 \text{ degrees}$ .....	64
Fig. 4. 7: Optical circuit diagram for 64-QAM transmitter. ....	65
Fig. 4. 8: (a) 4-QAM; (b) 4-QAM shifted to the first quadrant; (c) 16-QAM; (d) 16-QAM shifted to the first quadrant; (e) 64-QAM.....	66
Fig. 4. 9: Effect of 10% error in S1 on: (a) 4-QAM; (b) 4-QAM shifted to the first quadrant; (c) 16-QAM; (d) 16-QAM shifted to the first quadrant; (e) 64-QAM. ....	69
Fig. 4. 10: 3D plots of (a) change in $\partial(P2/P3)/\partial\alpha1\alpha2$ with $\alpha1\alpha2$ ;(b) change in $\partial(P4/P5)/\partial\alpha1\alpha2$ with $\alpha1\alpha2$ . ....	73
Fig. 4. 11: Effect of $\Delta\emptyset64 - QAM = 5 \text{ degrees}$ on: (a) shifted 16-QAM; (b) 64-QAM. (c) 64-QAM for $\Delta\emptyset16 - QAM = \Delta\emptyset64 - QAM = 5 \text{ degrees}$ .....	74
Fig. 4. 12: Optical circuit diagram for 64-QAM transmitter. ....	74

Fig. 4. 13: Effect of $\Delta\theta_{16QAM} = 5$ degrees on: (a) shifted 4-QAM; (b) 16-QAM at point C; (c) 64-QAM. ....	75
Fig. 5. 1: Simulation setup for 16-QAM. ....	76
Fig. 5. 2: QPSK implementation in OptiSystem. ....	77
Fig. 5. 3: Demodulator implementation in OptiSystem. ....	78
Fig. 5. 4: (a) Constellation for proper 16-QAM. ....	79
Fig. 5. 5: (a) Eye diagram for I signal; (b) Eye diagram for Q signal. ....	80
Fig. 5. 6: Symbol transitions. ....	80
Fig. 5. 7: BER performance. ....	81
Fig. 5. 8: (a) Symbol constellation at 16/84 coupling ratio; (b) Symbol constellation at 36/64 coupling ratio. ....	82
Fig. 5. 9: BER performance. ....	83
Fig. 5. 10: BER versus coupling ratio. ....	83
Fig. 5. 11: (a) Symbol constellation at 16/84 coupling ratio; (b) Symbol constellation at 36/64 coupling ratio. ....	84
Fig. 5. 12: BER versus phase error. ....	85
Fig. 5. 13: BER performance. ....	85
Fig. 5. 14: Simulation setup for 64-QAM transmitter. ....	86
Fig. 5. 15: 64-QAM constellation. ....	88
Fig. 5.16: I and Q eye diagrams. ....	88
Fig. 5. 17: BER performance. ....	89

Fig. 5. 18: Symbol constellation for (a) $S1=12/88$ , $S2=47/53$ ; (b) $S1=13.5/86.5$ , $S2=43.1/56.9$ .....	90
Fig. 5. 19: BER performance vs. $S1$ and $S2$ ; inset: coupling ratios for $BER < 10^{-4}$ .....	91
Fig. 5. 20: 64-QAM constellation for: (a) No phase errors; (b) $\Delta\phi_{16} - QAM =$ $5 \text{ degrees}$ ; (c) $\Delta\phi_{64} - QAM = 5 \text{ degree}$ ; (d) $\Delta\phi_{16} - QAM = \Delta\phi_{64} - QAM =$ $5 \text{ degrees}$ .....	93
Fig. 5. 21: BER performance vs. $\Delta\phi_{16} - QAM$ and $\Delta\phi_{64} - QAM$ ; inset: Phase errors for $BER < 10^{-4}$ .....	94
Fig. 5. 22: BER performance. ....	94

## ACRONYMS LIST

ADCs: analog to digital converters  
AWGN: additive white Gaussian noise  
BER: bit error rate  
BPSK: binary phase shift keying  
CD: Chromatic dispersion  
DACs: digital to analog converters  
DD: direct detection  
DFB: distributed feedback  
DFT: discrete Fourier transform  
DGD: differential group delay  
DQPSK: Differential quadrature phase-shift keying  
DSP: digital signal processing  
EDFAs: erbium doped fiber amplifiers  
FEC: forward error correction  
FFT: fast Fourier transform  
FSR: free spectral range  
I/Q: in-phase/quadrature modulator  
IM: intensity modulation  
ISI: inter-symbol interference  
ITU: International Telecommunication Union  
LO: local oscillator  
MZI: Mach-Zehnder interferometer  
MZM: Mach-Zehnder modulator  
O-OFDM: optical orthogonal frequency division multiplexing

OOK: ON/OFF keying  
PAPR: peak to average power ratio  
PBC: polarization beam combiner  
PBS: polarization beam splitter  
PDM: polarization division multiplexing  
PMD: polarization mode dispersion  
PSK: phase shift keying  
QPSK: quadrature phase shift keying  
QAM: quadrature amplitude modulation  
SE: spectral efficiency  
TC: tunable optical splitters/couplers  
TIA: transimpedance amplifier  
TIQ: tandem in-phase/quadrature modulators  
VV: Viterbi-Viterbi  
WDM: wavelength division multiplexing

# CHAPTER 1 INTRODUCTION

## 1.1. Introduction

Coherent optical transmission refers to optical communication systems that apply higher order modulation format at the transmitter side and coherent detection using local oscillator laser and digital signal processing (DSP) at the receiver side. Using higher order modulation format such as M-ary quadrature amplitude modulation (QAM) would allow better utilization of fiber bandwidth thus reducing the cost per bit of transmitted information. This chapter reviews the development of coherent optical transmission and its advantages. It also describes the commercially available coherent optical transmitters and summarizes the state of the art optical modulation formats used in coherent optical communication.

## 1.2. Background

DeLange introduced the first coherent optical communication system that applies phase modulation and heterodyne detection in the early 1970's [1]. His system did not receive a great deal of attention owing to the frequency instability and phase noise associated with the large linewidth semiconductor lasers. In addition, a simpler optical communication system based on intensity modulation (IM) of the semiconductor laser and direct detection (DD) using photo detector was the main stream at the time.

In the early 1980's, Okoshi and Kikuchi introduced a frequency stabilization technique for the semiconductor lasers that mitigated the frequency drifting and reduced the linewidth to

less than 10 MHz [2-4]. In [5], a comparison was made between a simple coherent optical system based on phase shift keying (PSK) and optical systems that are based on IM-DD. It was shown that the coherent system improves the receiver sensitivity by 6 dB and in return extends the transmission distance. This was a big motivation of research and development in coherent optical communications before the emergence of erbium doped fiber amplifiers (EDFAs).

In the 1990's, the invention of EDFAs interrupted the research in coherent optical transmission since the power-limited transmission distance of the IM-DD system could be extended. Furthermore, EDFA-based IM-DD system incorporated wavelength division multiplexing (WDM) to increase the transmission capacity of single-mode fiber [6]. In 2002, the International Telecommunication Union (ITU) introduced ITU-T G.694.1 WDM recommendation which allows 80 optical carriers spaced by 50 GHz to be simultaneously transmitted over a single fiber. Each optical carrier would employ IM-DD at a data rate of 10 Gbps per channel, employing ON/OFF keying (OOK) and achieving an aggregated capacity of 800 Gbps (80-channel  $\times$  10 Gbps) over single fiber [7].

In early 2000's, many research efforts began to focus on implementing IM-DD at data rates higher than 10 Gbps per WDM channel [8-10]. This approach was not viable because IM signal is highly susceptible to optical channel impairments such as chromatic dispersion (CD) and polarization mode dispersion (PMD) [11, 12] that worsen with shorter optical pulses. In addition, IM-DD-based systems at data rates more than 10 Gbps per channel have proven to be nonlinear and power inefficient, making it unsuitable to employ

electronic compensation for optical channel impairments. Consequently, coherent optical transmission has received renewed attention as the technology of choice.

The rebirth of coherent optical transmission started with the development of coherent optical system based on optical differential quadrature phase-shift keying (DQPSK) [13, 14]. This scheme increased the bit rate by 4- fold compared to IM-DD systems, achieving 40 Gbps at 20 Gbaud per WDM channel. Between 2005 and 2010, the research efforts focused on applying DSP techniques and polarization division multiplexing to further increase the data rate of coherent optical systems to 100 Gbps[15-17].

In 2010, the first coherent optical system that is based on orthogonal polarization division multiplexing (PDM) and QPSK became commercially available [18]. The system provides 100 Gbps at 25 Gbaud and applies DSP extensively for bit coding [19-22], laser source non-linearity compensation [22-25], fiber non-linearity pre-compensation [26], pulse shaping, carrier phase and frequency estimation, as well as CD and PMD compensation [27-30]. The 100 Gbps PDM-QPSK coherent optical system by far has been the highest data rate optical system available in the market.

Currently, coherent optical communication systems with data rates beyond 100 Gbps per optical channel are under investigation. The goal is to achieve 400 Gbps per WDM channel using higher order QAM modulation formats such as 16-QAM and 64-QAM. There are several publications that reported 400 Gbps using 16-QAM [31-33] and an even higher data rate using 64-QAM at 50 Gbaud [34]. Yet none of these solutions is commercially available.

### **1.3. Advantages of coherent optical transmission**

Coherent optical transmission is the key to achieve high data rates that are required for next generation optical networks. It provides high spectral efficiency (SE) and long transmission distance. It applies digital signal processors (DSP) to compensate for fiber transmission impairments such as CD and PMD, which in return eliminates the need for dispersion compensation modules and allows robust performance over different types of glass optical fiber. Coherent optical transmission allows higher network flexibility by supporting different baud rates and modulation formats per single optical carrier leading to increment in SE and reduction of the cost per bit of transmitted information. Compared to the widely used IM-DD systems, coherent optical systems provide the following advantages:

1. Concurrent modulation of carrier amplitude and phase using higher order modulation format would allow increases in the transmission capacity as well as SE. For instance, applying 16-QAM and 64-QAM would increase the SE and thus the capacity by 4-fold and 6-fold as compared to IM-DD.
2. Thanks to the DSP capability, coherent optical systems allow increase of receiver sensitivity by 15 dB to 20 dB [35] and therefore increasing the transmission distance by about 100 km over the C band while mitigating the need for EDFA.
3. Provide spectral shaping functionality that enables the usage of flexible grid systems and allows rejection of interference from adjacent channels. This increases the spectral efficiency by placing the optical carriers closer to one another within the transmission band.

4. Provide flexible programmable design that can support multiple modulation formats, therefore enabling the user to choose from a variety of data rates.
5. Apply DSP to compensate for the CD and PMD and improve system tolerance to polarization dependent losses. This eliminates the need for dispersion compensation modules and increases the data rate by transmitting information over multiple polarization states using PDM.

#### 1.4. Commercially available coherent optical systems

Commercially available coherent optical systems are based on PDM and 4-QAM, or PDM-QPSK as shown in Fig. 1.1a. The input digital data are split into 4 parallel binary streams and converted to multilevel electrical signals using high-speed digital to analog converters (DACs). The two pairs of electrical signals modulates the two orthogonal polarization states (X and Y) of the optical carrier. The electrical signal levels are adjusted

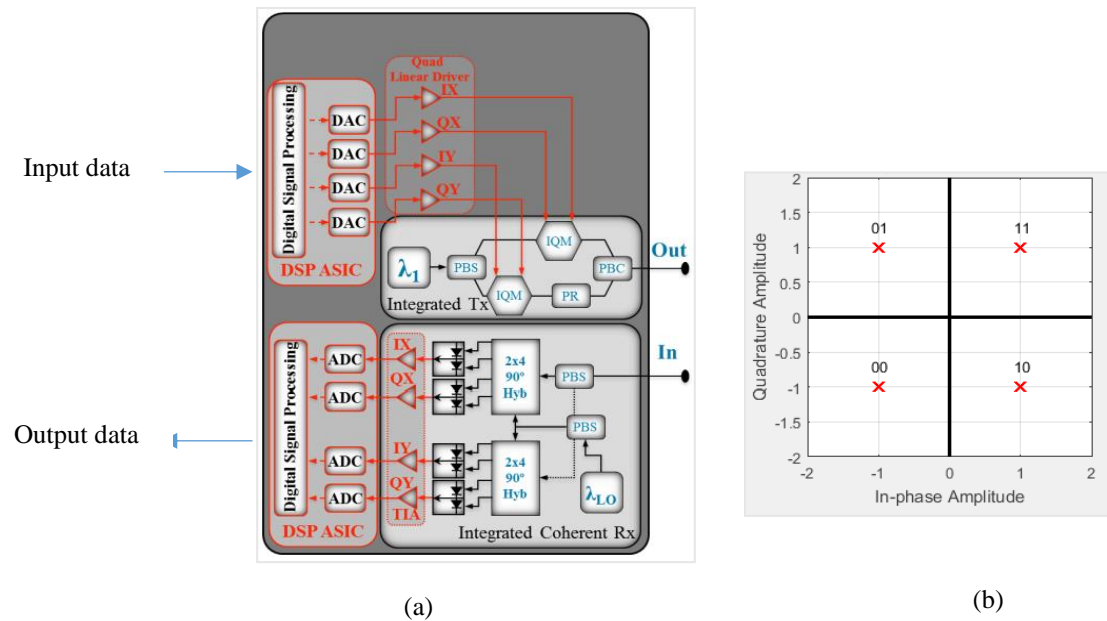


Fig.1. 1: (a) PDM-QPSK transceiver [36]; (b) QPSK constellation diagram.

to the values desired by the two in-phase/quadrature modulators (I/Q) using linear driving amplifiers. The two I/Q modulators modulate a narrow linewidth laser generating QPSK signals per each X Y polarization state as represented by the constellation diagram shown in Fig. 1.1b. The polarization beam combiner (PBC) combines the two QPSK polarized waves to generate PDM-QPSK signal at the output fiber. The DSP block at the transmitter side applies multiple algorithms for bit coding [36], I/Q non-linearity compensation [37, 38], non-linearity pre-compensation [39-41], and pulse shaping [42-45]. The signal is then amplified and sent through the optical fiber to the coherent receiver. At the receiver, the optical signal is split into two polarized signals X and Y using the polarization beam splitter (PBS) as shown in Fig. 1.1a. The 90° optical hybrids combine each signal with the polarization matched optical signal from the narrow linewidth local oscillator laser and converted to electrical domain using balanced I/Q photo detectors. The electrical signals are amplified and sampled into 4 digital bit streams via high speed analog to digital converters (ADCs). The DSP at the receiving end performs carrier phase and frequency estimation as well as CD and PMD compensation [46-51].

Operating the DACs/ADCs at a symbol rate of 25 Gbaud, the above configuration would be able to provide a data rate of 100 Gbps per WDM channel achieving an aggregated capacity of 8 Tbps over standard WDM. The coherent optical link described above is the highest speed link available in the market.

### **1.5. The need for coherent M-ary QAM transmission**

The Internet traffic demand has been growing at a rate of 25% per year owing to the emergence of high data rate solutions including high definition 3D TV, video conferencing,

online gaming, cloud computing, and big data [52-55]. Fig. 1.2 shows the traffic model developed by Bell Lab for North American core networks. The model predicts the total traffic demand over the last three decades and some forecasts through 2020.

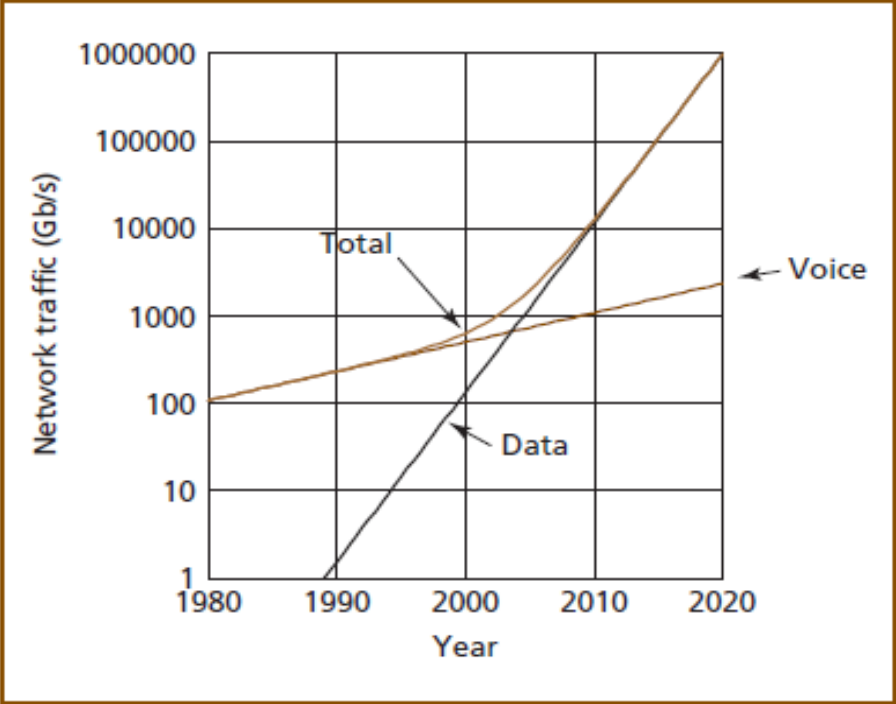


Fig.1. 2: Total traffic demand and available communication systems per year for North Americans core networks [52].

As illustrated, the current traffic demand in North American core networks is about 200 Tbps and is projected to increase 5-fold by 2020. However, the maximum achievable data rate over standard single-mode fiber is 8 Tbps [56]. Consequently, accommodating the current traffic demand for North American core networks would require about 25 WDM fiber links with capacity of 8 Tbps each. Around 125 WDM such links would be required to accommodate the 1000 Tbps anticipated for 2020. This huge number of WDM links

would result in high capital expenditure costs (CapEx) and thus increase the cost per bit of the optical transmission.

To increase the capacity of the core networks while reducing the number of WDM links, and thereby reducing the CapEx, coherent optical systems that employ higher modulation format such as 16-QAM and 64-QAM should be employed to increase SE. 16-QAM and 64-QAM would increase the SE and thus the capacity by 2-fold and 3-fold respectively, as compared to QPSK, and thereby decrease the number of required WDM links by the same factor.

### 1.6. State of the art optical modulation format

The data rate of an optical communication link is determined by the number of polarization states ( $\rho$ ), number of optical carriers ( $N$ ), symbol rate per carrier ( $R$ ), and the number of distinct binary pulses per symbol ( $M$ ) as follows:

$$\text{data rate} = \rho \times N \times R \times \log_2(M) \quad (1.1)$$

Also, the  $SE$  is defined as the number of bit per second per Hz:

$$SE = \frac{\text{data rate}}{BW} = \frac{\rho \times N \times R \times \log_2(M)}{BW} \quad (1.2)$$

where  $BW$  is the transmission bandwidth in Hertz.

Equations (1.1) and (1.2) suggest that a high data rate and thus high SE could be achieved using several approaches:

- Increasing  $\rho$  using PDM
- Increasing  $N$  using multi-carrier modulation techniques

- Increasing  $M$  using M-ary QAM

The data rate can be increased by combining two or more of the above-mentioned techniques. The following subsections provide a quick overview of each possible approach along with the recent research efforts.

### 1.6.1. Polarization division multiplexing

PDM is a technique that allows simultaneous transmission of multiple independent data streams over the same wavelength using different states of polarization for each stream [57]. At the receiving end, the multiple polarization channels are separated and detected independently. The most widely used form of PDM is orthogonal PDM where the horizontally and vertically polarized optical waves are independently modulated as shown in Fig. 1.3. Some investigations have been carried out to explore PDM with more than two states of polarization [57-59]. In [58], experimental OOK link using four states of polarization has been demonstrated at 32 Gbaud, achieving an aggregated data rate of 128

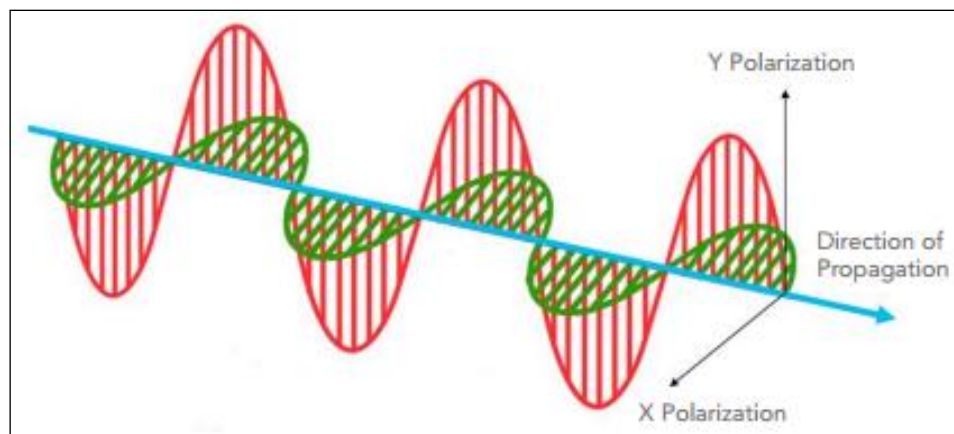


Fig.1. 3: Orthogonal PDM wave [56].

Gbps over distance of 2 km. Currently, the minimum achievable polarization multiplexing angle in research literature is  $23^\circ$  which means that fifteen different data streams with

different polarizations could potentially be sent simultaneously over the same wavelength [58]. The lab experiments, however, have been carried out with only four states of polarization owing to the complexity associated with the simultaneous detection of multiple states of polarization at the receiving end due to the cross-talk interference [60, 61]. Also, the asymmetries in circular geometry and stresses in the fiber core lead to a polarization dependent refractive index which produces PMD [62]. PMD causes a change in the state of polarization as the optical signal propagates down the fiber leading to a degradation of the optical link performance especially for long distances. Owing to these limitations, PDM is limited in practice to orthogonal PDM.

### **1.6.2. Multi-carrier modulation**

Multi-carrier modulation is the process of transmitting user data by dividing it into bit streams and using them to modulate several carriers [63]. In optical communication, there are two main categories of multicarrier modulation: super channel and optical orthogonal frequency division multiplexing O-OFDM [64].

#### **1.6.2.1. Super channel**

Super channel is a form of dense WDM that allows multiple carriers with small and non-overlapping frequency spacing to be transmitted simultaneously over a single channel as illustrated in Fig. 1.4a. As can be seen, five optical carriers with frequency spacing of 10 GHz are squeezed into a 50 GHz channel. Each carrier can be modulated using simple

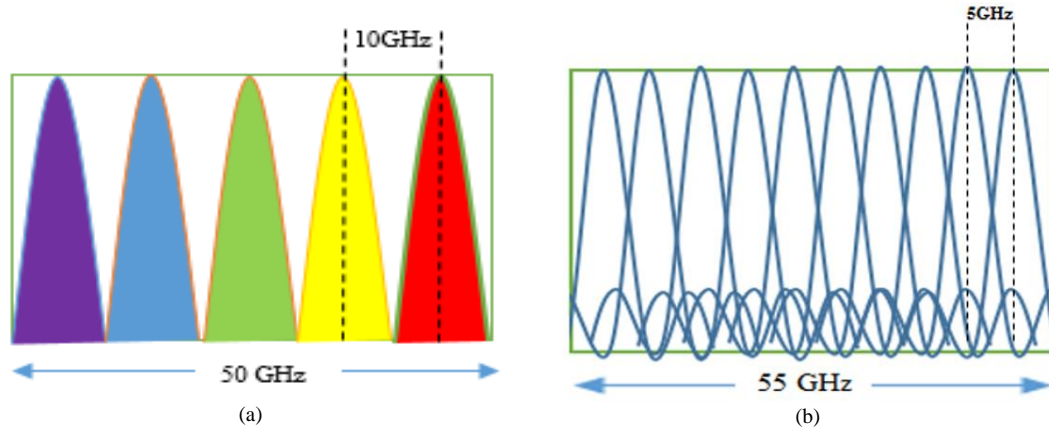


Fig.1. 4: (a) Super channel; (b) O-OFDM channel.

modulation format such as OOK which in return allows simple demodulation process by simply applying DD. To further increase the super channel data rate while operating the DACs/ADCs at relatively lower symbol rate, higher order modulation format such as PDM-M-ary QAM have been applied per sub-carrier [65]. In [66], a data rate of 400 Gbps was achieved using a super channel comprised of four sub-carriers that occupy only 150 GHz of bandwidth at 37.5 GHz sub-carrier spacing. Each carrier is modulated using the commercially available 100 Gbps PDM-QPSK modulator achieving a total data rate of 400 Gbps. In [67], four sub-channels modulated using PDM-16 QAM and occupying 100 GHz of bandwidth achieved an aggregated data rate of 800 Gbps.

The main advantage of super channel is to increase the SE of the optical link as well as reduce the demand on the DACs/ADCs by operating each sub-channel at a lower data rate compared to the channel bandwidth [68]. The main limitations on the other hand are the large number of modulators and demodulators required for each super channel as well as the cross-channel interference at the receiver side which increases with decreasing channel spacing [69].

### **1.6.2.2. Optical orthogonal frequency division multiplexing**

O-OFDM is a multi-carrier modulation technique that overlaps multiple orthogonal carriers within the channel bandwidth to increase the SE [70]. As can be seen in Fig. 1.4b, 10 overlapped sub-channels, each with 10 GHz bandwidth, can be squeezed into 55 GHz channels, effectively doubling the spectrum efficiency obtained with super channel. The orthogonality property of O-OFDM signals enable demodulation without co-channel interference. It is worthwhile to mention that the O-OFDM is different from the electrical OFDM in the way the signal is generated. While electrical OFDM signal is generated and processed using discrete Fourier transform (DFT) and fast Fourier transform (FFT) [71], O-OFDM typically employs multiple laser sources, photo detectors, and filters to generate and detect the signal in order to circumvent the speed limitation of the DACs/ADCs [72]. The distinct advantage of O-OFDM is the high spectrum efficiency owing to the orthogonality between the adjacent channels [73]. It can facilitate resource allocation and provide dynamic data rates based on the traffic demand as each carrier can be modulated with different modulation format as needed [74].

In [72], a 275 Gbps O-OFDM signal based on eleven sub-carriers each applies IMDD at 25 Gbaud was demonstrated. To further increase the O-OFDM system capacity while operating the DACs/ADCs at a lower symbol rate, higher order modulation format such as PDM-M-ary QAM have been applied per O-OFDM sub-carrier. In [74], error free 80 Gbps based on four O-OFDM sub-carriers, each modulated using PDM-QPSK, was proposed.

Even though many experiments have been conducted to evaluate the performance of O-OFDM, only a few can be practically realized due to various limitations associated with digital signal processor capability [73]. In addition, the modulation and demodulation process in O-OFDM is complicated as it requires multiple laser sources, photo detectors, and filters [70]. Also, high accuracy in the phase and frequency of the receiver local oscillator laser is required because any carrier mismatch would result in degradation of the system performance [72]. The peak to average power ratio (PAPR) along with the challenges facing real time implementation at high data rate have been major drawbacks of O-OFDM systems [70, 71].

### **1.6.3. M-ary quadrature amplitude modulation**

M-ary QAM is a single carrier modulation technique that allows multiple bits to be transmitted simultaneously by mapping them into one symbol [75]. The advantages of single carrier M-ary QAM include simplicity, easy wavelength allocation, more compactness, low power dissipation, and it can be implemented in real time [76, 77]. Optical M-ary QAM signal can be generated by modulating a single narrow linewidth cavity laser using single or multiple I/Q modulators as described below.

#### **1.6.3.1. M-ary QAM generation using single QPSK modulator**

In this configuration, a QPSK modulator is used to modulate a narrowband optical laser in quadrature phases using multilevel electrical signals from high-speed DACs and driving amplifiers as shown in Fig. 1.5. In [75], 256.8 Gbps data rate and spectral efficiency of 12 bit/s/Hz was achieved using a single carrier at 21.4 Gbaud by applying PDM-64 QAM

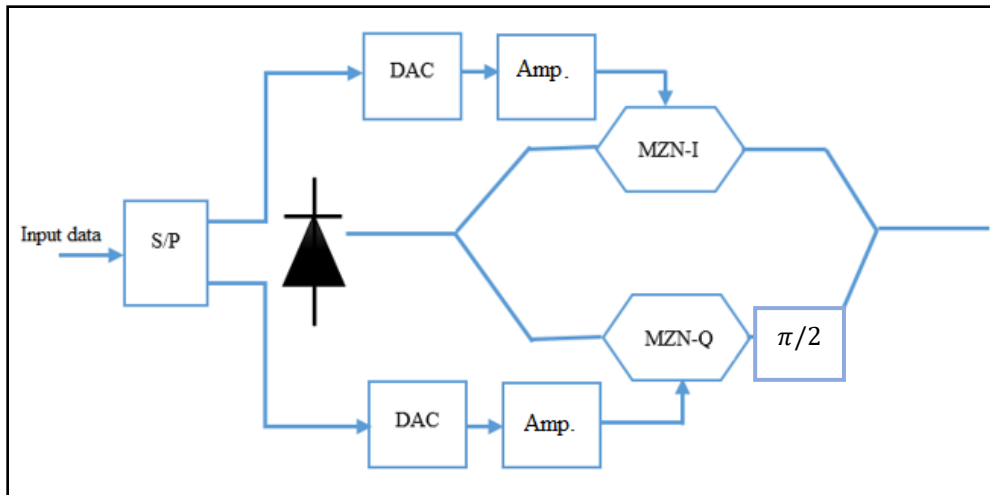


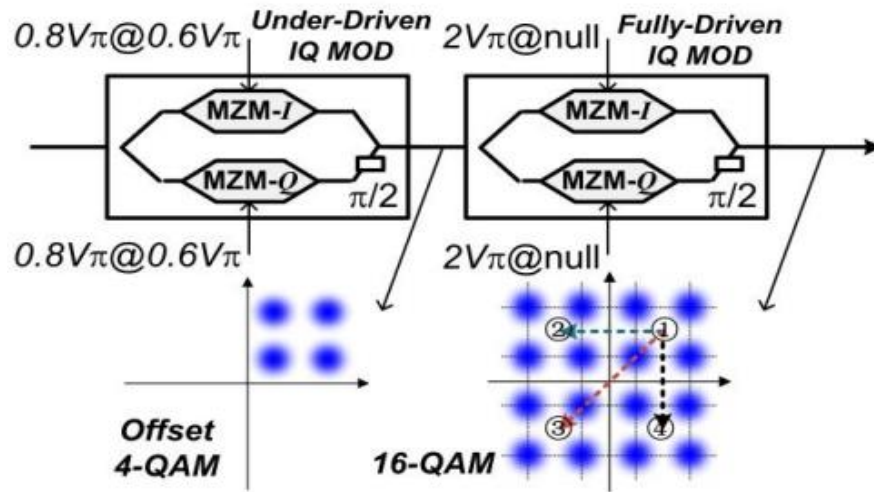
Fig.1. 5: Configuration of single I/Q M-ary QAM transmitter.

using a single I/Q optical modulator driven by eight-level electrical waveforms from a high-power DAC. In [76], the author demonstrates 400 Gbps transmission by means of dual-polarization I/Q modulator on a single carrier using 16-QAM at 56 Gbaud, and 64-QAM at 38 Gbaud, achieving spectral efficiency of 7 bit/s/Hz and 10 bit/s/Hz respectively. The main advantage of this approach is the simplicity in optical domain as only a single I/Q modulator is required. The main drawback is the high-resolution required by the DACs to cope with the nonlinearities associated with the Mach-Zehnder modulator (MZM), as well as the high power driving amplifiers in order to generate high quality symbol constellations and eye diagrams [77]

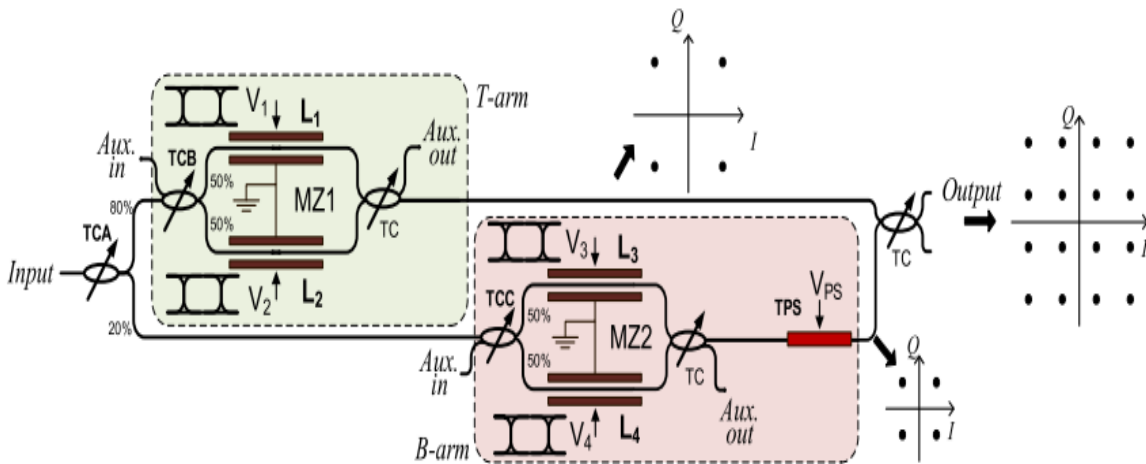
### 1.6.3.2. M-ary QAM using multiple I/Q modulators driven by binary electrical signals

This configuration overcomes the nonlinearities and DAC/amplifier limitations by employing multiple I/Q modulators that are driven by binary electrical signals [78-81]. Single carrier with multiple I/Q modulators transmitters are proposed in different configurations [79, 80] as shown in Fig. 1.6. The tandem I/Q (TIQ) modulator proposed in

[79] is shown in Fig. 1.6a. As illustrated, two I/Q modulators in tandem are used to generate 16-QAM signal. The first I/Q modulator is operated to generate 4-QAM constellation in the first quadrant. The second I/Q modulator rotates the offset 4-QAM to the four-quadrants generating 16-QAM as shown. In [80], reconfigurable nested Mach-Zehnder



(a)



(b)

Fig.1. 6: (a) Block diagram for TIQ scheme [79]; (b) Block diagram for RN-MZI scheme [80].

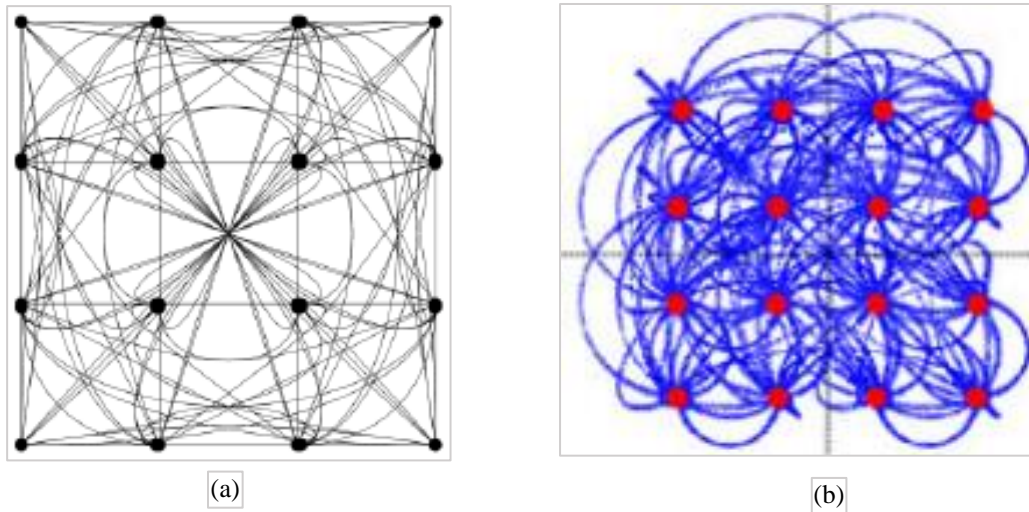


Fig.1. 7: (a) Symbol transitions for TIQ scheme [79]; (b) Symbol transitions for RN-MZI scheme [80].

interferometer (RN-MZI) is proposed with the configuration shown in Fig. 1.6b. As can be seen, 16-QAM modulator is implemented using four phase modulators (L1-L4) embedded in a double-nested MZI, and tunable optical splitters/couplers (TC). The two QPSK signals generated in the T-and B-arms in Fig. 1.6b combine constructively or destructively, depending on the splitting ratio of the TC as well as the applied binary signals, generating the 16-QAM constellation as shown. Fig. 1.7 shows the symbol transition diagrams for TIQ and RN-MZI transmitters. The diagrams show the schemes are susceptible to intersymbol interference (ISI) due to the nonlinear phase transitions between the symbols, reflecting the vulnerability of the generated 16-QAM signals to CD and PMD [81]. The two configurations are not easily scalable to higher-order modulation formats and also generate non-Gray coded symbol constellations resulting in high bit error rates from symbol errors.

## 1.7. Conclusion

Coherent optical systems apply higher order modulation format to increase optical systems capacity. The highest data rate coherent optical links available in the market can achieve 100 Gbps over single wavelength using PDM and QPSK. There is a variety of modulation formats that would allow higher data rate such as O-OFDM, super channel, and optical QAM. . However, optical QAM transmitters based on multiple QPSK modulators that are driven by binary electrical signals appears to be the most promising as they eliminate the need for high speed DAC and driving amplifiers associated with single QPSK modulator that is driven by multilevel electrical signals.

## CHAPTER 2 MAIN COMPONENTS IN COHERENT OPTICAL TRANSMISSION SYSTEM

### 2.1. Introduction

Similar to all communication systems, coherent optical systems comprise three basic components: transmitter, transmission media, and receiver as shown in Fig. 2.1. The transmitter modulates the optical carrier with input data and sends it over the transmission media. The transmission media is a glass optical fiber that provides the connection between the transmitter and the receiver. At the receiver, the signal is demodulated and converted to electrical domain by means of balanced coherent detection. The electrical signal is then converted to digital domain via high speed ADC. DSP allows compensation of the noise and distortion from the

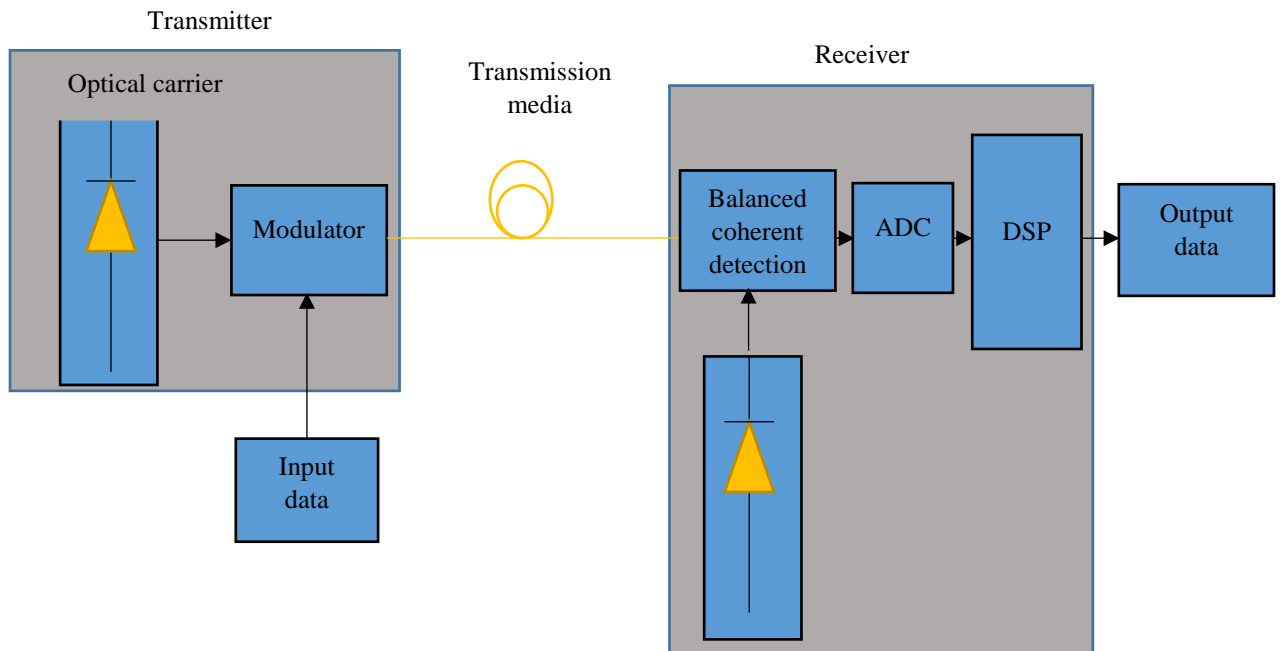


Fig. 2. 1: Structure of coherent optical communication system.

lasers and transmission media while recovering the transmitted information. This chapter provides detailed description of the main components in coherent optical transmission system.

## **2.2. Optical transmitter**

An optical transmitter is a device that encodes the input bits, transforms the bits into symbols of a given a modulation format, and modulates them into the optical carrier for transmission by the media. The general configuration of coherent optical transmitter comprises laser source, and optical modulator as shown in Fig. 2.1.

### **2.2.1. Laser source**

The term “laser” is an acronym for light amplification by stimulated emission of radiation. It implies that turning an atomic system into a laser would require: a lasing medium, also called an amplification medium, a pump to excite the atoms to a higher energy level, and a mechanism that converts the energy of the excited atoms to the output optical signal. This can be practically achieved using an optical resonator.

#### **2.2.1.1. Optical resonator**

The basic optical resonator is a cavity formed by two parallel mirrors facing each other, with the lasing medium placed in between as shown in Fig. 2.2. The mirrors reflect spontaneously emitted photons out of the system while forcing the coherent photons back, so they can stimulate more photons and thus contribute to the lasing process. The external source pumps the lasing medium to generate excited atoms in high energy state. As the excited atoms decay to low energy state, they release energy via spontaneous emission by

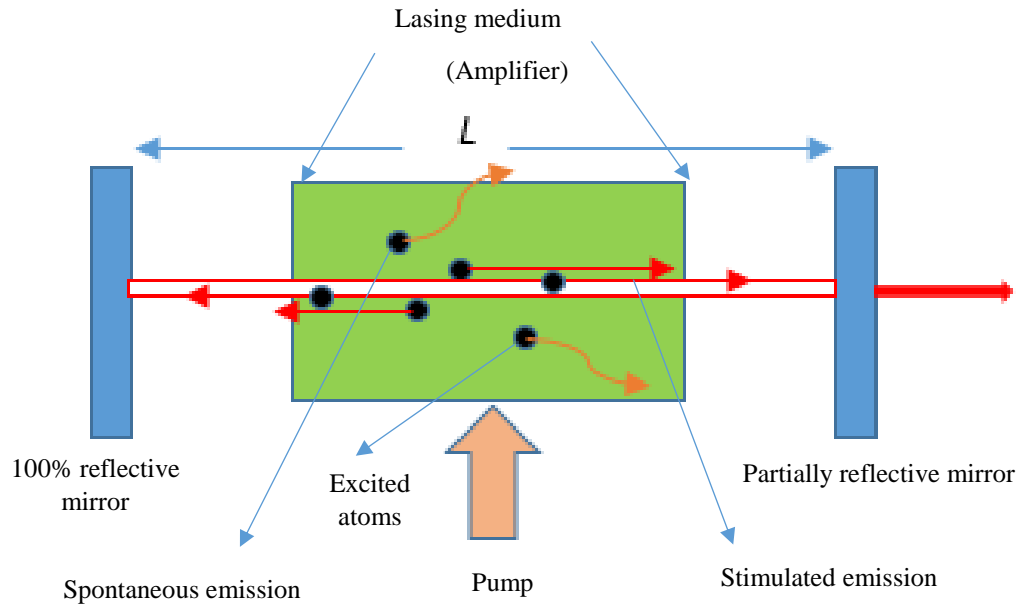


Fig. 2. 2: Optical resonator

emitting non-coherent photons in all directions. Some of the photons travel along the axis of the lasing medium, while others are directed outside. The photons traveling along the axis bounce back and forth between the end mirrors, causing excited atoms in the lasing medium to undergo stimulated emission by emitting coherent photons. Lasing action or optical oscillation, which depends on the pump power and atom density, takes place when light amplification due to the stimulated emission dominates over spontaneous emission [82]. The amount of amplification or gain due to stimulated emission must be higher than the resonator loss to ensure optical oscillation. Also, one mirror is partially reflective to couple optical signal to the output.

For a linear resonator, the oscillation frequency of the output optical signal can be obtained as [83]:

$$f = q \frac{c}{2nL} \quad (2.1)$$

Here  $L$  is the distance between the mirrors,  $q$  is an integer,  $n$  is the refraction index of the medium and  $c$  is the speed of light. To obtain a monochromatic laser source, the gain bandwidth should be kept less than the free spectral range (FSR) ( $\frac{c}{2nL}$ ). Light sources in optical communication are predominantly semiconductor diode lasers where photons are generated via carrier (electrons and holes) recombination. Since the gain bandwidth of laser diode is larger than the FSR of the semiconductor cavity, typically distributed feedback (DFB) laser diodes achieve monochromatic light by employing Bragg grating to ensure that lasing would occur in a single longitudinal mode.

Laser diodes in coherent optical communication must be monochromatic with constant amplitude, phase, and frequency. However, there are many reasons that lead to random fluctuations in the amplitude, phase, and frequency of the laser source including quantum noise associated with the spontaneous emission, vibration of the resonator, and temperature variations [84].

#### **2.2.1.2. Laser amplitude noise**

Amplitude noise refers to the fluctuations of the laser output power over time. This noise occurs for many reasons but the most intuitive one is the stimulated emission. In [84], it has been shown that the laser energy has a direct proportion to the number of stimulated photons. Therefore, addition or removal of one photon would change the output laser power. Additional contributions to amplitude noise could be the unstable pump power and resonator losses.

### 2.2.1.3. Laser phase and frequency noise

Phase noise refers to fluctuations of the output optical signal phase over time. It is mainly attributed to the random phase of the spontaneously-emitted photons. For a single mode semiconductor laser, the phase variance can be found in terms of the number of excited electrons ( $N_2$ ), number of non-excited electrons ( $N_1$ ), average number of quanta in the mode  $\bar{n}$ , symbol duration ( $\tau$ ), and photon lifetime in the laser resonator without pumping the lasing medium ( $\tau_{ph}$ ) as [85]:

$$\sigma^2(\tau) = \frac{N_2/(N_2-N_1)}{2\bar{n}\tau_{ph}} \tau \quad (2.2)$$

The phase noise is related to frequency fluctuation or linewidth, ( $\Delta\nu$ ) as follows:

$$\Delta\nu = \frac{d\sigma^2(\tau)}{2\pi d\tau} = \frac{N_2/(N_2-N_1)}{4\pi\bar{n}\tau_{ph}} \quad (2.3)$$

For coherent communications, the effect of  $\sigma^2(\tau)$  over a symbol duration ( $\tau$ ) can be found in terms of the laser linewidth at the transmitter ( $\Delta\nu_{Tx}$ ) and laser linewidth at the receiver ( $\Delta\nu_{Rx}$ ) as [85]:

$$\sigma^2(\tau) = 2\pi(\Delta\nu_{Tx} + \Delta\nu_{Rx})\tau \quad (2.4)$$

Since the baud rate is the inverse of the symbol duration ( $\tau$ ), it is clear that the effect of phase variation can be minimized by increasing the baud rate.

## 2.2.2. Modulator

Modulator is a device that changes the amplitude, phase or the frequency of the laser source in response to the information being transmitted. Here we focus on amplitude modulation, also called intensity modulation, as well as phase modulation.

### 2.2.2.1. Amplitude modulation

Amplitude modulation is the process of conveying user information into a laser source amplitude. Many optical communication systems apply this type of modulation owing to its simplicity. There are two techniques used for intensity modulation namely: direct modulation and external modulation.

#### 2.2.2.1.1. Direct modulation

In direct modulation, the laser emits light when 1 is being transmitted and emits no light when 0 is being transmitted as illustrated in Fig. 2.3.

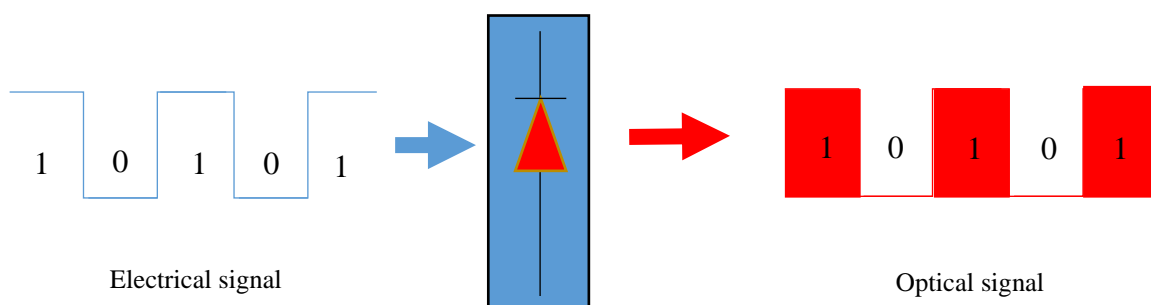


Fig. 2. 3: Intensity modulation

For this type of modulation, the laser switching speed should be fast enough to allow proper operation at the desired bit rate. At a data rate of 100 Gbps for instance, the duration of the optical pulse is 10 ps and therefore the expected laser switching speed should be within a fraction of this pulse duration. This is not practically visible due to the long-life time of the

photon in the resonator and the relaxation oscillation frequency [86]. The intensity noise of the laser signal is also another obstacle for applying direct modulation in high speed optical transmission.

### 2.2.2.1.2. External modulation

In external modulation, the limited switching speed and amplitude noise of the laser source are mitigated by moving the modulation process out of the laser source to an interferometric structure such as Mach Zehnder interferometer (MZI). In this case, MZI would operate as a switch that allows the signal corresponding to '1' to pass and blocks the signal that corresponds to '0'. In contrast to direct modulation, external modulation allows for modulation at higher data rate. In addition, high order modulation formats can be achieved by modulating both the amplitude and phase of optical carrier, which in return increase the transmission capacity.

### 2.2.2.1.3. Mach Zehnder interferometer (MZI)

The basic MZI configuration is shown in Fig. 2.4. As can be seen, it comprises two waveguide arms with lengths  $L_1$  and  $L_2$ , a splitter (S), and a combiner (C). As the light

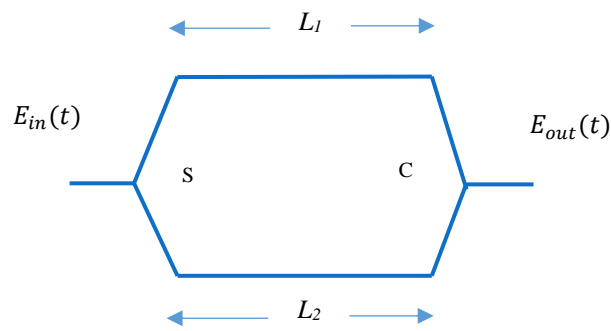


Fig. 2. 4: MZI configuration

signal ( $E_{in}(t)$ ) is fed to the input, S splits the signal equally into the two arms. C then combines the light from the two arms to produce the output signal ( $E_{out}(t)$ ). The optical signal phase ( $\phi$ ) at the output of each arm can be found in terms of the signal wavelength ( $\lambda$ ), arm length, and the refractive index ( $n$ ) of the arm material as:  $\phi_1 = \frac{2\pi}{\lambda} n(L_1)$  and  $\phi_2 = \frac{2\pi}{\lambda} n(L_2)$  respectively, assuming that both arms are made from the same material.

Therefore, the electrical field transfer function for the MZI can be found as:

$$\frac{E_{out}(t)}{E_{in}(t)} = \frac{e^{j\phi_1} + e^{j\phi_2}}{2} \quad (2.5)$$

Thus,  $\frac{E_{out}(t)}{E_{in}(t)}$  varies depending on the differential phase shift between the signals in the two arms.

Amplitude modulation can be achieved by controlling  $\phi_1$  and  $\phi_2$  in (2.5). For example, if  $\phi_1 = \phi_2 = 2\pi$ , then we find that:

$$\frac{E_{out}(t)}{E_{in}(t)} = \frac{e^{j\phi_1} + e^{j\phi_2}}{2} = \frac{e^{j2\pi} + e^{j2\pi}}{2} = \frac{2}{2} = 1 \quad (2.6)$$

Simplifying to

$$E_{out}(t) = E_{in}(t) \quad (2.7)$$

Similarly, if  $\phi_1 = 2\pi$  and  $\phi_2 = \pi$ , then

$$\frac{E_{out}(t)}{E_{in}(t)} = \frac{e^{j2\pi} + e^{j\pi}}{2} = \frac{e^{j2\pi} + e^{j\pi}}{2} = \frac{1-1}{2} = 0 \quad (2.8)$$

Simplifying to

$$E_{out}(t) = 0 \quad (2.9)$$

From (2.7) and (2.9), we conclude that MZI can be used as an amplitude modulator if the phases of the optical signals in the modulator arms are changed as a function of the modulating signal.

In practice, MZI are made from Titanium that is diffused onto a substrate layer made of Lithium Niobate crystal ( $\text{LiNbO}_3$ ).  $\text{LiNbO}_3$  has a strong electro-optic effect such that if a voltage  $u(t)$  is applied to it as shown in Fig. 2.4b, a change in the refractive index ( $\Delta n_{\text{eff}}$ ) would be induced. The change in the refractive index would result in a change of the optical length and thus a phase shift  $\varphi_{\text{PM}}$  is induced which can be obtained as [87]:

$$\varphi_{\text{PM}} = \frac{2\pi}{\lambda} \Delta n_{\text{eff}} L \propto u(t) \quad (2.10)$$

where  $L$  is the the length of the light path along the optical axis as shown in Fig. 2.5. We define the half wave voltage ( $V_\pi$ ) as the applied voltage required to induce a phase shift of 180 degrees. The phase introduced in the waveguide is related to  $u(t)$  and  $V_\pi$  as :

$$\varphi_{\text{PM}} = u(t) \left( \frac{\pi}{V_\pi} \right) \quad (2.11)$$

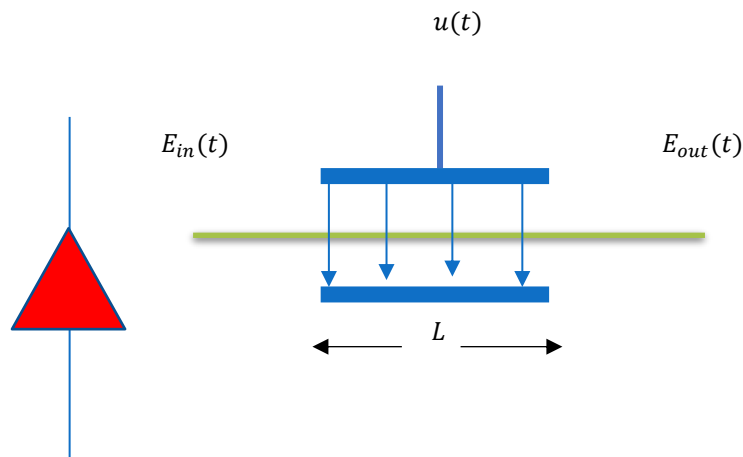


Fig. 2. 5: Principles of phase modulation

Therefore, the electrical field transfer function for the phase modulator in Fig. 2.5 can be found as :

$$\frac{E_{out}(t)}{E_{in}(t)} = e^{j\phi_{PM}} = e^{ju(t)\left(\frac{\pi}{V\pi}\right)} \quad (2.12)$$

The MZI with electro-optic arms is usually referred to as Mach Zehnder modulator (MZM). Thus, amplitude modulation can be achieved using the MZM shown in Fig. 2.6. Here, the upper arm length, hence the phase of the optical signal in the arm, is controlled by  $u(t)$  while the lower arm length is kept constant. Therefore, the transfer function in (2.5) can be modified as:

$$\frac{E_{out}(t)}{E_{in}(t)} = \frac{e^{ju(t)\left(\frac{\pi}{V\pi}\right)} + e^{j\theta_2}}{2} \quad (2.13)$$

Applying a voltage across the MZM arm would shift the phase of the signal in that arm by an amount proportional to  $u(t)$ . If the phase shift equates to an integral number of

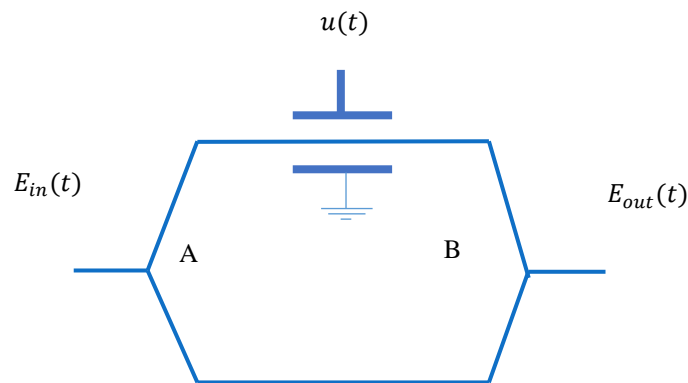


Fig. 2. 6: (a) MZI with phase modulator embedded in one arm.

wavelengths, the two light beams in the arms will combine constructively, and the intensity of the output light will be at its maximum. If the phase shift is a half wavelength out of phase, the two beams will combine destructively, and the output light will be at its minimum. For example, in Fig. 2.6, if  $u(t)$  changes between 0 and  $V_\pi$ , the induced phase shift in the upper arm would change between 0 and  $\pi$ . If  $\phi_2 = 2\pi$ , then from (2.13) we have:

$$E_{out}(t) = \begin{cases} E_{in}(t) & \text{if } u(t) = 0 \\ 0 & \text{if } u(t) = V_\pi \end{cases} \quad (2.14)$$

Notice that when there is no voltage applied to the upper arm, the output will be maximum only if the arms of the MZM are symmetric. This symmetry ensures that the modulated output of the MZM is not shifted in phase/frequency, also called frequency chirped. Ensuring the arms symmetry is practically challenging due to material inhomogeneity, waveguide non-uniform doping profiles, and manufacturing tolerances [88]. Therefore, to overcome the frequency chirp, both arms of the MZI should be made of an electro optic material where the electrodes are driven by complimentary signals ( $u(t)$  and  $-u(t)$ ) as shown in Fig. 2.7. This configuration is the most commonly used for amplitude modulation and is referred to as chirp free or push-pull configuration. The electrical field transfer function for the MZM with push pull configuration can be found as:

$$\frac{E_{out}(t)}{E_{in}(t)} = \frac{e^{ju(t)\left(\frac{\pi}{V_\pi}\right)} + e^{-ju(t)\left(\frac{\pi}{V_\pi}\right)}}{2} = \cos\left[u(t)\left(\frac{\pi}{V_\pi}\right)\right] \quad (2.15)$$

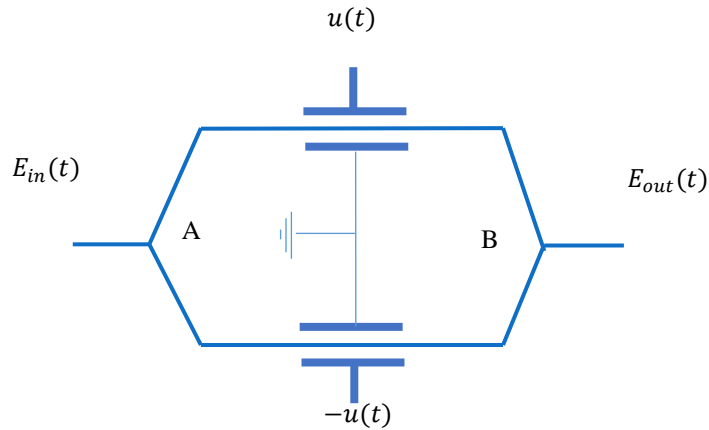


Fig. 2. 7: (a) MZI with phase modulator embedded in one arm.

From (2.15), the amplitude modulation can then be obtained by alternating  $u(t)$  between 0 and  $\frac{V_\pi}{2}$  such that:

$$E_{out}(t) = \begin{cases} E_{in}(t) & \text{if } u(t) = 0 \\ 0 & \text{if } u(t) = \frac{V_\pi}{2} \end{cases} \quad (2.16)$$

Commercial MZM are either single drive or dual drive. In the single drive, separate pair of electrodes are used to drive each arm independently. Dual drive MZM uses only one electrode to drive both arms with complementary voltage levels.

#### 2.2.2.2. Phase modulation

Phase modulation refers to the process in which the optical carrier phase changes in response to user information. As described in section 2.2.2.1.3, if a voltage is applied to electro-optic material like  $\text{LiNbO}_3$ , its refractive index changes and that introduce a phase shift to the optical signal (see Fig. 2.5). Phase modulation can also be obtained using the

dual drive MZM shown in Fig 2.7. In this case, both arms are driven by equal voltage  $u(t)$ .

Therefore, the electrical field transfer function can be obtained as:

$$\frac{E_{out}(t)}{E_{in}(t)} = \frac{e^{j\frac{u(t)}{V_\pi}\pi} + e^{j\frac{u(t)}{V_\pi}\pi}}{2} = e^{j\frac{u(t)}{V_\pi}\pi} = \cos\left(\frac{u(t)}{V_\pi}\pi\right) + j \sin\left(\frac{u(t)}{V_\pi}\pi\right) \quad (2.17)$$

Thus, any phase shift angle can be obtained by controlling  $u(t)$ . For instance,  $\frac{\pi}{4}$  phase shift can be obtained by setting  $u(t) = \frac{V_\pi}{4}$ . Also, binary phase shift keying (BPSK) signal can be obtained by alternating  $u(t)$  between  $V_\pi$  and  $-V_\pi$ .

#### 2.2.2.2.1. In phase/quadrature (I/Q) modulator (QPSK modulator)

The amplitude and phase of an optical carrier can be modulated by binary data simultaneously so that each  $n$  bits of the input data are mapped into one symbol ( $M$ ) such that:

$$n = \log_2(M) \quad (2.18)$$

This helps carry more information as compared to either amplitude or phase modulation alone. QPSK modulation, for instance, uses four symbols to carry the information ( $M = 4$ ) and therefore the number of bits per symbol according to (2.18) is  $n = 2$  bits.

QPSK can be achieved using two parallel MZMs embedded in MZI structure and  $\pi/2$  phase shifter as shown in Fig. 2.8. The input power is split into two components. The BPSK signals constellations point A (Fig. 2.9a) and point B (Fig. 2.9b) are generated by the binary dual drive MZMs in the upper and lower paths. The BPSK in the lower arm is phase-shifted by  $\pi/2$  generating the BPSK signal at point C as shown in Fig. 2.9c. The

BPSK signal in the upper path is combined with the  $\pi/2$  phase-shifted signal, generating the QPSK signal as point D as illustrated in Fig. 2.9d.

The electrical field transfer function for the QPSK modulator can be obtained from (2.15)

as:

$$\frac{E_{out}}{E_{in}} = \cos\left(\frac{u_I(t)}{V_\pi}\pi\right) + j \cos\left(\frac{u_Q(t)}{V_\pi}\pi\right) \quad (2.17)$$

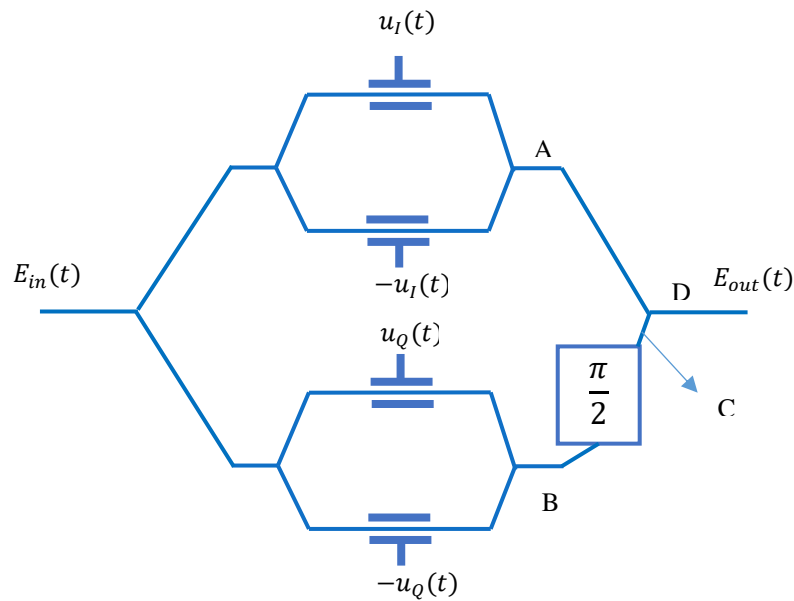


Fig. 2. 8: I/Q modulator

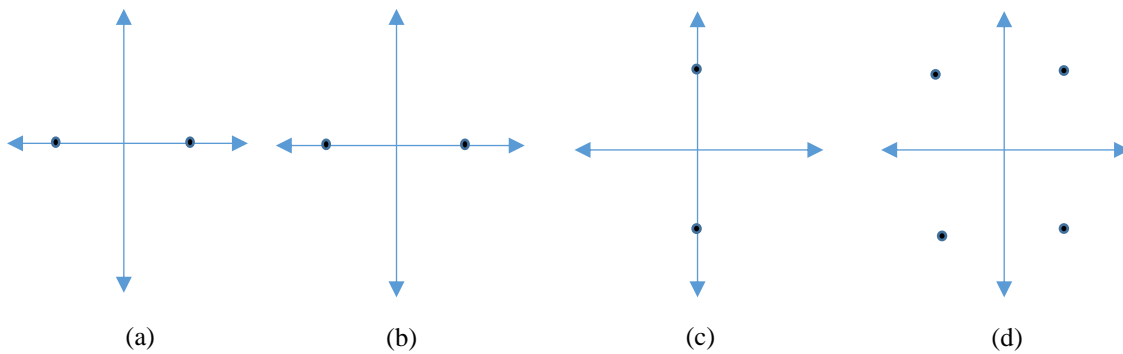


Fig. 2.9: (a) signal constellation at point A; (b) signal constellation at point B; (c) signal constellation at point C; (d) signal constellation at point D.

The QPSK modulator with two MZM in push-pull configuration is the basic building block for all high speed optical transmitters.

### 2.3. Gray coding

The bits at the transmitter input should be mapped into  $M$  symbols so that any two adjacent symbols in the resulting signal constellation would differ in only one bit as illustrated in Fig. 2.10a. This bit mapping is called Gray code. Gray code is important to minimize the BER during symbols recovery. Fig. 2.10 illustrates QPSK Gray coded and Non-Gray coded symbol constellations. For the Non-Gray coded constellation, the complementary symbols 11 and 00 as well as 01 and 10 are next to each other. This would result in high BER since the detection errors usually take place between neighboring constellation points [89]. Therefore, the Gray coding minimizes the BER since the adjacent symbols differ in only one bit as illustrated.

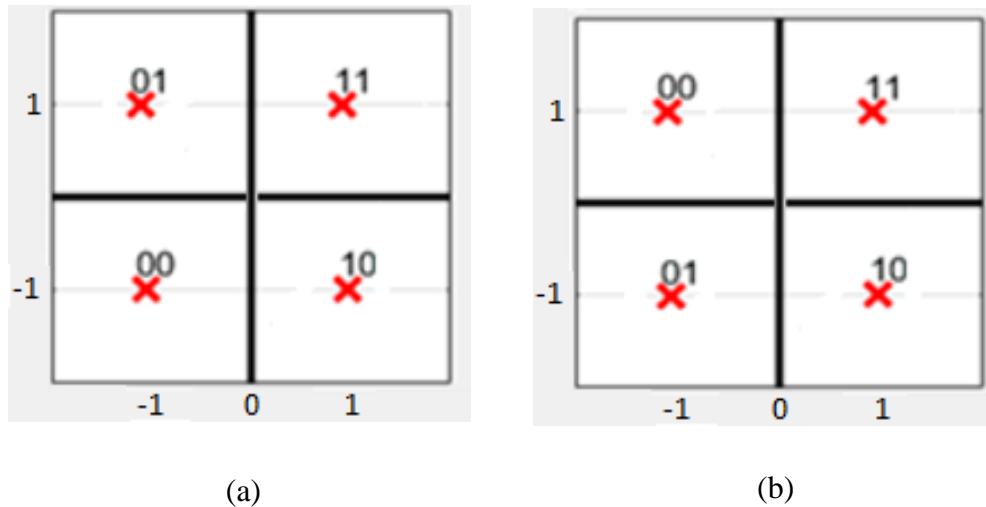


Fig. 2. 10: (a) Gray coded QPSK constellation; (b) Non-Gray coded QPSK constellation.

## 2.4. Commercial MZM

Commercial MZMs use two sets of electrodes as shown in Fig. 2.11. The RF port is used for the input modulating signal and the DC port is used for biasing the MZM at the required

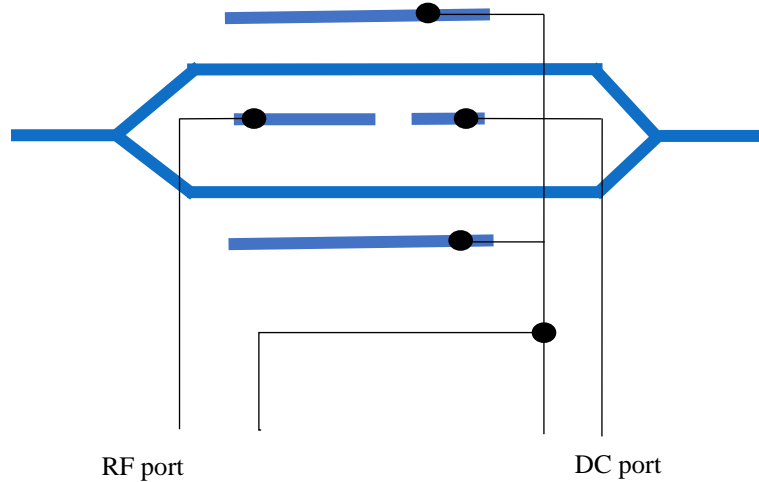


Fig. 2.11: Commercial MZM

operating point. Having a DC biasing port is important to allow various modulation formats through the MZM. It also encounters for errors that occur during the manufacturing processes or during operational lifetime [90]. The MZM transfer function in (2.15) can be rewritten in terms of the DC bias voltage ( $V_b$ ) and the input signal to the RF port  $V_{RF}(t)$  as:

$$\frac{E_{out}(t)}{E_{in}(t)} = \cos\left((V_b + V_{RF}(t)) \frac{\pi}{V_\pi}\right) \quad (2.20)$$

The plot of the commercial MZM transfer function is shown in Fig. 2.12.

To operate the commercial MZM as an intensity modulator for instance,  $V_b$  should be set to  $\pm \frac{V_\pi}{2}$ , also called the quadratic point. At the same time, the peak to peak voltage of the RF input signal should be limited to  $V_\pi$  to ensure linear operation. Similarly, to operate the

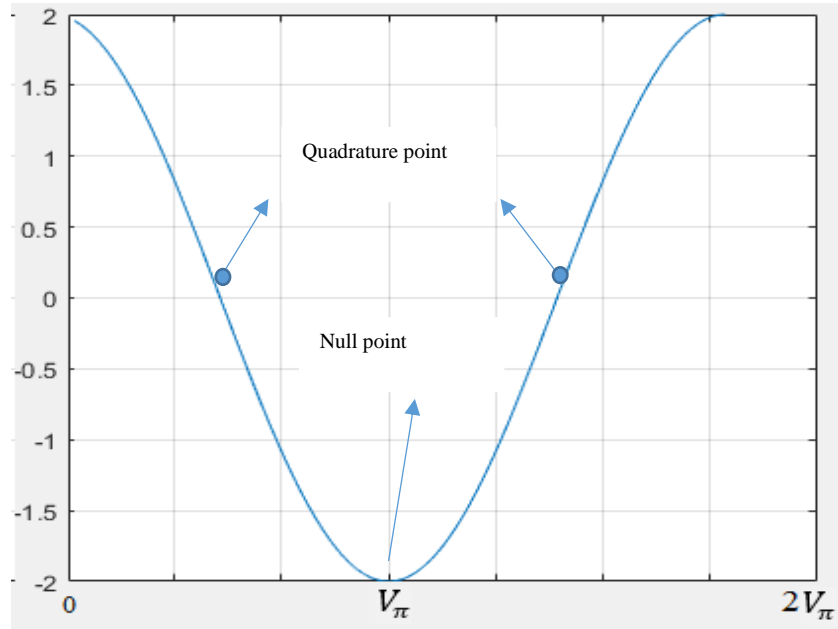


Fig. 2.12: MZM transfer function

MZM as phase modulator, the DC biasing voltage need to be set to  $V_\pi$ , also called the null point, and the RF peak to peak voltage need to be limited to  $2V_\pi$

#### 2.4.1. MZM errors due to arm's length mismatch

For unbiased operation, the optical signals in the interferometric arms of the MZM should have equal phase. In practice however, there is arm's length mismatch due to wave guide material inhomogeneity, non-uniform refractive index profile, and manufacturing tolerances [91]. The arm's length mismatch would inquire phase error ( $\Delta\phi_m$ ), which can be obtained in terms of the waveguide refractive index ( $n$ ), differential length between the two arms ( $\Delta L$ ), and the optical signal wavelength as:

$$\Delta\phi_m = \frac{2\pi n \Delta L}{\lambda} \quad (2.21)$$

The MZM transfer function in (2.15) can be represented in terms of  $\Delta\phi_m$  as:

$$\frac{E_{out}(t)}{E_{in}(t)} = \cos \left( (V_b + V_{RF}(t)) \frac{\pi}{V_{\pi}} + \Delta\phi_m \right) \quad (2.22)$$

It is clear from (2.22) that the error due to  $\Delta\phi_m$  can be compensated by tuning  $V_b$ .

### 2.4.2. MZM errors due to drift in the operating point

One of the major problems associated with practical application of MZM is the drifting of the DC operating point over time. The drifting is caused by pyro-electric, photorefractive and photoconductive phenomena in LiNbO<sub>3</sub> substrate [92]. Drifting in the operating point leads to a displacement of the transfer function, resulting in a performance deterioration. Since the drift in the operating point varies time, feedback is essential to stabilize the operating point via a bias control circuit. In the following subsections, we will briefly describe two simple and widely used bias control techniques.

#### 2.4.2.1. Bias control based on the output optical power of MZM

In this technique, a photodetector (PD) is used to monitor the output power of the MZM as shown in Fig. 2.13. The output current from the PD is amplified using transimpedance

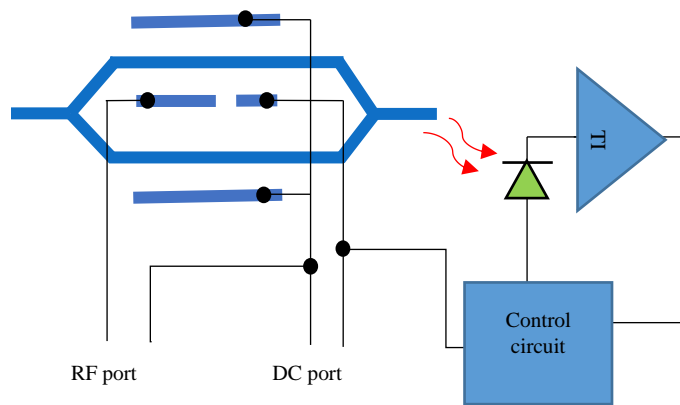


Fig. 2.13: Bias control based on change in output optical power.

amplifier (TIA) and then used as a feedback to drive a bias control circuit that is connected to the MZM DC bias voltage. The control circuit can be designed using a comparator that compares the average voltage from the TIA to the expected average voltage from the TIA under the drifting free scenario. Even though this technique is simple, the accuracy is questionable because the average output power from the MZM varies not only with the drift in the DC voltage, but also with the input optical power to the MZM [93].

#### 2.4.2.2. Bias control based on harmonic analysis

This method focuses on detecting the drift in the operating point by analyzing the spectrum of the optical signal at the output of the MZM. It has been shown in [93] that under no biasing errors, the second harmonic of the output signal has minimum amplitude at the quadrature operating point ( $V_b = \pm \frac{V_\pi}{2}$ ) as shown in Fig. 2.14. Meanwhile, the first harmonic has constant magnitude over the entire range of the biasing voltages as shown in

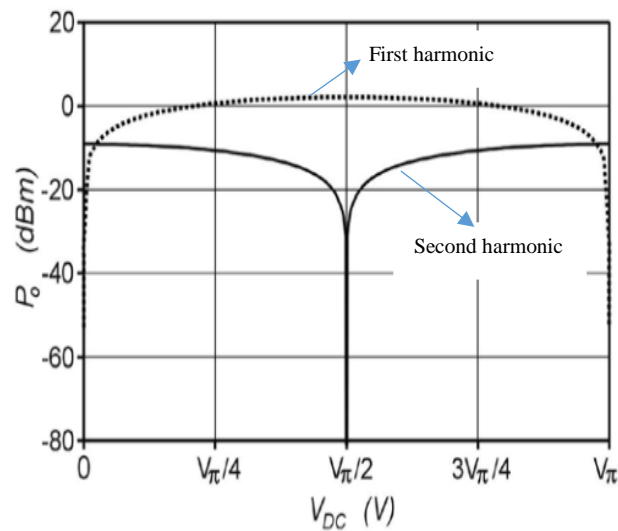


Fig. 2.14: Comparison between the power of first harmonic (dotted curve) and the second harmonic of the output optical power [93].

Fig. 2.14. Therefore, the magnitude of the second harmonic can be used as an indicator of the drifting in the DC bias.

## 2.5. Optical fiber

Optical fiber is the medium that connects the transmitter to the receiver. It is made of glass and has two concentric sections: core and cladding as shown in Fig. 2.15. The core is the part of the fiber in which light propagates while the cladding prevents the light from escaping. Light propagation in the fiber is based on the principles of total internal reflection which requires the core material to have higher refractive index than the cladding material.

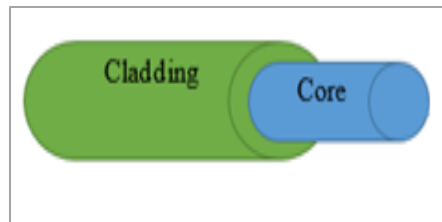


Fig. 2. 15: Optical fiber structure.

There are two types of optical fiber: multimode and single mode fibers. Multimode is characterized by its large core diameter ( $50\ \mu\text{m}$  or  $62.5\ \mu\text{m}$ ) which allows multiple light rays or modes to propagate. This type of fiber is used for local area networks (LANs) that operates at data rates less than 10 Gbps. Single mode fibers on the other hand have a core diameter that is small (less than  $10\ \mu\text{m}$ ) compared to multimode fibers which allows only one mode to propagate. This type of fibers is used for wide area networks that operate at higher data rates. The following subsections review the main transmission impairments of single mode fiber.

### 2.5.1. Attenuation

Attenuation is the degradation in the optical power as the light propagates through the fiber. It occurs mainly because of material absorption and Rayleigh scattering. In material absorption, the optical power converts to heat because of the molecular bonds vibration of the glass material. Atomic defects and impurities such as OH ions can cause optical signal absorption as well. Scattering on the other hand is caused by fluctuations in the density, orientation, and composition of the material. Rayleigh scattering increases in proportional to the inverse fourth power of the optical signal wavelength. Thus, doubling the wavelength would reduce the scattering losses by 16 times. Together, the absorption and scattering produce the attenuation curve for a typical glass optical fiber shown in Fig. 2.16. As can be seen, the attenuation is minimum at wavelength of 1550 nm and therefore it is the most widely used wavelength for long distance optical communications.

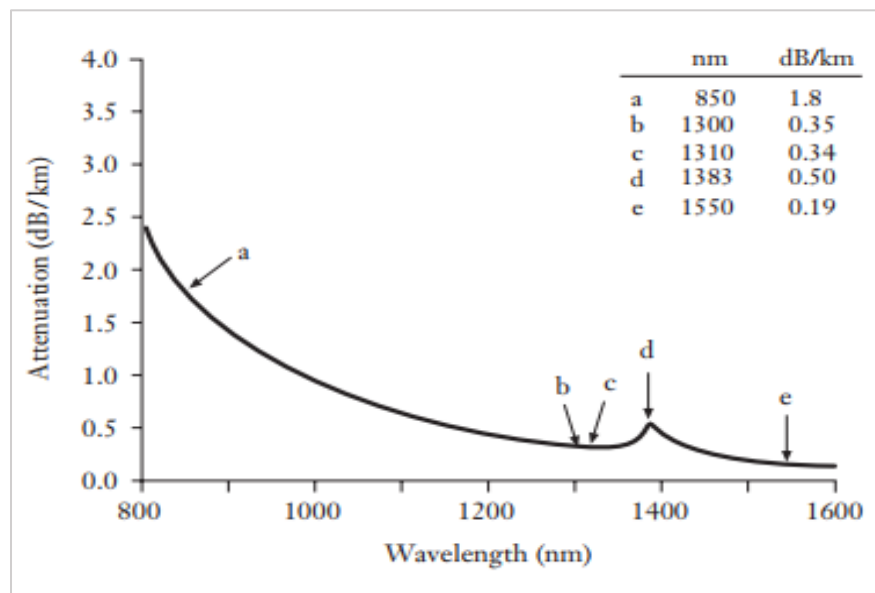


Fig. 2. 16: Attenuation profile for standard single mode fiber [94].

### 2.5.2. Chromatic dispersion (CD)

Chromatic dispersion is the broadening of the optical pulses as they propagate down the fiber. CD occurs because the optical pulse travel down the fiber at different speeds for different wavelengths. The differential speed is caused by the change of fiber's refractive index with wavelength. As a result, longer wavelength components of the signal travels faster than shorter wavelength and cause spreading to the optical pulse as shown in Fig. 2.17. Differential group delay due to CD in single mode fiber that may result in overlapping of high speed pulses, causing inter-symbol interference (ISI) hence error during data recovery.



Fig. 2. 17: Pulse spreading due to chromatic dispersion (CD) [95].

The dispersion introduced in single mode fiber ( $D$ ) can be calculated as function of fiber length ( $L$ ), optical signal wavelength ( $\lambda$ ), fiber refractive index ( $n$ ), the variation of the refractive index with the square of the wavelength as:

$$D = -\frac{L}{3 \times 10^8} \times \lambda \times \frac{\partial^2(n)}{\partial(\lambda^2)} \quad (2.23)$$

The dispersion for typical standard optical fibers is known and can be used to compute the maximum reachable distance at a certain data rate. Fig. 2.18 shows the maximum reachable

distance as a function of bit rates for the most common standard single mode fibers without dispersion compensation. As can be seen, the maximum allowable distance for the G.655 operating at 100 Gbps is about 1 km.

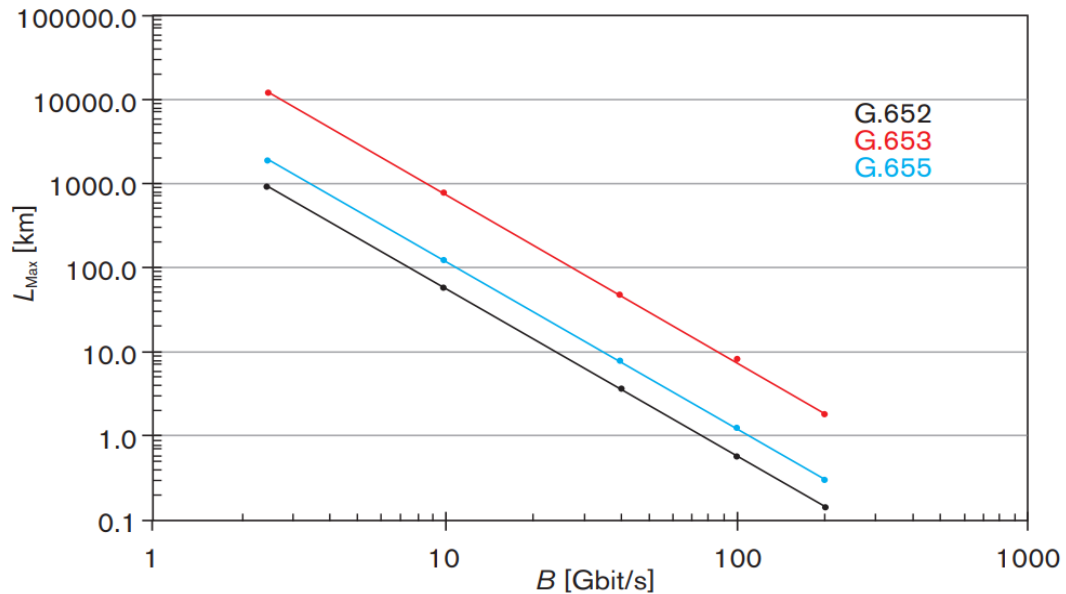


Fig. 2. 18: Maximum allowable distance versus bit rate [96].

Long distance transmission at high bit rates is not feasible without dispersion compensation. In practice, there are several passive and active ways to compensate for CD using DSP techniques and forward error correction (FEC).

### 2.5.3. Polarization mode dispersion (PMD)

Polarization-mode dispersion refers to the pulse spreading caused by light propagating through the fiber at different speeds for different polarization, as illustrated in Fig. 2.19. This is related to fiber birefringence, where the refractive index of the fiber is polarization dependent due to variations in core shape and stress [97]. Like CD, PMD causes spreading

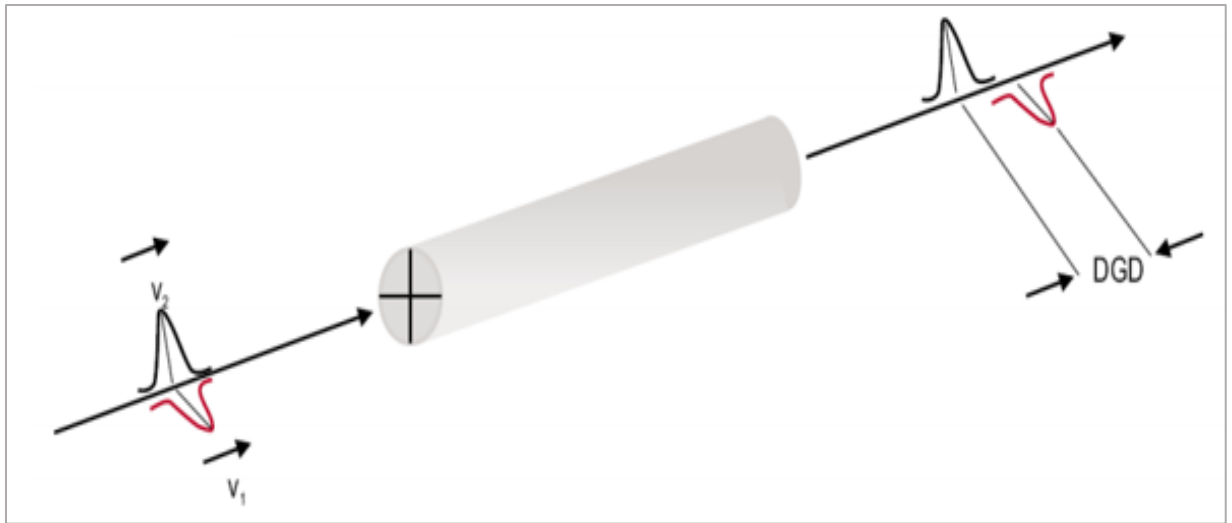


Fig. 2. 19: Polarization mode dispersion (PMD) [98].

to the optical pulse as it propagates down the fiber. The subsequent variation of this index as a function of wavelength leads to the group delay as a function of wavelength. The differential group delay (DGD) varies randomly as a function of frequency. As the pulse broadening due to PMD widens, the pulse stream starts to overlap, causing ISI that degrades the BER performance.

In practice, a pulse spreading of 10% of the bit duration is considered acceptable [98]. Therefore, for 100 Gbps link, the pulse spreading should not exceed 1ps to insure good BER performance.

## 2.6. Coherent optical receiver

The main function of coherent optical receiver is to convert the signal from optical domain to electrical domain, perform ADC, and apply the necessary DSP techniques to recover the transmitted information. The main components of coherent optical receiver are heterodyne detector, ADC, and DSP blocks.

### 2.6.1. Heterodyne detector

The schematic diagram of a heterodyne detector is shown in Fig. 2.20. As can be seen, the detector comprises two 3 dB optical couplers, continuous wave local oscillator (LO) laser,  $\pi/2$  phase shifter, and four photo detectors. The 3-dB optical couplers add a 180 degrees phase shift to either the received optical signal field or the LO field. Therefore, the electric

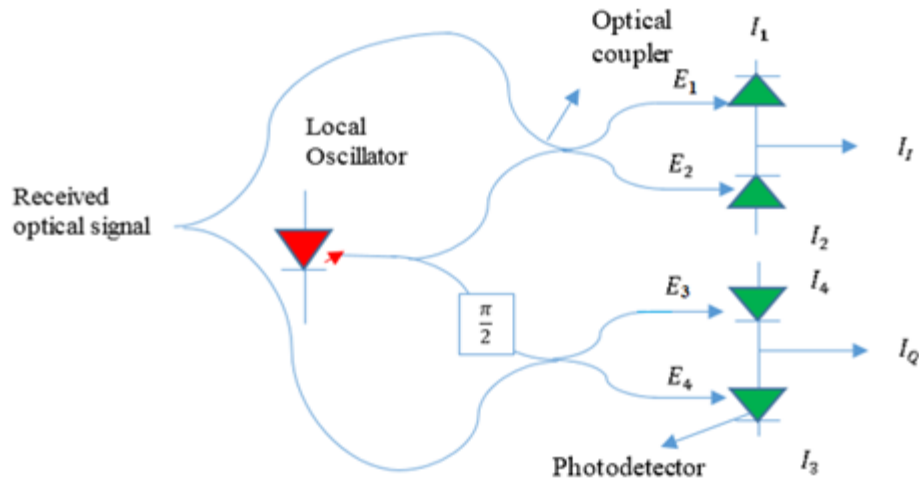


Fig. 2. 20: Heterodyne detector

fields incident on the photodiodes are given as:

$$E_1 = \frac{1}{\sqrt{2}}(E_{Lo} + E_s) , E_2 = \frac{1}{\sqrt{2}}(E_{Lo} - E_s), E_3 = \frac{1}{\sqrt{2}}(E_s + jE_{Lo}), E_4 = \frac{1}{\sqrt{2}}(E_s - jE_{Lo})$$

The photo diode current from the detector can be found as function of photo diodes responsivity ( $R$ ), input signal power ( $P_s$ ), local oscillator power ( $P_{lo}$ ), phase modulation angel ( $\theta_{sig}(t)$ ), local oscillator phases ( $\theta_{lo}(t)$ ), and the difference between input signal frequency and the local oscillator frequency ( $\omega_i(t) = 2\pi(f_s - f_{lo})$ ) as:

$$I_I(t) = I_{I1}(t) - I_{I2}(t) = R\sqrt{P_s P_{lo}} \cos(\omega_i(t) + (\theta_{sig}(t) - \theta_{lo}(t))) \quad (2.24)$$

$$I_Q(t) = I_{Q1}(t) - I_{Q2}(t) = R\sqrt{P_s P_{lo}} \sin(\omega_i(t) + (\theta_{sig}(t) - \theta_{lo}(t))) \quad (2.25)$$

Therefore, the complex photo diode current ( $I_T(t)$ ) is obtained as:

$$I_T(t) = I_I(t) + jI_Q(t) = R\sqrt{P_s P_{lo}} e^{j(\omega_i(t) + \theta_{sig}(t) - \theta_{lo}(t))} \quad (2.26)$$

### 2.6.2. Analog to digital converter (ADCs)

The complex photo diode currents at the output of the balanced detectors in Fig. 2.20 are sampled at high rate and converted to discrete signals using ADCs. ADCs take in the analog current signal, sample it at high rate, resolve it into discrete levels ( $N$ ), and assign  $k$  bits to each level such that  $k = \log_2 N$ . ADCs should sample the received signal at the Nyquist rate which is higher than or equal to twice the symbol rate in order to avoid the Aliasing Effect [99]. Also,  $N$  should be high in order to avoid the quantization errors. For optimal performance, it is preferable to sample the input signal at rate above the Nyquist rate and increase the number of levels to a high number. However, this will lead to more complex hardware and high power consumption [22]. The state-of-the-art ADCs are capable of operating at rate of 65 Gbaud with a resolution of up to 8 bits [24].

### 2.6.3. Digital signal processing (DSP)

The digital signal at the output of ADC is further processed using DSP circuits for noise removal and data recovery. DSP refers to various techniques for improving the reliability and accuracy of coherent optical communication links through the removal of channel impairments, such CD, and PMD as well as laser phase and frequency noise [100]. The use

of DSP in conjunction with coherent detection allows the preservation of full information of the incoming signal, which in return increases receiver sensitivity [101]. Fig. 2.21 shows the DSP block diagram. As can be seen, the signal at the output of the ADC is fed to the CD compensation block which focuses on eliminating the CD in digital domain using multiple techniques such as time domain least mean square adaptive filter, static time domain finite impulse response filter, and frequency domain equalizers [102]. The PMD is also removed in digital domain using adaptive filters such as the least mean square and the constant modulus algorithm filters. Carrier phase estimation algorithms track and remove the phase noise using different methods such as normalized least means square estimator, differential phase estimation, and the Viterbi-Viterbi (VV) estimators [100]. The decision circuit with the appropriate threshold levels is used to recover the bits. The bits are decoded and converted to a serial bit stream at the output.

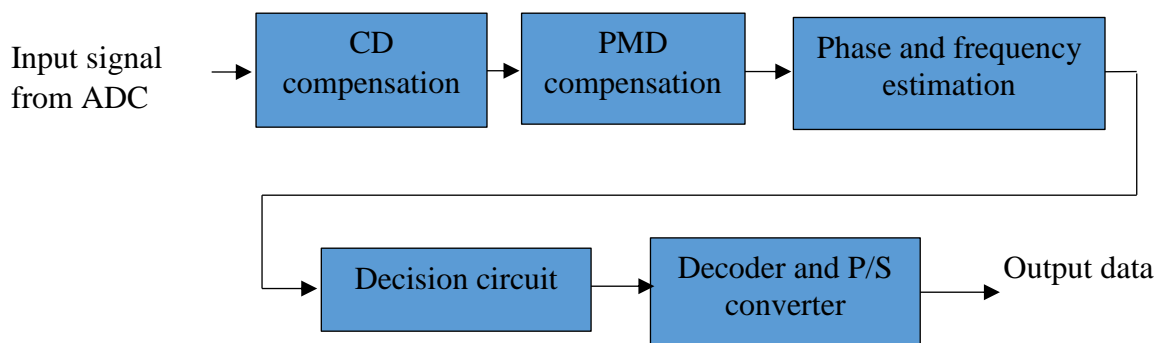


Fig. 2. 21: DSP block diagram.

## 2.7. Conclusion

Coherent optical communication systems are comprised of three main components: transmitter, transmission media, and receiver. The transmitter uses MZM to generate

higher order modulation format signals such as QPSK and 16-QAM. The signals are transmitted to the receiver through a single mode fiber where they encounter attenuation and dispersion. At the receiver, the signals are converted to electrical signals by means of heterodyne detection. The received signal errors are compensated for using DSP techniques.

## **CHAPTER 3: PROPOSED SCALABLE AND GRAY CODED OPTICAL M-ARY QAM TRANSMITTER DRIVEN BY BINARY ELECTRICAL SIGNALS**

### **3.1. Introduction**

Commercially available coherent fiber-optic systems provide a 100 Gbit/s transmission rate using PDM-QPSK at 25 Gbaud symbol rate. Higher-order modulation format such as 16-QAM and 64-QAM will be necessary to accommodate the growing demand on the transmission rates. Several configurations for the 64-QAM transmitter have been investigated both in electrical and optical domains. In the electrical domain, transmitters that employ single optical I/Q modulator driven by multi-level electrical signals from high speed DACs and driving amplifiers have been presented [75]. Those configurations require high-resolution DACs to cope with the non-linearity associated with the Mach–Zender modulator, as well as the driving power amplifiers in order to generate high quality symbol constellations and eye diagrams. While the optical hardware is simple, requiring only one I/Q modulator, the achievable transmission rate and signal quality are limited in practice by the speed and resolution of the DACs [78]. The optical domain configurations, on the other hand, overcome the non-linearity and DACs limitations by employing multiple QPSK modulators that are driven by binary electrical signals [78–81]. However, those configurations are not easily scalable to higher-order modulation format and some would generate non-Gray coded symbol constellation [103], resulting in high error rate at the receiver. We propose a transmitter that eliminates the need for DACs and provides a

scalable design that could enlarge the data rate based on customer needs. It also provides a Gray coded constellation, thereby insuring delivery of digital data over coherent optical communication systems with the smallest error rate possible.

This chapter describes principles of operation for our proposed design for 16-QAM and 64-QAM transmitters. It also sheds light on the scalability of the transmitter design and investigates the electrical and optical techniques to provide Gray coded symbol constellation.

### 3.2. Operating principles for 16-QAM transmitter

Fig. 3.1 shows the block diagram of the 16-QAM transmitter that employs two tandem QPSK modulators. The input data stream is split into four binary data streams D1–D4. QPSK1 is driven by D1 and D2 while QPSK2 is driven by D3 and D4. Each QPSK comprises of a two-dual drive MZM modulator in push pull configuration as shown in Fig. 3.2. The optical carrier at the upper arm of SP1 is split into two components; one is

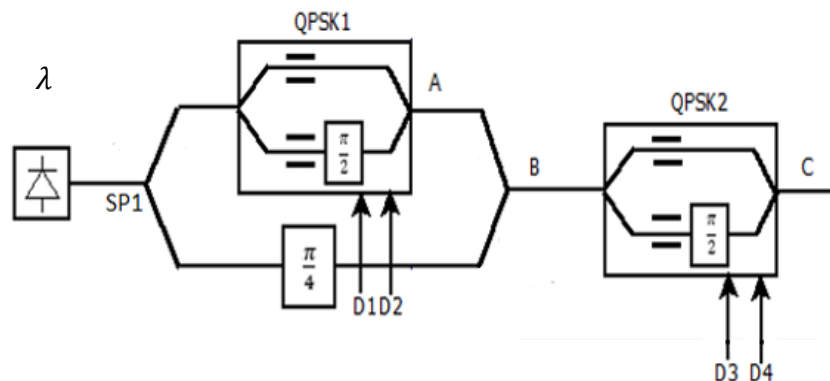


Fig. 3. 1: Optical circuit diagram for 16-QAM.

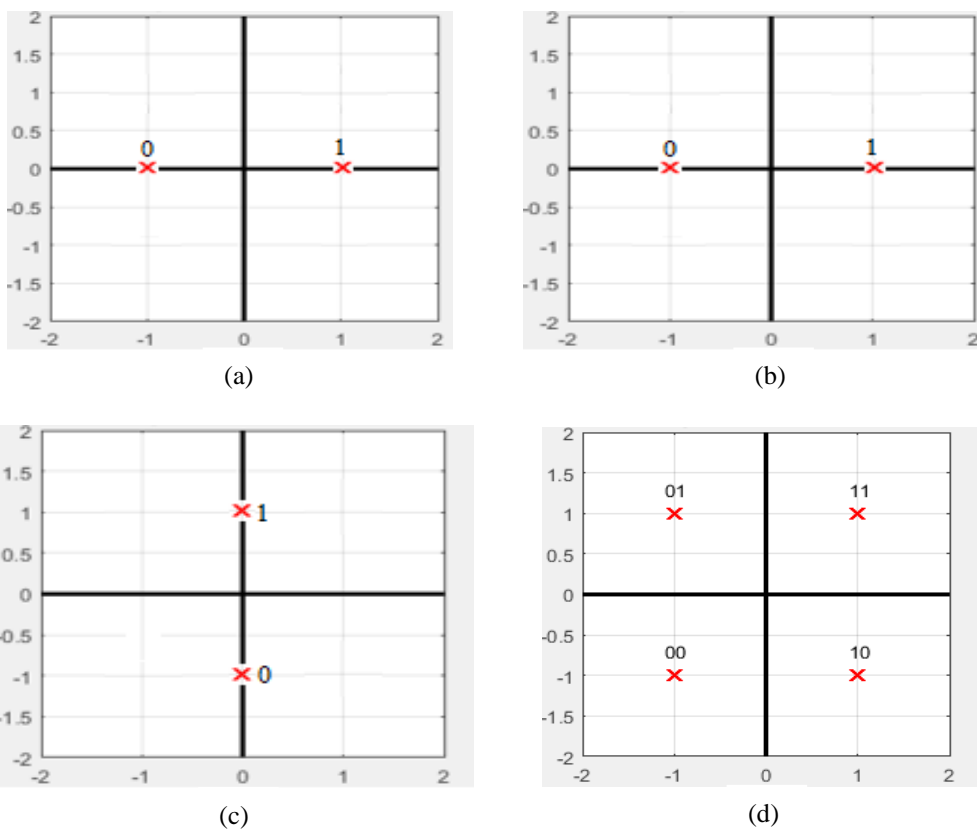
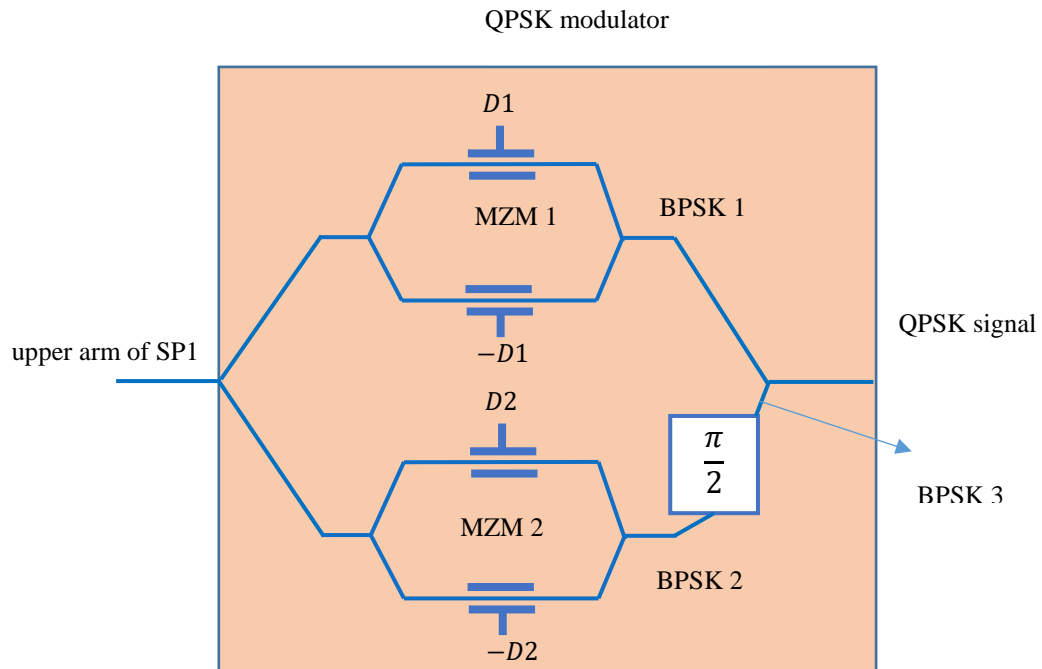


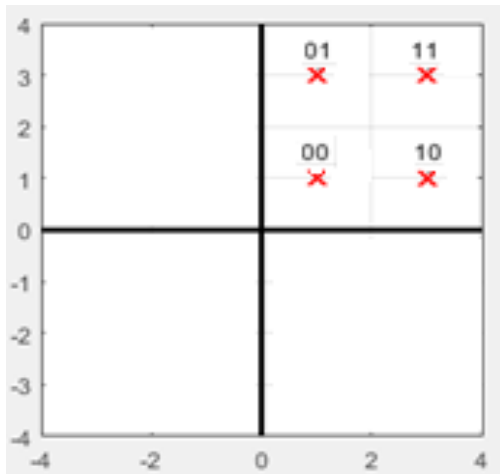
Fig. 3.3: (a) BPSK 1; (b) BPSK 2; (c) BPSK 3; (d) QPSK signal modulated by MZM1 resulting in the BPSK1 signal constellation as shown in Fig. 3.3a,

and the other is modulated by MZM2 resulting in the BPSK2 signal as shown in Fig. 3.3 b. BPSK2 is phase-shifted by  $\pi/2$  generating BPSK3 signal as shown in Fig. 3.3c. BPSK2 and BPSK3 are combined interferometrically to generate the Gray coded QPSK signal as illustrated in Fig. 3.3d.

On the other hand, the optical signal in the lower arm of SP1 (Fig. 3.1) is shifted by  $\pi/4$  and combined interferometrically with the QPSK signal at point A (Fig. 3.1), generating the offset 4-QAM in the first quadrant (point B) as illustrated in Fig. 3.4a. The second QPSK modulator maps the offset constellation to the other quadrants, based on D3 and D4 as illustrated in Table 3.1, generating square 16-QAM constellation (point C) as depicted in Fig. 3.4b.

Table 3. 1: Mapping process

D4D3	Mapping of shifted 4-QAM
00	Third quadrant
01	Second quadrant
10	Fourth quadrant
11	First quadrant



(a)



(b)

Fig. 3.4: (a) 4-QAM shifted to the first quadrant; (b) Non-Gray coded 16-QAM

### 3.3. Generation of a Gray coded 16-QAM constellation

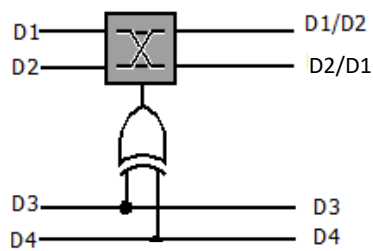
As described in Chapter 2, in order to insure the lowest bit error rate possible at the receiver, it is important that the bit to symbol mapping at the transmitter is arranged such that all the adjacent symbols differ in only one bit, which is known as Gray coding.

In the proposed transmitter, the two QPSK modulators are Gray coded and will produce constellation similar to Fig.3.3d where any two adjacent symbols differ in only one bit. When the Gray coded QPSK constellation at the output of QPSK1 is shifted to the first quadrant (Fig.3.4a) and mapped to the other quadrants, using QPSK2, we notice that the resulting 16-QAM constellation (Fig.3.4b) is not Gray coded. Symbols 0110 and 0101 as well as 1001 and 1010 should be swapped per the arrows in Fig.3.4b in order to restore the Gray coded constellation.

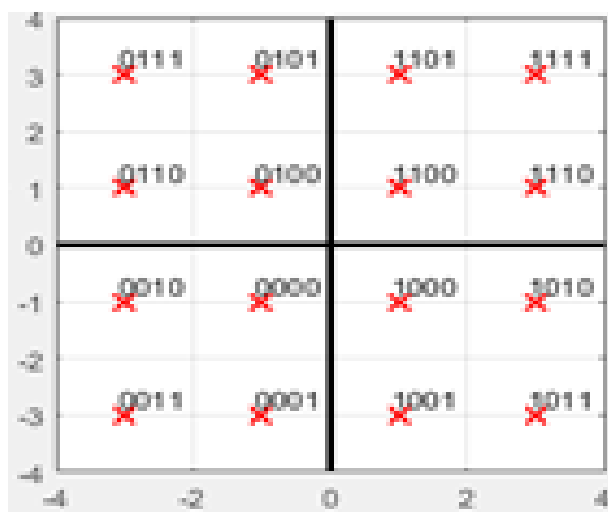
Gray coded constellation can be accomplished in electrical domain with a precoder that would check the two most significant bits, D3 and D4. If  $D3 \neq D4$ , i.e., if the second QPSK modulator operates in the 2nd and 4th quadrants, then D1 and D2 are swapped so that the output of the precoder is D4 D3 D1 D2. If  $D3=D4$ , i.e., if the QPSK2 operates in the 1st and 3rd quadrants, the output of the precoder is D4 D3 D2 D1. Therefore, the input and output of the precoder would be related as shown in Table 3.2. Accordingly, the precoder can simply be implemented using one XOR gate and a switch as shown in Fig. 3.5a. The resulting symbol constellation from the precoder would be identical to Fig. 3.5b after applying the precoder. It should be clear that neither the Gray precoder design nor the selection of symbol rearrangements are unique. For example, the off-diagonal symbols in the 1<sup>st</sup> and 3<sup>rd</sup> quadrants in Fig. 3.4b could be swapped instead.

Table 3. 2: logical table for 16-QAM precoder

Precoder input	Precoder output
0000	0000
0001	0001
0010	0010
0011	0011
0100	0100
0101	0110
0110	0101
0111	0111
1000	1000
1001	1010
1010	1001
1011	1011
1101	1101
1110	1110
1111	1111



(a)



(b)

Fig. 3.5: (a) 16-QAM precoder; (b) Gray coded 16-QAM.

### 3.4. Alternative configuration for a Gray coded 16-QAM transmitter

In the 16-QAM transmitter presented in section 3.2, the Gray coded constellation was achieved by precoding the binary data in the electrical domain using one XOR gate and one switch. In the alternative 16-QAM configuration, we eliminate the electrical domain precoding, and instead employ optical binary phase modulators in order to produce the Gray coded constellation. Fig.3.6 shows the block diagram of the proposed 16-QAM transmitter that employs two QPSK modulators and one phase modulator (PM) in tandem. The input data are split into four parallel data streams, D1, D2, D3, and D4. D1, D2 drive QPSK1 while D3, D4 drive QPSK2. Fig. 3.7a shows the Gray coded constellation produced by QPSK1 at point A. The QPSK constellation at point A is shifted to the first quadrant at point B by combining it with the  $\pi/4$  phase-shifted optical carrier. The offset constellation

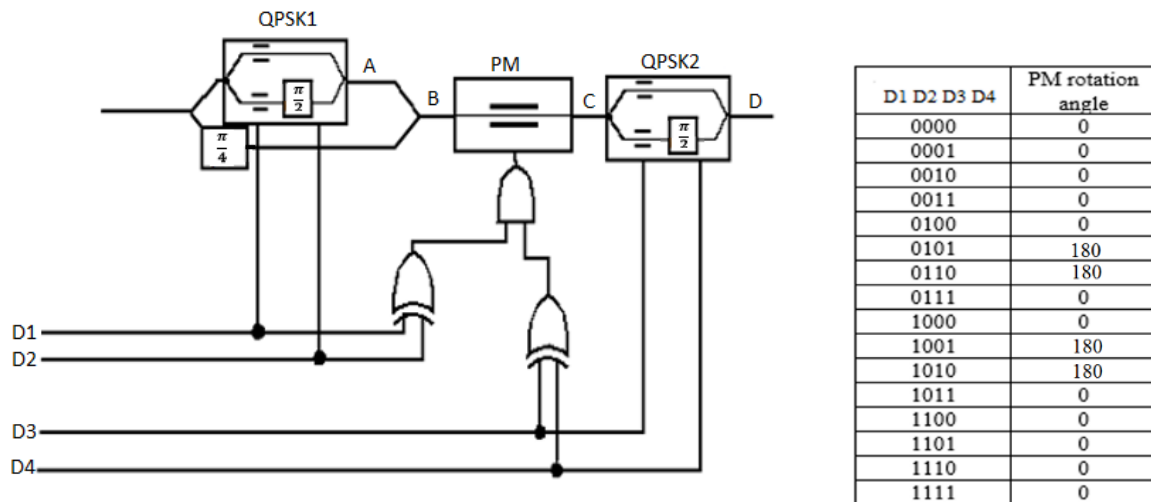
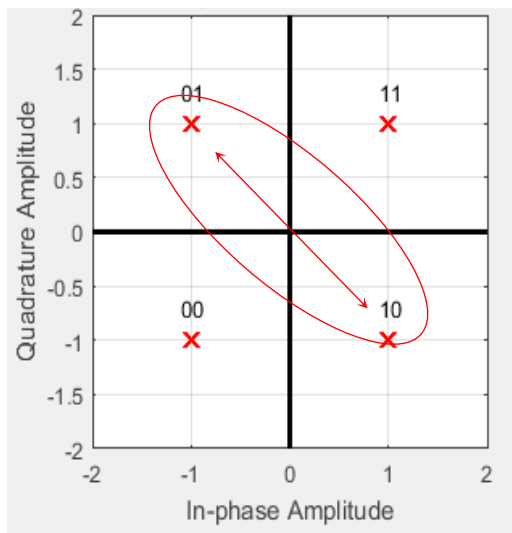


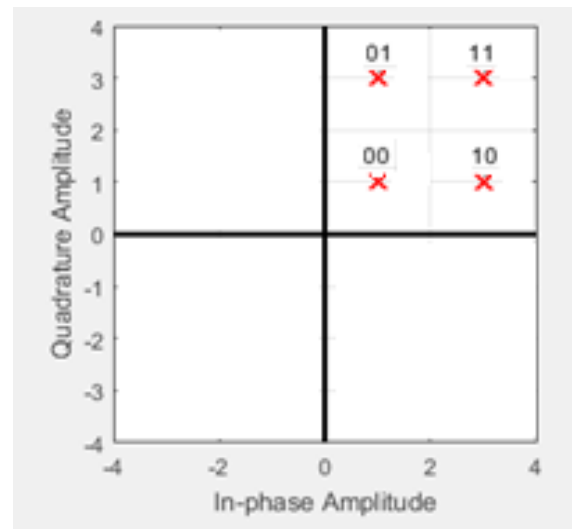
Fig. 3. 6: Alternative configuration for 16-QAM transmitter.

at point B depends on D1 through D4 as shown by the Table in Fig.3.6. If D1, D2 are the same (00 or 11) or D3, D4 are the same, the PM would have zero phase shift and the resulting constellation is as shown Fig. 3.7b. If D1, D2 are not the same (01 or 10) and D3-

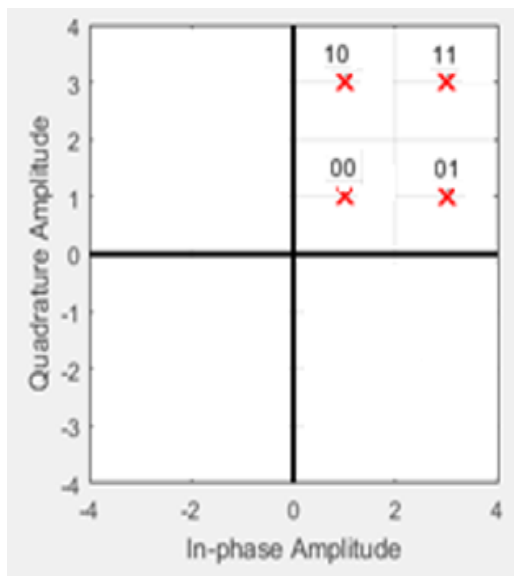
D4 are also not the same, the PM rotates the off-diagonal symbols as shown in Fig. 3.7a by  $180^\circ$ , resulting in the offset constellation shown in Fig. 3.7c. QPSK2 then rotates the



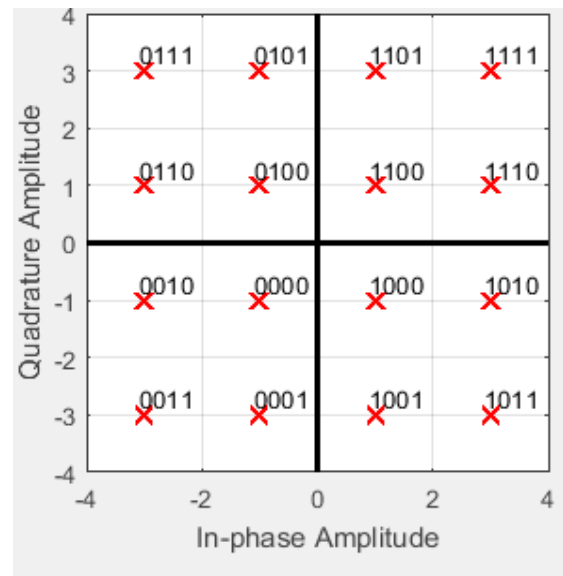
(a)



(b)



(c)



(d)

Fig. 3. 7: (a) Output of QPSK1; (b) Offset constellation for D3, D4 the same; (c) Offset constellation for D3, D4 different; (d) Gray coded 16-QAM output of QPSK2.

offset constellation in Fig. 3.7b or Fig. 3.7c to the four quadrants based on D3, D4, resulting in a Gray coded 16-QAM constellation as shown in Fig. 3.7d.

It can be seen that the 16-QAM symbols have been Gray coded since any adjacent symbols differ in only one bit.

### 3.5. Operating principles for 64-QAM transmitter

The configuration for 16-QAM transmitter in Fig. 3.1 can be scaled up to 64-QAM by adding a third QPSK modulator in tandem, driven by the binary data D5 and D6 as shown in Fig. 3.8. Notice that D1-D4 are the outputs from the 16-QAM precoder as described in Section 3.3.

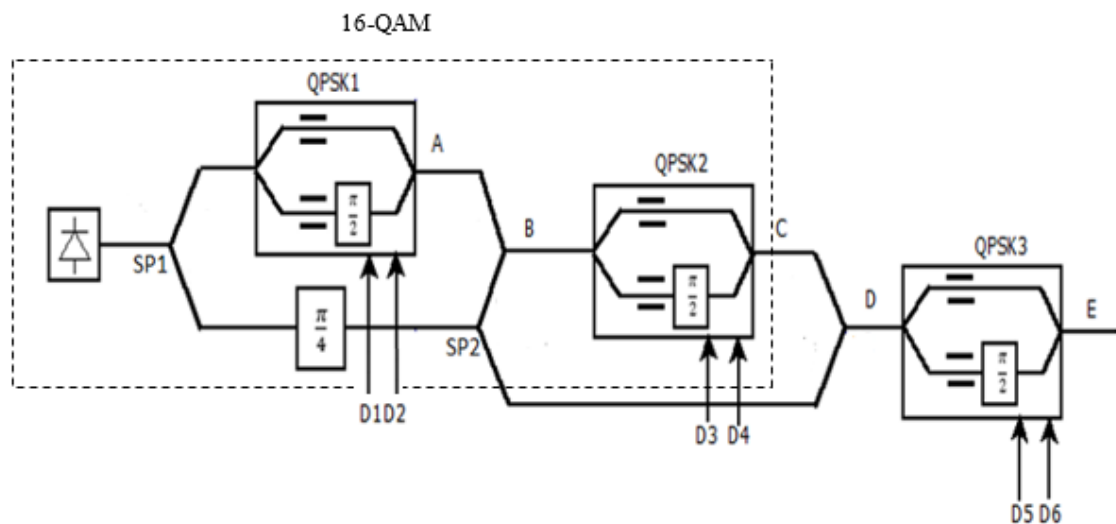


Fig. 3. 8: Optical circuit diagram for 64-QAM.

The 16-QAM constellation (point C) would be shifted to the first quadrant (point D) using the  $\pi/4$  phase shifted carrier and then be mapped to the other quadrants by means of QPSK3 and D5, D6 to generate the 64-QAM signal (point E). The shifted 16-QAM will be mapped to the four quadrants based on the binary value of D5, D6 as illustrated in Table 3.2.

Table 3. 3: Mapping process

D6D5	Mapping of shifted 16-QAM
00	Third quadrant
01	Second quadrant
10	Fourth quadrant
11	First quadrant

The resulting 64-QAM constellation is shown in Fig. 3.9.

As can be seen, the symbols at the border between the four quadrants (inside the dashed box in Fig. 3.9) deviate from the proper Gray coded constellation. Similar to the 16-QAM, the Gray coded constellation can be restored using a precoder that would check the two most significant bits D5 and D6. If  $D5 \neq D6$ , i.e., if QPSK3 modulator operates in the 2<sup>nd</sup> and 4<sup>th</sup> quadrants, then D1 and D2 as well as D3 and D4 are swapped so that the output of

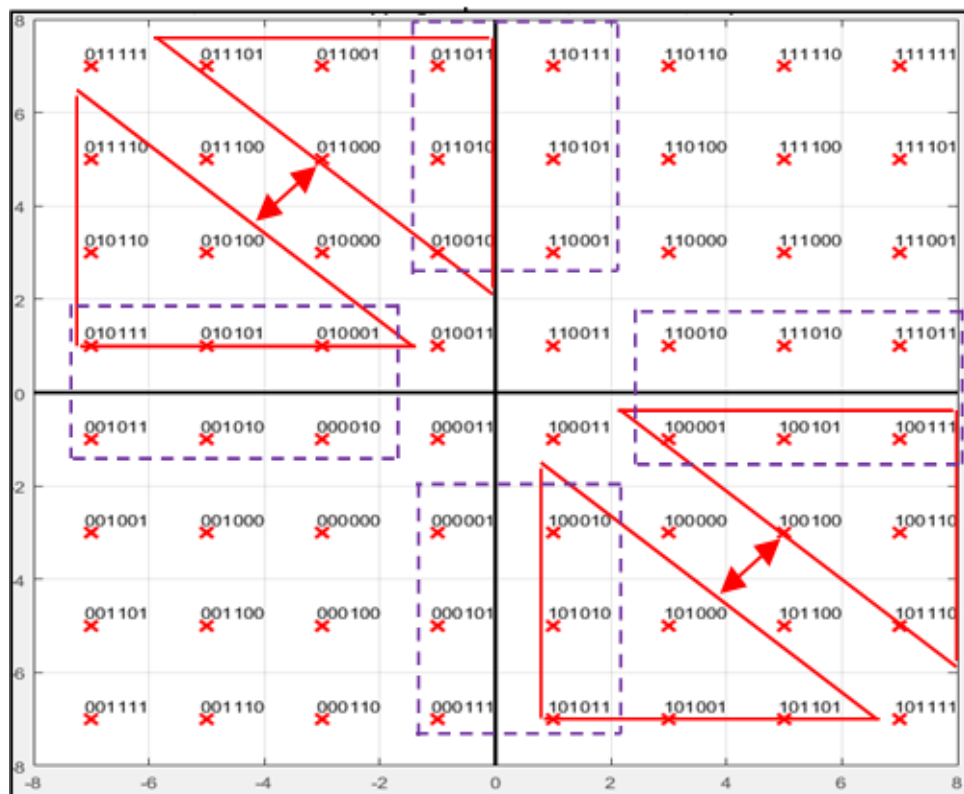


Fig. 3. 9: Non-Gray coded 64-QAM.

the precoder is D6 D5 D3 D4 D1 D2. If  $D5 = D6$ , i.e., if the third QPSK modulator operates in the 1<sup>st</sup> and 3<sup>rd</sup> quadrants, the precoder output is: D6 D5 D4 D3 D2 D1. The 64-QAM precoder can be implemented using one XOR gate and two switches as illustrated in Fig. 3.10a. Fig. 3.10b displays the way that the output of the 64-QAM should look like after applying the precoder.

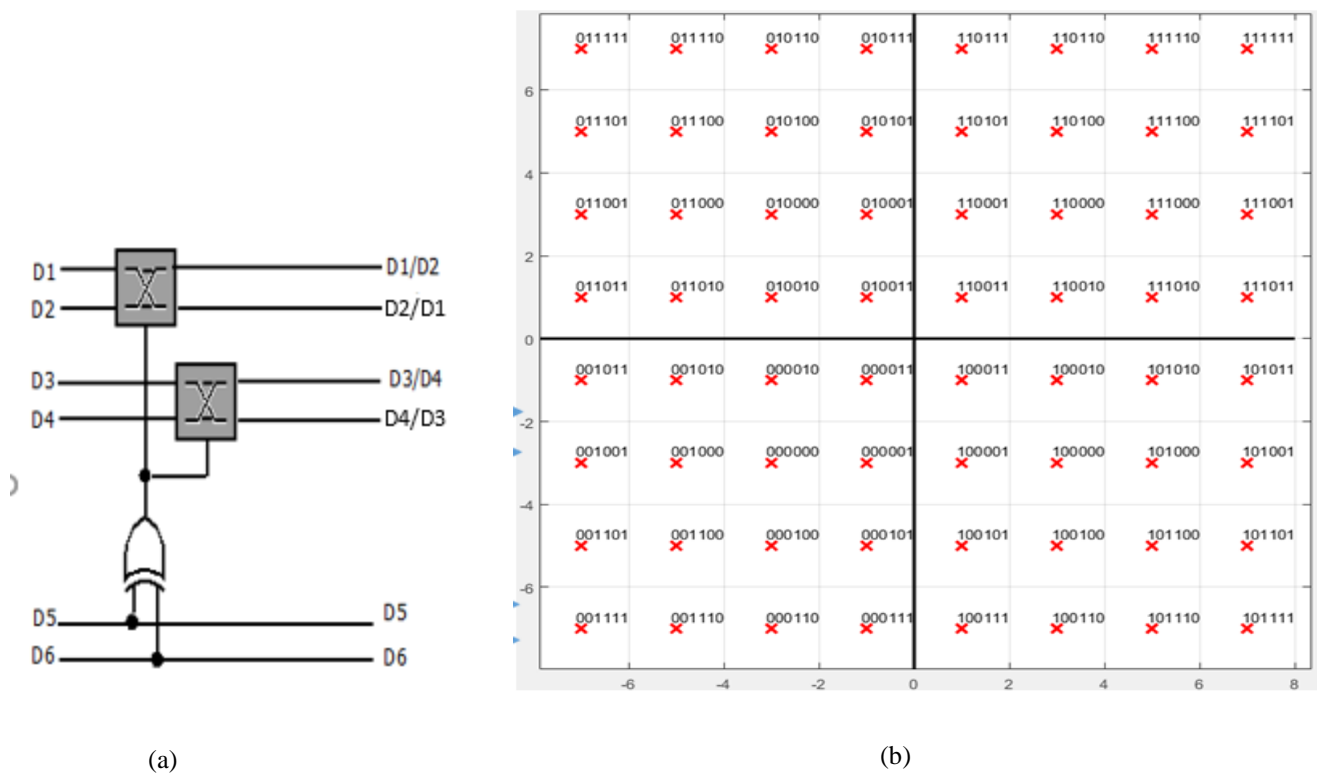


Fig. 3. 10: (a) 64-QAM precoder; (b) Gray coded 64-QAM constellation.

Higher-order square M-QAM transmitters, can be configured in a similar manner by scaling the above design accordingly with  $N$  tandem QPSK modulators, where  $M = 4^N$ , and  $N - 1$  nested precoders that consists of  $N(N - 1)/2$  switches. Therefore, 265-QAM transmitter can be obtained by scaling up the 64-QAM design accordingly with the fourth tandem QPSK modulator as shown in Fig. 3.11. Here again, the 265-QAM precoder would

switch the 64-QAM binary symbol at the output of the 64-QAM precoder (D1 and D2, D3 and D4, D5 and D6, respectively) into the 64-QAM transmitter in Fig. 3.8 if the fourth QPSK modulator operates in the 2<sup>nd</sup> or 4<sup>th</sup> quadrants according to the most significant bits D7 and D8.

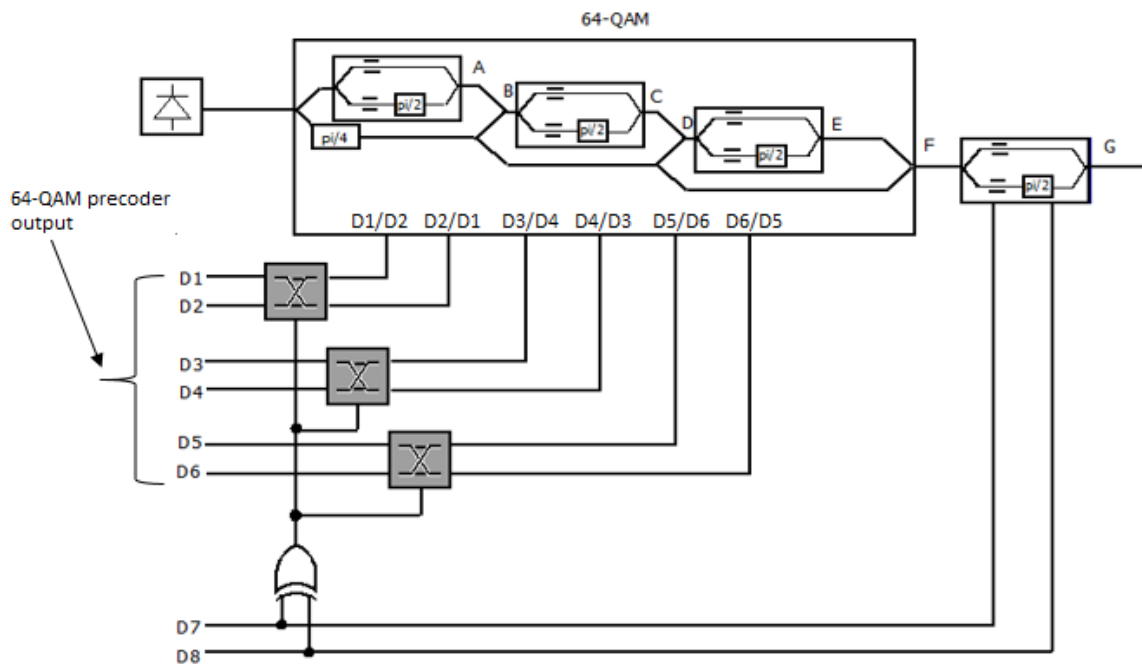


Fig. 3.11: Optical circuit diagram for 256-QAM.

### 3.6. Conclusion

We have proposed M-ary QAM optical transmitter driven by binary electrical signals. The design utilizes multiple QPSK modulators in tandem driven by binary electrical signals. It also provides a scalable configuration that can be scaled to any order of M-ary QAM and allows Gray coded symbol constellation to insure the lowest bit error rate possible.

## CHAPTER 4: DESIGNING THE COUPLING RATIOS FOR PROPER CONSTELLATIONS AND ANALYZING THE IMPACT OF COUPLING AND PHASE ERRORS

### 4.1. Introduction

The coupling ratios for the proposed M-ary QAM transmitter should be set to the correct values in order to obtain proper constellations with equally spaced symbols. This chapter provides the design for the correct coupling ratios taking into consideration the insertion loss of the optical components. It also analyzes the transmitters by evaluating the impact of coupling ratio errors as well as the phase errors on the resulting constellation diagrams.

### 4.2. Designing the coupling ratio for 16-QAM transmitter

Fig.4.1 shows the optical circuit diagram for the proposed 16-QAM transmitter employing two QPSK modulators in push-pull configuration. The four streams of binary data D1-D4 are the outputs from the Gray precoder described in Chapter 3. The optical coupler or splitter (SP1) with coupling ratio  $S1 = \alpha_1/(1 - \alpha_1)$ , where  $\alpha_1$  is the percentage of power

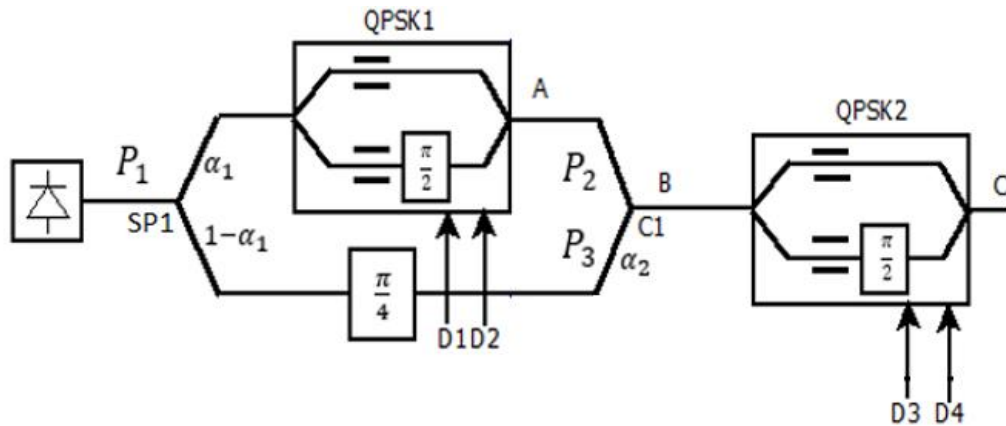


Fig. 4. 1: Optical circuit diagram for 16-QAM optical transmitter.

coupled to the upper arm of SP1, and the input power ratio to the combiner C1 ( $P_2/P_3$ ) are crucial for achieving a proper 16-QAM constellation.

SP1 splits the source optical carrier power  $P_1$  into two components. The 4-QAM signal constellation (point A) based on D1 and D2 is generated by QPSK1 in the upper arm with I/Q coordinate values  $(-1, 1)$  as shown in Fig. 4.2a. C1 combines the 4-QAM output signal power  $P_2$  at point A with the  $\pi/4$  phase-shifted carrier power  $P_3$  at the output of SP1 in the lower arm, generating the offset 4-QAM in the 1<sup>st</sup> quadrant (point B) with I/Q coordinate values  $(1, 3)$  as illustrated in Fig. 4.2b. QPSK2 rotates the offset constellation at point B to the four quadrants based on D3 and D4, thus generating a square 16-QAM constellation (point C) with the I/Q coordinate values  $(-3, -1, 1, 3)$  as shown in Fig. 4.2c.

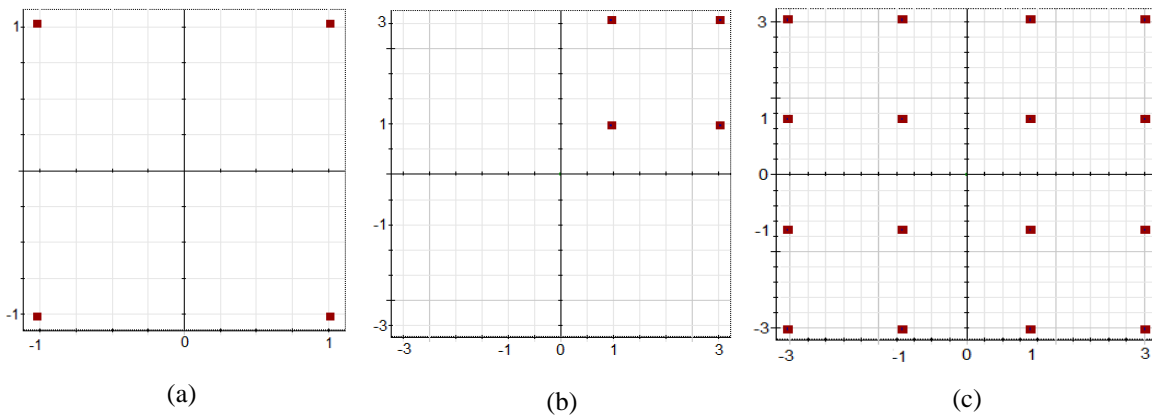


Fig. 4. 2: (a) 4-QAM; (b) 4-QAM shifted to the first quadrant; (c) 16-QAM.

The average power for the 4-QAM signal in Fig. 4.2a is  $P_2 = (1^2 + 1^2) = 2$ . Similarly, the average power for the 16-QAM signal in Fig. 4.2c is  $P_4 = [(1^2 + 1^2) + (1^2 + 3^2) + (3^2 + 1^2) + (3^2 + 3^2)]/4 = 10$ . In order to shift the 4-QAM constellation (Fig. 4.2a) to the first quadrant (Fig. 4.2b), the  $\pi/4$  phase-shifted carrier must be  $2\sqrt{2} \times e^{j\frac{\pi}{4}}$ , i.e., a

carrier power of  $P_3 = (2\sqrt{2})^2 = 8$ . Accordingly, the power ratio at the inputs of C1 should be set to  $P_2/P_3 = 1/4$  in order to achieve a proper 16-QAM constellation.

Let  $\beta$ ,  $K$ , and  $L$  denote, respectively, the insertion loss of each QPSK modulator, the  $\pi/4$  phase shifter, and the optical coupler/combiner. The goal is to design the coupling ratio that establishes  $P_2/P_3 = 1/4$  and takes into account the insertion loss of the optical components.

From the optical circuit diagram in Fig. 4.1, the laser power  $P_1$  is split into two components:  $P_1 (\alpha_1 L)$  and  $P_1 (1 - \alpha_1)L$  in the upper and lower arms of SP1 respectively.  $P_1 (\alpha_1 L)$  is applied to QPSK1, generating a QPSK signal with a power of  $P_2 = P_1 \alpha_1 L \beta$ . While  $P_1 (1 - \alpha_1)L$  is shifted by  $\pi/4$  obtaining  $P_3 = P_1 (1 - \alpha_1)LK$ . The power ratio  $P_2/P_3$  can then be obtained as:

$$\frac{P_2}{P_3} = \frac{P_1 \alpha_1 L \beta}{P_1 (1 - \alpha_1) L K} = \frac{\alpha_1 \beta}{(1 - \alpha_1) K} \quad (4.1)$$

Since  $P_2/P_3$  must be 1/4 for the proper 16-QAM constellation, the coupling ratio  $\alpha_1/(1 - \alpha_1)$  for SP1 can be determined from (4.1) as:

$$S1 = \frac{\alpha_1}{1 - \alpha_1} = \frac{1}{4} \left( \frac{K}{\beta} \right) \quad (4.2)$$

### 4.3. Effect of coupling ratio error

Deviation from the correct  $S1$  would introduce displacement to the shifted 4-QAM symbols thus distorts the targeted 16-QAM constellation. In practice, coupling ratio errors would occur during the fabrication process. For couplers fabricated using silicon-on-insulator

(SOI) technology for instance, the lithography and etching of SOI waveguide result in rough sidewalls of waveguides. The roughness leads to scattering and back reflections at the sidewalls, which in return cause error in the coupling ratio [88, 89].

Fig. 4.3 shows the 4-QAM, shifted 4-QAM, and the resulting 16-QAM constellations respectively for 10% increment in  $S1$ . As can be seen, the increment in  $\alpha_1$  leads to increment in  $P_2$  (see Fig. 4.1) thus expands the QPSK symbols in Fig. 4.3a. The corresponding reduction in  $P_3$  with  $(1 - \alpha_1)$  would result in displacement of the shifted 4-QAM closer to I axis as shown in Fig. 4.3b. The mapping of the displaced 4-QAM with QPSK2 would result in the distorted 16-QAM constellation as shown in Fig. 4.3c. Notice that the distances between the resulting symbols of the 16-QAM constellation are not equal.

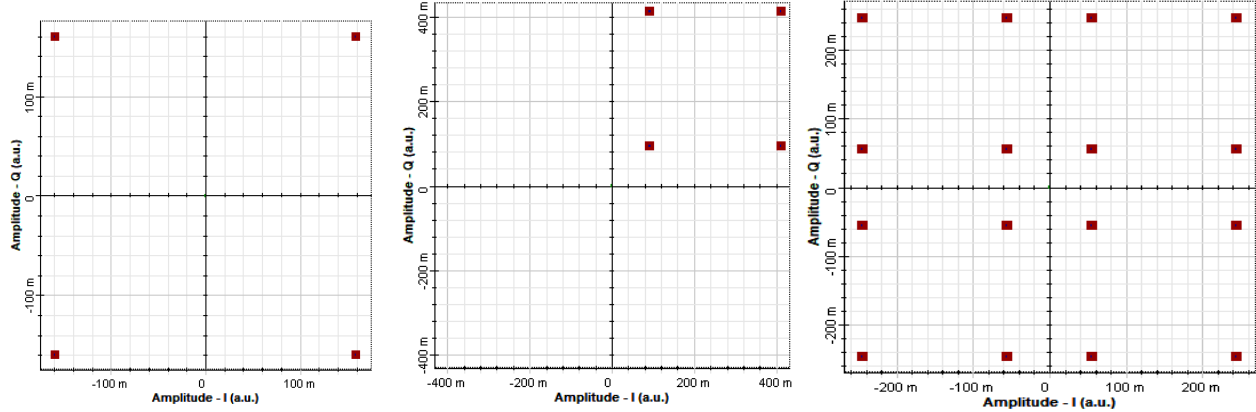


Fig. 4. 3: Effect of 10% errors in  $S1$  on: (a) 4-QAM; (b) 4-QAM shifted to the first quadrant; (c) 16-QAM.

To find the coupling ratio value at which the change in  $S1$  would have a minimum impact on  $P_2/P_3$  and thus on the resulting constellation diagrams, we take the derivative of  $(P_2/P_3)$  in (4.1) with respect to  $\alpha_1$  as follows:

$$\frac{\partial(\frac{P_2}{P_3})}{\partial\alpha_1} = \frac{(1-\alpha_1)K\beta - (\alpha_1\beta(-K))}{(1-\alpha_1)^2K^2} = \frac{(1-\alpha_1)K\beta}{(1-\alpha_1)^2K^2} + \frac{\alpha_1\beta K}{(1-\alpha_1)^2K^2} \quad (4.3)$$

Simplifies to:

$$\frac{\partial(\frac{P_2}{P_3})}{\partial\alpha_1} = \frac{\beta}{(1-\alpha_1)K} + \left(\frac{\alpha_1\beta}{(1-\alpha_1)K}\right) \frac{1}{1-\alpha_1} \quad (4.4)$$

Multiplying the term  $\frac{\beta}{(1-\alpha_1)K}$  by  $\alpha_1/\alpha_1$  yields:

$$\frac{\partial(\frac{P_2}{P_3})}{\partial\alpha_1} = \frac{\alpha_1\beta}{(1-\alpha_1)K} \left(\frac{1}{\alpha_1}\right) + \left(\frac{\alpha_1\beta}{(1-\alpha_1)K}\right) \frac{1}{1-\alpha_1} \quad (4.5)$$

Substituting  $\frac{\partial(\frac{P_2}{P_3})}{\partial\alpha_1}$  in (4.1) into (4.5) yields:

$$\frac{\partial(\frac{P_2}{P_3})}{\partial\alpha_1} = \frac{P_2}{P_3} \left(\frac{1}{\alpha_1}\right) + \left(\frac{P_2}{P_3}\right) \frac{1}{1-\alpha_1} = \left(\frac{P_2}{P_3}\right) \left(\frac{1}{\alpha_1} + \frac{1}{1-\alpha_1}\right) = \left(\frac{P_2}{P_3}\right) \left(\frac{1}{\alpha_1(1-\alpha_1)}\right) \quad (4.6)$$

Therefore,

$$\frac{\partial(\frac{P_2}{P_3})}{\partial\alpha_1} = \left(\frac{P_2}{P_3}\right) \left(\frac{1}{\alpha_1(1-\alpha_1)}\right) \quad (4.7)$$

Since  $P_2/P_3$  must be 1/4 for the proper 16-QAM constellation, the change of  $P_2/P_3$  with  $\alpha_1$  can then be determined as:

$$\frac{\partial(\frac{P_2}{P_3})}{\partial\alpha_1} = \left(\frac{1}{4}\right) \left(\frac{1}{\alpha_1(1-\alpha_1)}\right) \quad (4.8)$$

Fig. 4.4 plots  $\partial(P_2/P_3)/\partial\alpha_1$  as  $\alpha_1$  changes from 0.01 to 0.99. As can be seen, the rate of change increases exponentially for values of  $\alpha_1$  that are less than 0.3 or higher than 0.7. It

also shows that the rate of change is minimum and almost constant for  $\alpha_1$  between 0.3 and 0.7. We conclude that the design which results in  $\alpha_1$  close to 0.5 would be less sensitive to the coupling ratio error.

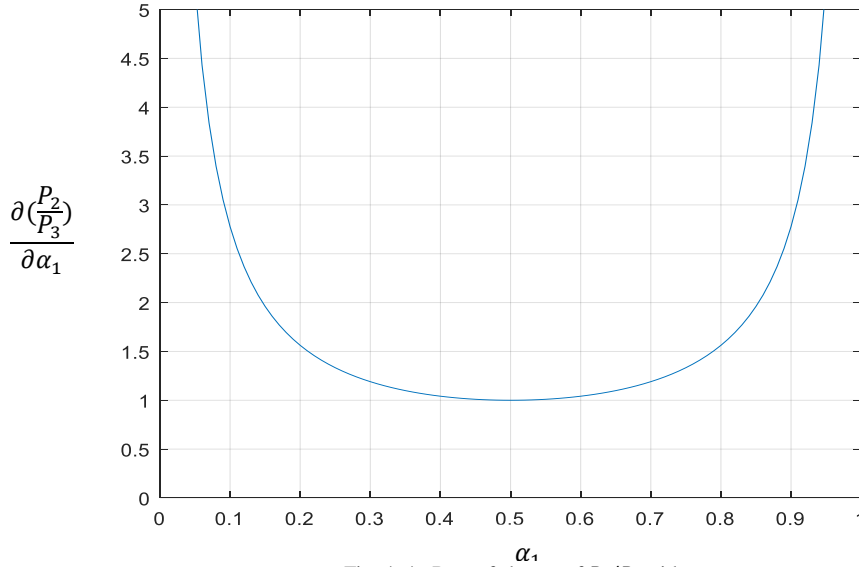


Fig. 4. 4: Rate of change of  $P_2/P_3$  with  $\alpha_1$ .

#### 4.4. Effect of phase errors

In order to obtain proper 16-QAM constellation from the 16-QAM transmitter in Fig. 4.5, the phase shift between  $P_2$  and  $P_3$  must be  $\pi/4$ . In practice however, phase shifters fabricated using LiNbO3 substrate would introduce biasing errors and thus phase errors due to the pyro-electric, photorefractive and photoconductive phenomena that take action in the LiNbO3 [89]. In addition, phase errors could occur due to the length mismatch between  $L_1$  and  $L_2$  caused by various imperfections like waveguide non-uniform doping profiles, waveguide material inhomogeneity, and manufacturing tolerances [88]. The phase error ( $\Delta\phi_{16QAM}$ ) between  $P_2$  and  $P_3$  would rotate the optical carrier and displace the shifted 4-QAM symbols at point B as shown in Fig. 4.6a for instance when  $\Delta\phi_{16QAM} =$

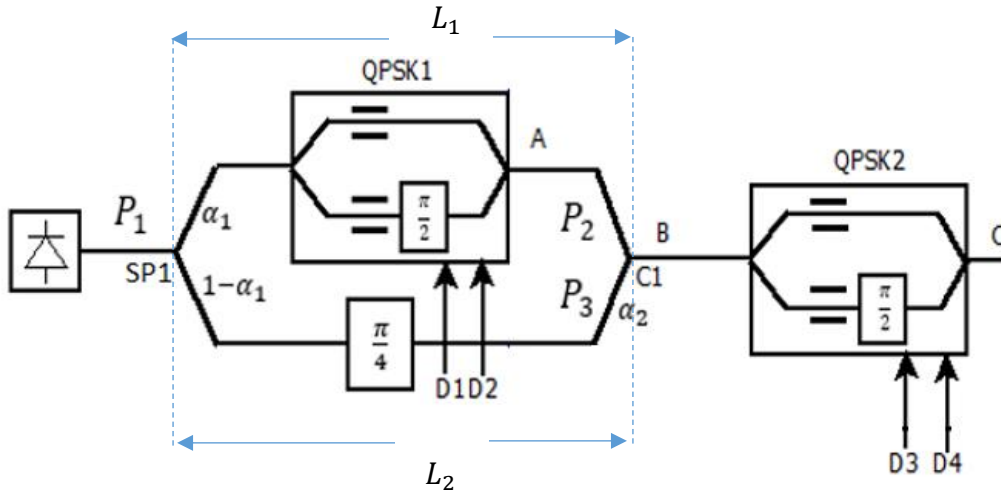


Fig. 4. 5: Optical circuit diagram for 16-QAM optical transmitter.

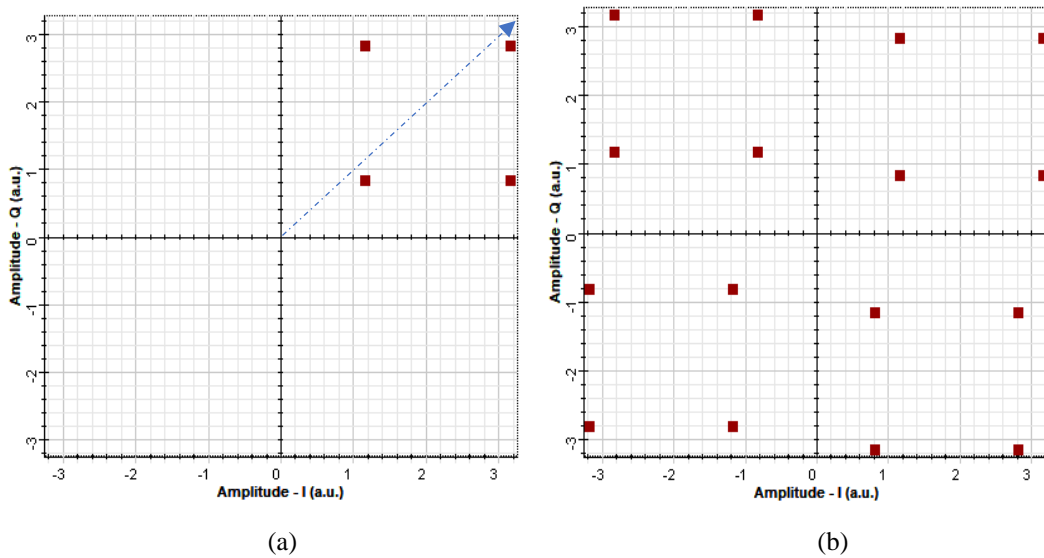


Fig. 4. 6: (a) shifted 4-QAM for  $\Delta\phi_{16QAM} = 5$  degrees.; (b) 16-QAM for  $\Delta\phi_{16QAM} = 5$  degrees.

5 degrees. The displaced constellation would be mapped by QPSK2 resulting in the distortion 16-QAM constellation as shown in Fig. 4.6b.

There are various techniques to compensate for phase errors. For instance, phase shifter in the arm  $L_2$  would adjust  $P_3$  and compensate for the phase errors  $\Delta\phi_{16-QAM}$ . Also, the

techniques described in chapter 2 for MZM phase error detection and correction could be adapted to control the errors in 16-QAM transmitter.

#### 4.5. Designing the coupling ratio for 64-QAM transmitter

The optical circuit diagram for the 64-QAM optical transmitter is shown in Fig 4.7. The coupling or power splitting ratios of SP1 and SP2,  $S1 = \alpha_1/(1 - \alpha_1)$  and  $S2 = \alpha_2/(1 - \alpha_2)$ , are responsible for setting the correct ratio of the input power to the combiners C1 ( $P_2/P_3$ ) and C2 ( $P_4/P_5$ ), in order to achieve a proper 64-QAM constellation with equally-spaced symbols.

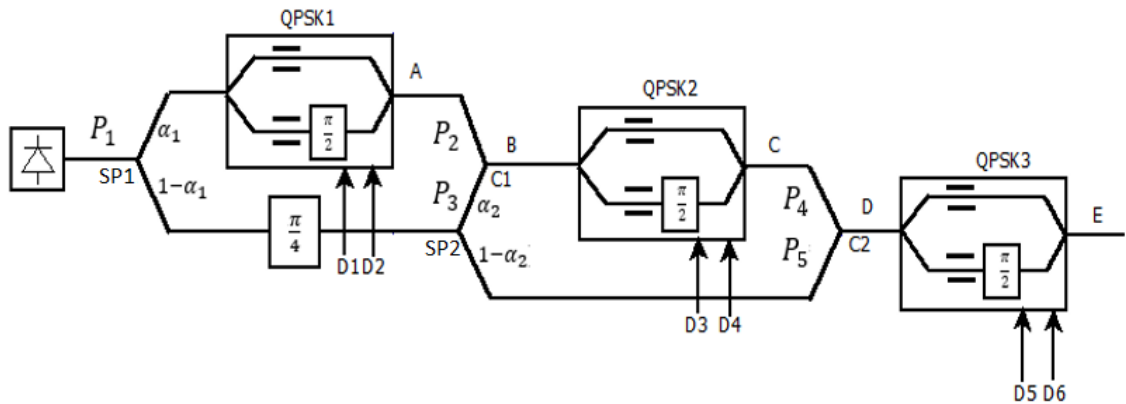


Fig. 4. 7: Optical circuit diagram for 64-QAM.

The constellations in Fig. 4.8a, Fig. 4.8b, and Fig.4.8c are generated at different points in the 16-QAM transmitter as described in Section 4.2. Therefore, the average power for the 4-QAM in Fig. 4.8a is  $P_2 = 2$ . Also, the average power for the 16-QAM signal in Fig. 4.8c is  $P_4 = 10$ . In order to shift the 4-QAM constellation (Fig. 4.8a) to the first quadrant

(Fig. 4.8b), the  $\pi/4$  phase-shifted carrier should have power of  $P_3 = (2\sqrt{2})^2 = 8$  .

Similarly, the  $\pi/4$  phase-shifted carrier of  $4\sqrt{2} \times e^{j\frac{\pi}{4}}$ , corresponding to a carrier power

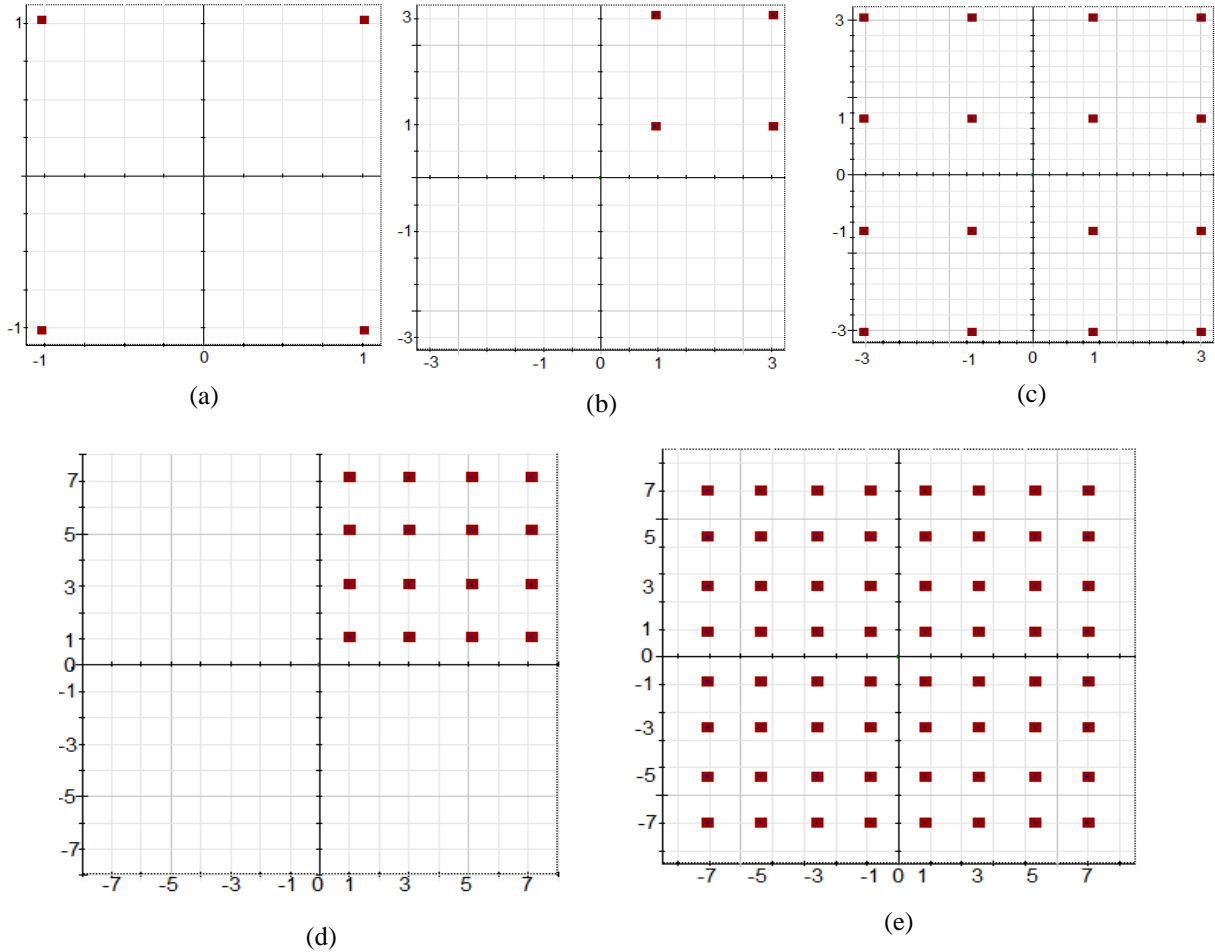


Fig. 4. 8: (a) 4-QAM; (b) 4-QAM shifted to the first quadrant; (c) 16-QAM; (d) 16-QAM shifted to the first quadrant; (e) 64-QAM.

of  $P_5 = (4\sqrt{2})^2 = 32$ , would be required to shift the 16-QAM constellation (Fig. 4.8c) to the first quadrant (Fig. 4.8d). Accordingly, the power ratios at the inputs to C1 and C2 should be set to  $P_2/P_3 = 1/4$ ,  $P_4/P_5 = 1/3.2$ , respectively, in order to achieve a proper 64-QAM constellation.

Again, let  $\beta$ ,  $K$ , and  $L$  denote, respectively, the insertion loss of each QPSK modulator, the  $\pi/4$  phase shifter, and the optical couplers/combiners. The goal is to design the coupling ratios that establish the correct values for  $P_2/P_3$  and  $P_4/P_5$  and take into account the insertion loss of the optical components.

From the optical circuit diagram in Fig. 4.7, the laser power  $P_1$  is split into two components:  $P_1 (\alpha_1 L)$  and  $P_1 (1 - \alpha_1)L$  in the upper and lower arms of SP1 respectively.  $P_1 (\alpha_1 L)$  is applied to QPSK1, generating a QPSK signal with a power of  $P_2 = P_1 \alpha_1 L \beta$ . While  $P_1 (1 - \alpha_1)L$  is shifted by  $\pi/4$  and then applied to SP2 obtaining  $P_3 = P_1 (1 - \alpha_1)LK\alpha_2 L = P_1 (1 - \alpha_1)\alpha_2 L^2 K$  in the upper arm, and  $P_5 = P_1 (1 - \alpha_1)LK(1 - \alpha_2)L = P_1(1 - \alpha_1)(1 - \alpha_2)L^2 K$  in the lower arm. The combination of  $P_2$  and  $P_3$  is applied to QPSK2, generating the 16-QAM signal with power  $P_4 = (P_2 + P_3)L\beta = P_1[\alpha_1 L^2 \beta^2 + (1 - \alpha_1)\alpha_2 L^3 K \beta]$ .

The power ratio  $P_2/P_3$  can then be obtained as:

$$\frac{P_2}{P_3} = \frac{P_1 \alpha_1 L \beta}{P_1 (1 - \alpha_1)\alpha_2 L^2 K} = \frac{\alpha_1 \beta}{(1 - \alpha_1)\alpha_2 L K} \quad (4.9)$$

Since  $P_2/P_3$  must be 1/4 for the proper 64-QAM constellation, the coupling ratio  $\alpha_1/(1 - \alpha_1)$  for SP1 can be determined from (4.9) as:

$$S1 = \frac{\alpha_1}{1 - \alpha_1} = \frac{1}{4} \left( \frac{\alpha_2 L K}{\beta} \right) \quad (4.10)$$

Comparing (4.9) and (4.2), we notice that splitting the carrier power with SP2 for the 64-QAM makes  $S1$  dependent on  $L$ .

A similar calculation for the power ratio  $P_4/P_5$  yields:

$$\frac{P_4}{P_5} = \frac{1}{3.2} = \frac{P_1[\alpha_1 L^2 \beta^2 + (1 - \alpha_1) \alpha_2 L^3 K \beta]}{P_1(1 - \alpha_1)(1 - \alpha_2)L^2 K} \quad (4.11)$$

Dividing both the numerator and the denominator by  $(1 - \alpha_1) \alpha_2 L^3 K \beta$  results in:

$$\frac{P_4}{P_5} = \frac{(\alpha_1 \beta) / ((1 - \alpha_1) \alpha_2 L K) + 1}{(1 - \alpha_2) / (\alpha_2 L \beta)} = \frac{P_2/P_3 + 1}{(1 - \alpha_2) / (\alpha_2 L \beta)} \quad (4.12)$$

Where we have used the expression for  $P_2/P_3$  in (4.9)

The coupling ratio  $\alpha_2/(1 - \alpha_2)$  for SP2 can then be determined as:

$$\frac{\alpha_2}{1 - \alpha_2} = \frac{P_4}{P_5} \left( \frac{1}{1 + P_2/P_3} \right) \frac{1}{\beta L} = \frac{1}{3.2} \left( \frac{1}{1 + 1/4} \right) \left( \frac{1}{\beta L} \right) \quad (4.13)$$

Simplifying to:

$$S2 = \frac{\alpha_2}{1 - \alpha_2} = \frac{1}{4} \left( \frac{1}{\beta L} \right) \quad (4.14)$$

#### 4.6. Effect of coupling ratios errors

As described above, S1 and S2 are responsible for setting  $P_2/P_3 = 1/4$  and  $P_4/P_5 = 1/3.2$  respectively. Deviation from these ratios would result in a distorted 64-QAM constellation. Fig. 4.9 shows the constellation diagrams at points A, B, C, D, and E under presence of 10% increment in S1.

The increment in  $\alpha_1$  leads to increment in  $P_2$  (see Fig. 4.7) thus expands the QPSK symbols in Fig. 4.9a. The corresponding reduction in  $P_3$  with  $(1 - \alpha_1)$  would result in displacement

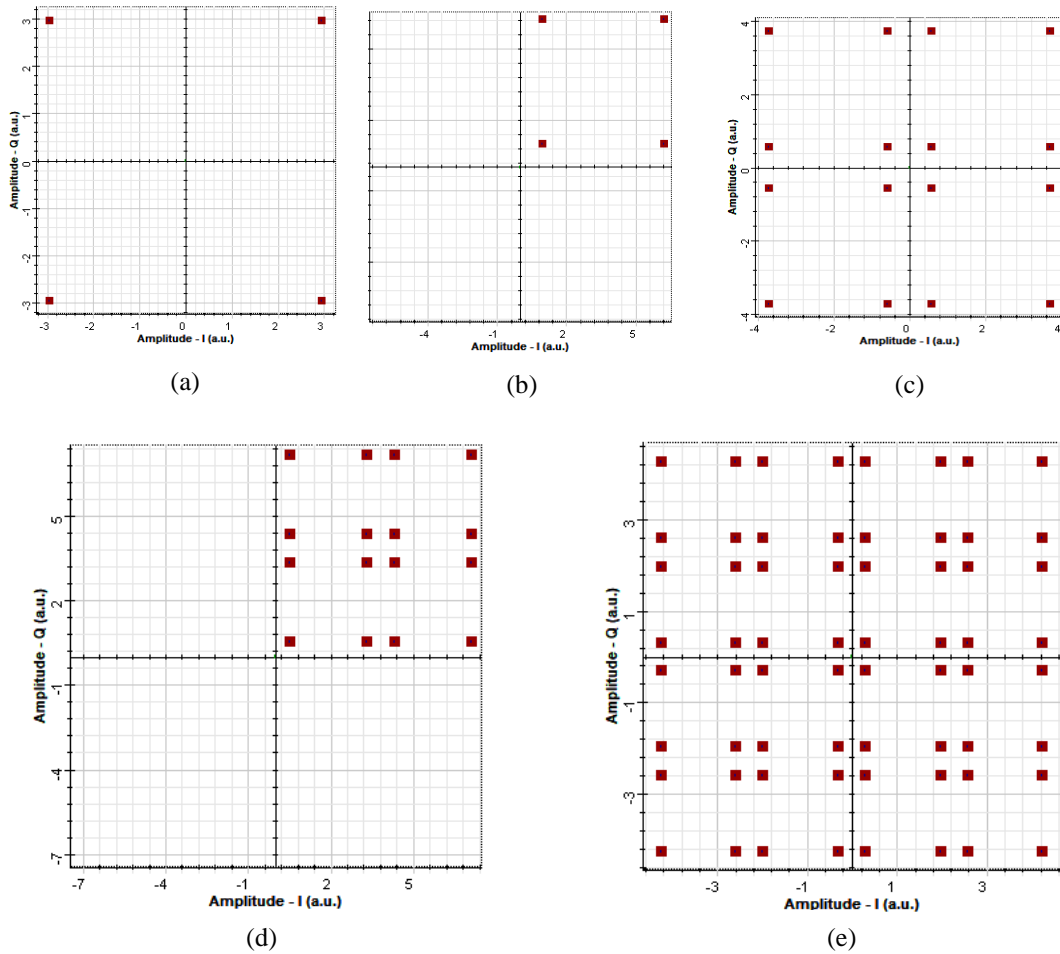


Fig. 4. 9: Effect of 10% error in S1 on: (a) 4-QAM; (b) 4-QAM shifted to the first quadrant; (c) 16-QAM; (d) 16-QAM shifted to the first quadrant; (e) 64-QAM.

of the shifted 4-QAM closer to I axis as shown in Fig. 4.9b. The mapping of the displaced 4-QAM with QPSK2 would result in the distorted 16-QAM constellation as shown in Fig. 4.9c. The reduction in  $P_3$  with  $(1 - \alpha_1)$  would also lead to reduction in  $P_5$  which would displace the shifted 16-QAM closer to I axis as shown in Fig. 4.9d. QPSK3 would map the distorted 16-QAM to the other quadrants resulting in the distorted 64-QAM constellation as shown in Fig. 4.9e.

The change in  $S_2$ , on the other hand, would displace the 16-QAM symbols and distort the 64-QAM constellations as shown in Fig. 10, where  $S_2$  is increased by 10%. The increment in  $\alpha_2$  leads to increment in  $P_4$  (see Fig. 4.7) thus expands the 16-QAM symbols as shown in Fig. 4.10a. The corresponding reduction in  $P_5$  with  $(1 - \alpha_2)$  would result in

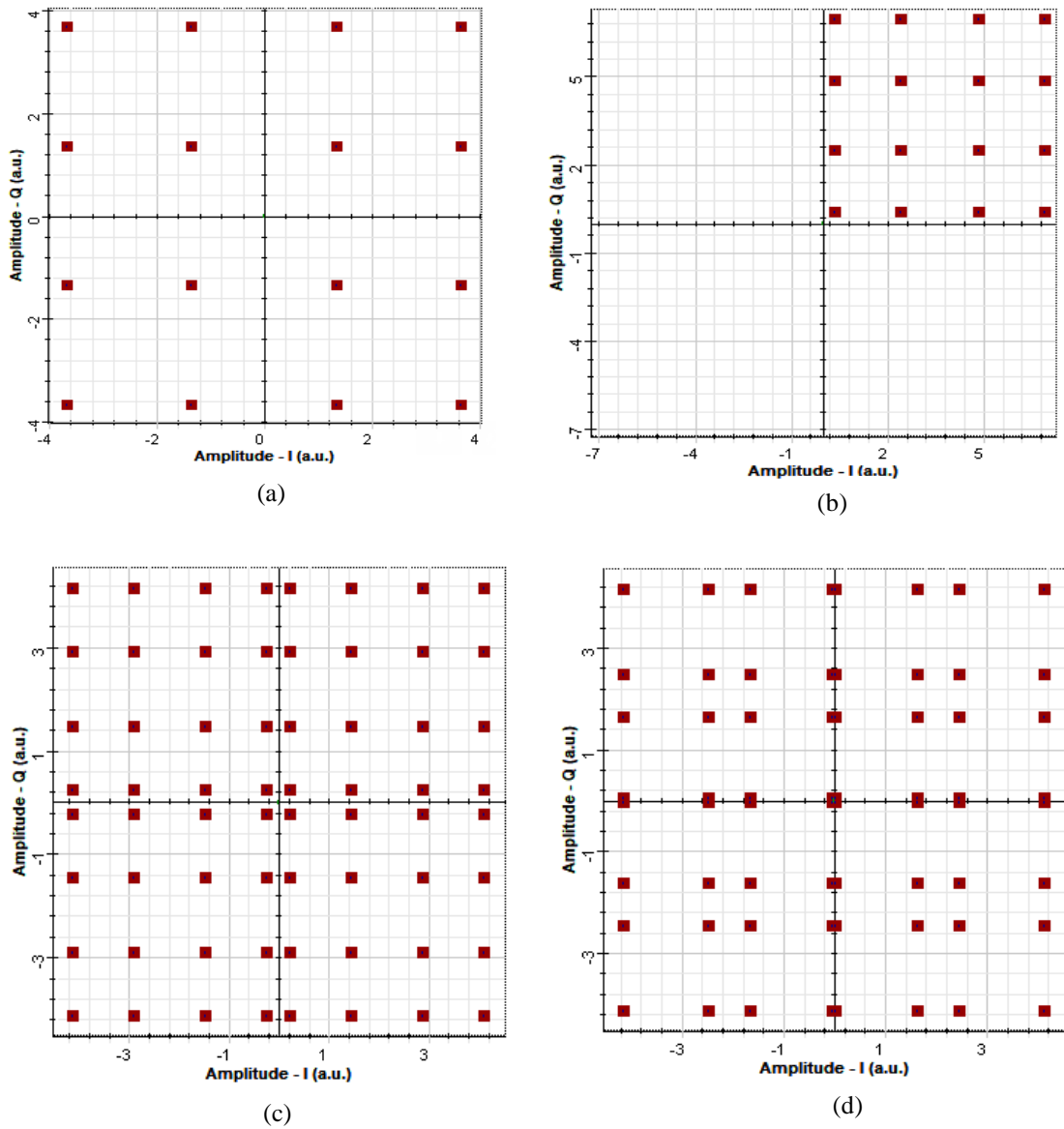


Fig. 4. 10: Effect of 10% error in  $S_2$  on: (a) 16-QAM, (b) 16-QAM shifted to the first quadrant; (c) 64-QAM. (d) 64-QAM for 10% error in  $S_1$  and  $S_2$ .

displacement of the shifted 16-QAM closer to I axis as shown in Fig. 4.10b. The mapping of the displaced 16-QAM with QPSK3 would result in the distorted 64-QAM constellation as shown in Fig. 4.10c. Fig. 4.10d shows the example 64-QAM constellation under presence of 10% phase errors in both S1 and S2. As can be seen, the distortion is worse with the symbols being displaced across the quadrant boundaries.

To find the coupling ratio values at which the change in  $S1$  and  $S2$  would have a minimum impact on  $P_2/P_3$  and thus on the resulting constellation diagrams, we take the derivative of  $(P_2/P_3)$  in (4.1) with respect to  $\alpha_1$  and  $\alpha_2$  as follows:

$$\frac{\partial(\frac{P_2}{P_3})}{\partial\alpha_2\alpha_1} = \frac{-(\alpha_1\beta(-KL))}{(1-\alpha_1)^2\alpha_2^2K^2L^2} = \frac{\alpha_1\beta}{(1-\alpha_1)^2\alpha_2^2LK} \quad (4.15)$$

Simplifies to:

$$\frac{\partial(\frac{P_2}{P_3})}{\partial\alpha_1\alpha_2} = \frac{\alpha_1\beta}{(1-\alpha_1)\alpha_2LK} \left(\frac{1}{1-\alpha_1}\right) \left(\frac{1}{\alpha_2}\right) \quad (4.16)$$

Since  $\frac{P_2}{P_3} = \frac{\alpha_1\beta}{(1-\alpha_1)\alpha_2LK} = \frac{1}{4}$  we obtain

$$\frac{\partial(\frac{P_2}{P_3})}{\partial\alpha_1\alpha_2} = \frac{P_2}{P_3} \left(\frac{1}{1-\alpha_1}\right) \left(\frac{1}{\alpha_2}\right) = \frac{1}{4} \left(\frac{1}{1-\alpha_1}\right) \left(\frac{1}{\alpha_2}\right) \quad (4.17)$$

Therefore

$$\frac{\partial(\frac{P_2}{P_3})}{\partial\alpha_1\alpha_2} = \frac{1}{4} \left(\frac{1}{1-\alpha_1}\right) \left(\frac{1}{\alpha_2}\right) \quad (4.18)$$

Similarly, the values of  $\alpha_1$  and  $\alpha_2$  within which the change in  $(P_4/P_5)$  would have minimum impact on the constellation diagram can be found by taking the derivative of (4.12) with respect to  $\alpha_1$  and  $\alpha_2$  as:

$$\frac{\partial(\frac{P_4}{P_5})}{\partial\alpha_1\alpha_2} = \frac{(\frac{1-\alpha_2}{\alpha_2 L\beta})(\frac{\partial(\frac{P_2}{P_3})}{\partial\alpha_1\alpha_2})}{(\frac{1-\alpha_2}{\alpha_2 L\beta})^2} = \frac{\partial(\frac{P_2}{P_3})}{\partial\alpha_1\alpha_2} \frac{(\frac{1-\alpha_2}{\alpha_2 L\beta})}{(\frac{1-\alpha_2}{\alpha_2 L\beta})} \quad (4.19)$$

Substituting  $\partial(\frac{P_2}{P_3})/\partial\alpha_1\alpha_2$  from (4.18) into (4.19) yields:

$$\frac{\partial(\frac{P_4}{P_5})}{\partial\alpha_1\alpha_2} = \frac{\frac{1}{4}(\frac{1}{1-\alpha_1})(\frac{1}{\alpha_2})}{(\frac{1-\alpha_2}{\alpha_2 L\beta})} = \frac{\frac{1}{4}}{((1-\alpha_1)(\frac{1-\alpha_2}{L\beta}))} = \frac{L\beta}{4(1-\alpha_1)(1-\alpha_2)} = (\frac{1}{16(1-\alpha_1)(1-\alpha_2)})(4L\beta) \quad (4.20)$$

Simplifying to:

$$\frac{\partial(\frac{P_4}{P_5})}{\partial\alpha_1\alpha_2} = (\frac{1}{16(1-\alpha_1)(1-\alpha_2)})(4L\beta) \quad (4.21)$$

Substituting  $4L\beta$  from (4.14) into (4.21) results in

$$\frac{\partial(\frac{P_4}{P_5})}{\partial\alpha_1\alpha_2} = (\frac{1}{16(1-\alpha_1)(1-\alpha_2)})(\frac{1-\alpha_2}{\alpha_2}) = \frac{1}{16(1-\alpha_1)\alpha_2} \quad (4.22)$$

Therefore

$$\frac{\partial(\frac{P_4}{P_5})}{\partial\alpha_1\alpha_2} = \frac{1}{16(1-\alpha_1)\alpha_2} \quad (4.23)$$

The 3D plots of (4.18) and (4.23) for  $\alpha_1$  and  $\alpha_2$  varying from 0.01 to 0.99 are shown in Fig. 4.11. As can be seen,  $\partial(P_2/P_3)/\partial\alpha_1\alpha_2$  as well as  $(P_4/P_5)/\partial\alpha_1\alpha_2$  decrease with the decrease in  $\alpha_1$  and the simultaneous increases in  $\alpha_2$ . It is also clear that the power ratio

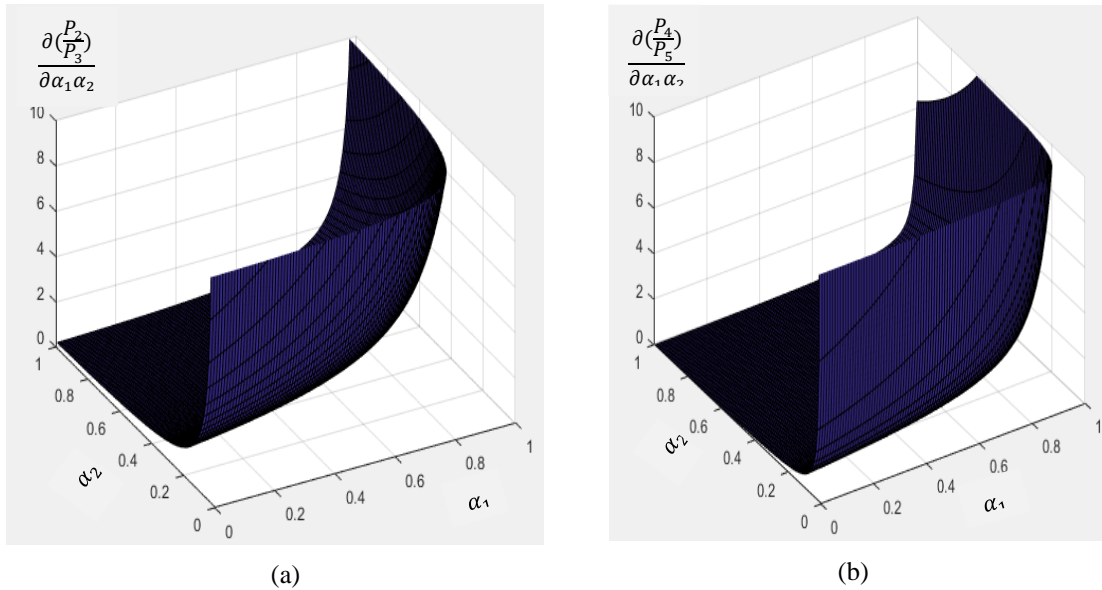


Fig. 4. 11: 3D plots of (a) change in  $\partial(P_2/P_3)/\partial\alpha_1\alpha_2$  with  $\alpha_1\alpha_2$ ; (b) change in  $\partial(P_4/P_5)/\partial\alpha_1\alpha_2$  with  $\alpha_1\alpha_2$ .

$P_2/P_3$  is more sensitive to the change in the coupling ratios as compared to  $P_4/P_5$ . Finally, the design which results in  $\alpha_1 < 0.3$  and  $\alpha_2 > 0.5$  would be less sensitive to the coupling errors.

#### 4.7. Effect of phase errors on the 64-QAM transmitter

In order to obtain proper 64-QAM constellation from the transmitter in Fig. 4.12, the phase shift between  $P_2$  and  $P_3$  as well as  $P_4$  and  $P_5$  must be  $\pi/4$ . In practice however, the phase shifters biasing variation and length mismatch between the arms  $L_1$  and  $L_2$  as well as  $L_3$  and  $L_4$  would introduce phase errors. The phase error ( $\Delta\phi_{16QAM}$ ) between  $P_2$  and  $P_3$  would rotate the optical carrier and displace the shifted 4-QAM symbols at point B, in Fig. 4.12, causing distortion to the 16-QAM and 64-QAM constellations at points C and E respectively. The phase errors ( $\Delta\phi_{64-QAM}$ ) between  $P_4$  and  $P_5$  would similarly displace the shifted 16-QAM symbols at point D causing distortion to the 64-QAM constellation at

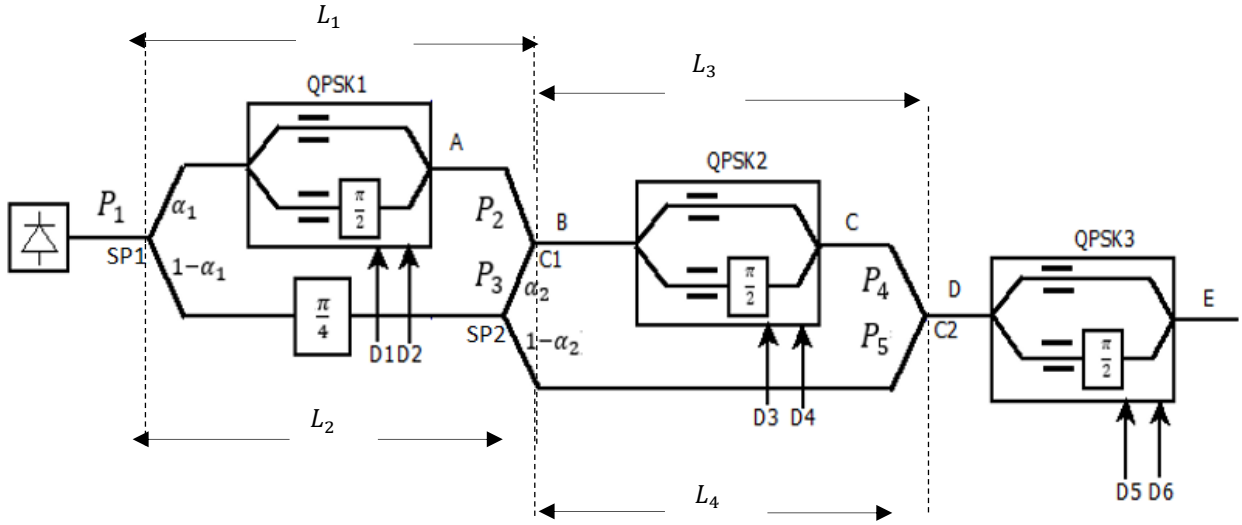


Fig. 4. 12: Optical circuit diagram for 64-QAM transmitter.

point E. Fig. 4.13 a show the symbol constellations at points B, D, and E for phase error  $\Delta\phi_{16QAM} = 5$  degrees. The displacement of the QPSK symbols in Fig. 4.13a is due to  $\Delta\phi_{16-QAM} = 5$  degrees that in turn distorts the 16-QAM symbols in each quadrant as well as the 64-QAM constellation as shown in Fig. 4.13b and Fig. 4.13c respectively. Similarly,  $\Delta\phi_{64-QAM} = 5$  degrees would displace the 16-QAM symbols in each quadrant as shown in Fig. 4.14a which in turn distorts the 64-QAM constellation as shown in Fig.

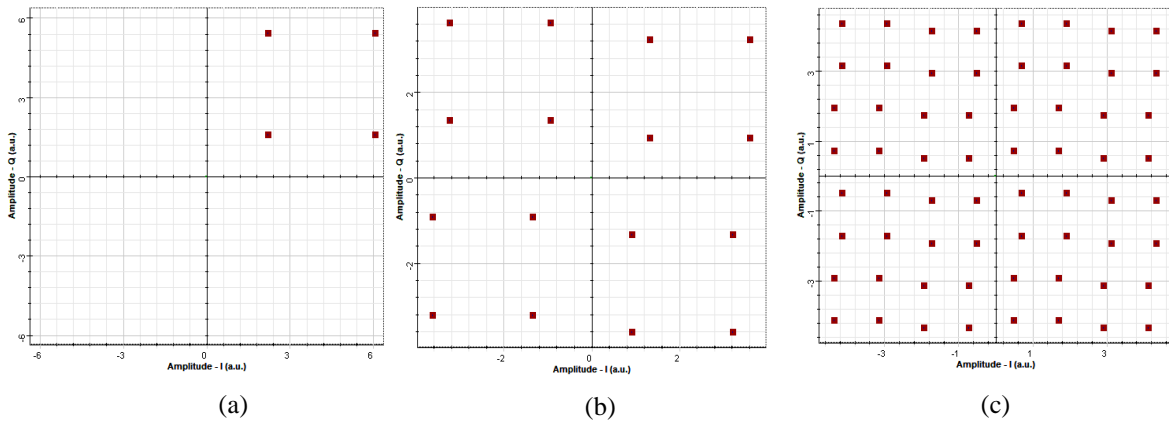


Fig. 4. 13: Effect of  $\Delta\phi_{64-QAM} = 5$  degrees on: (a) shifted 16-QAM; (b) 64-QAM. (c) 64-QAM for  $\Delta\phi_{16-QAM} = \Delta\phi_{64-QAM} = 5$  degrees

4.14b. It is clear that  $\Delta\phi_{64-QAM}$  causes constellation rotation around the center of 64-QAM constellation while  $\Delta\phi_{16-QAM}$  causes rotation around the center of the 16-QAM in each quadrant. This can be seen clearly in Fig. 4.14d where  $\Delta\phi_{16-QAM} = \Delta\phi_{64-QAM} = 5$  degrees.

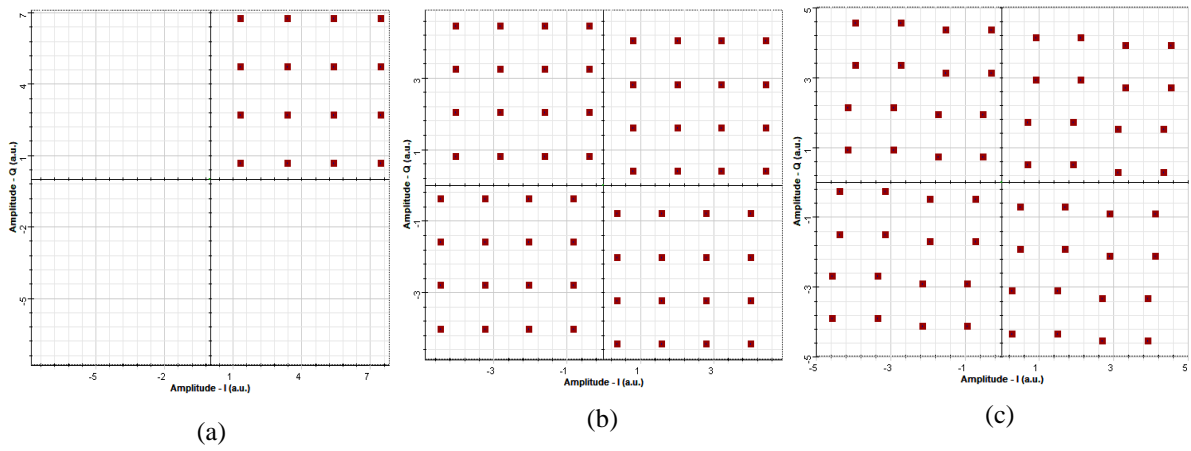


Fig. 4. 14: Effect of  $\Delta\phi_{16QAM} = 5$  degrees on: (a) shifted 4-QAM; (b) 16-QAM at point C; (c) 64-QAM.

## 4.8. Conclusion

We introduced the coupling ratios design required for proper 16-QAM and 64-QAM constellations taking into consideration the insertion loss of the optical components. We also analyzed the effect of coupling ratio errors and phase errors on the resulting constellation diagrams.

## CHAPTER 5: SIMULATION SETUP AND RESULTS

### 5.1. Introduction

The proposed configurations for the 16-QAM and 64-QAM transmitters have been constructed at 50 Gbaud in OptiSystem simulation software. The performance is evaluated under presence of additive white Gaussian noise (AWGN) as well as coupling and phase errors. This chapter describes the simulation setup and the obtained simulation results.

### 5.2. Simulation setup for 16-QAM transmitter

Fig. 5.1 shows the block diagram of the simulation setup for the back to back 16-QAM in OptiSystem. Each QPSK modulator is implemented using a sequence generator, two binary pulse generators, power splitter, two dual-drive MZM,  $\pi/2$  phase shifter, and power combiner as shown in Fig. 5.2.

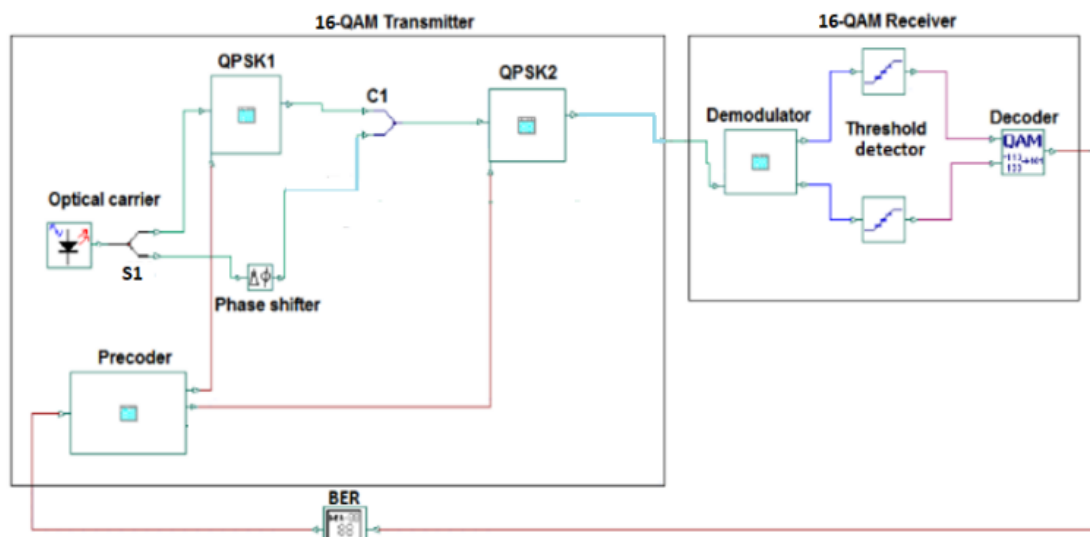


Fig. 5. 1: Simulation setup for 16-QAM.

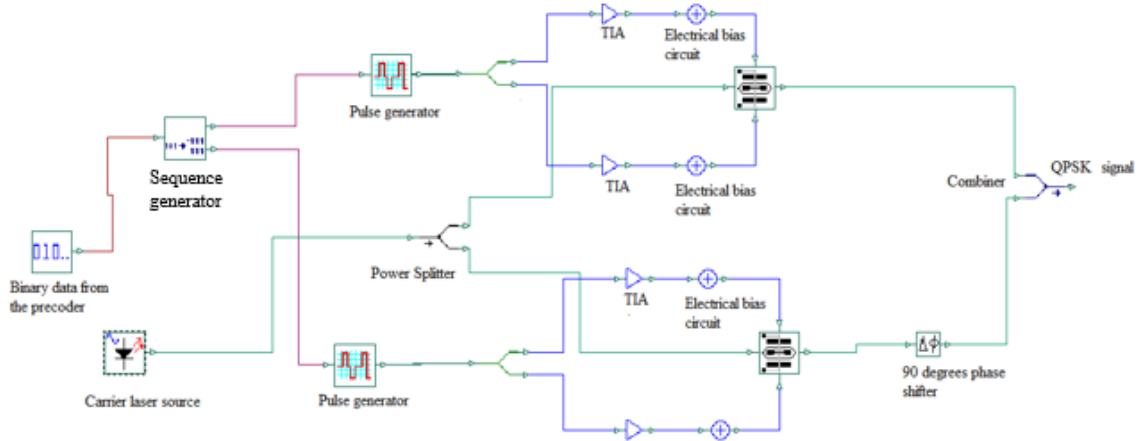


Fig. 5. 2: QPSK implementation in OptiSystem.

The sequence generator generates two parallel symbol sequences in-phase (I) and quadrature (Q) from the input binary data at the output of the precoder. Both I and Q components are applied to a binary pulse generator, driving amplifier, and electrical bias circuit to set the MZM driving voltage to 3V. Each of the MZM is biased at its null voltage of  $V_{\pi} = 3V$ . The 16-QAM precoder is implemented in a mapping circuit according to Table 5.1.

The transmitter output is applied to the quadrature hybrid demodulator of the coherent receiver operating under AWGN as shown in Fig. 5.1. The hybrid demodulator is implemented using a set of 3 dB optical couplers, local oscillator laser, with frequency and phase equal to those of the CW optical carrier, and a balanced photo detection scheme as illustrated in Fig. 5.3. The output current from the photo detectors is amplified using TIA and applied to I/Q threshold detector circuit followed by symbol decoder. The binary output data are compared to the input data to determine the BER as illustrated in Fig. 5.1.

Table 5.1: logic table for 16-QAM precoder

Precoder input	Precoder output
0000	0000
0001	0001
0010	0010
0011	0011
0100	0100
0101	0110
0110	0101
0111	0111
1000	1000
1001	1010
1010	1001
1011	1011
1101	1101
1110	1110
1111	1111

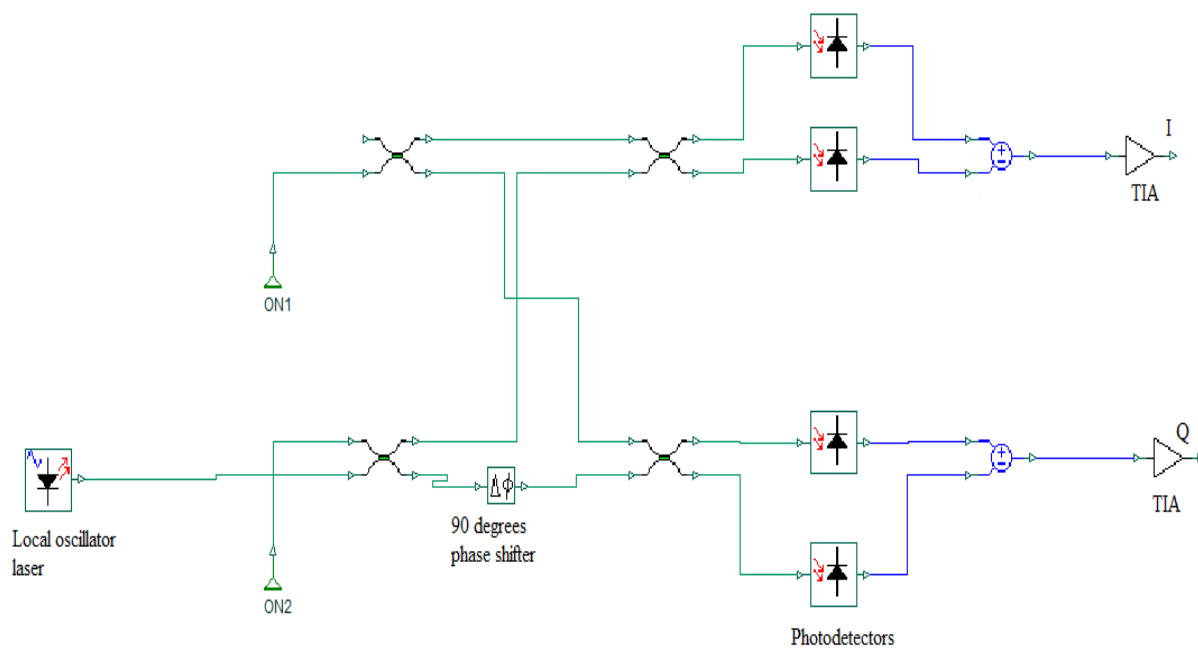


Fig. 5. 3: Demodulator implementation in OptiSystem.

### 5.2.1. 16-QAM transmitter performance

Equation (4.2) is used to design the required coupling ratio under the assumption that  $\beta = 4.5$  dB,  $K = 3$  dB as follows:

$$\frac{\alpha_1}{1 - \alpha_1} = \frac{1}{4} \left( \frac{K}{\beta} \right) = \frac{1}{4} \left( \frac{10^{-0.3}}{10^{-0.45}} \right) = 0.353$$

Simplifying to

$$\alpha_1 = 0.353 - 0.353\alpha_1 \rightarrow \alpha_1 = \frac{0.353}{1.353} = 0.26$$

Therefore, the coupling ratio required for proper 16-QAM constellation is

$$\frac{\alpha_1}{1 - \alpha_1} \approx \frac{0.26}{0.74} = \frac{26}{74}$$

The simulation setup in Fig. 5.1 is configured to reflect the values assumed in the example design. Fig. 5.4 displays the results of the back-to-back simulation for the Gray coded 16-QAM constellation at 14.5 dB Eb/No. As can be seen, the resulting symbol constellation

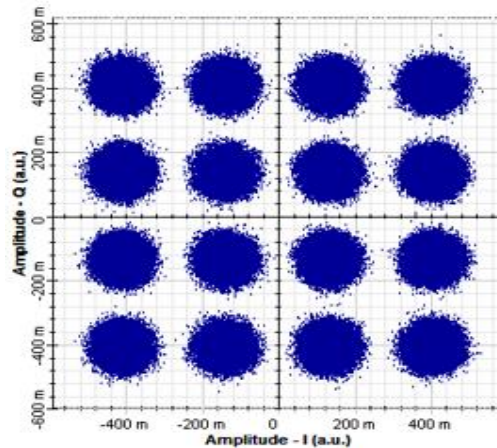


Fig. 5. 4: Constellation for proper 16-QAM.

is proper as expected. Also, the in-phase and quadrature eye diagrams are clear and uniform, reflecting the high quality of the generated 16-QAM signal as shown in Fig. 5.5.

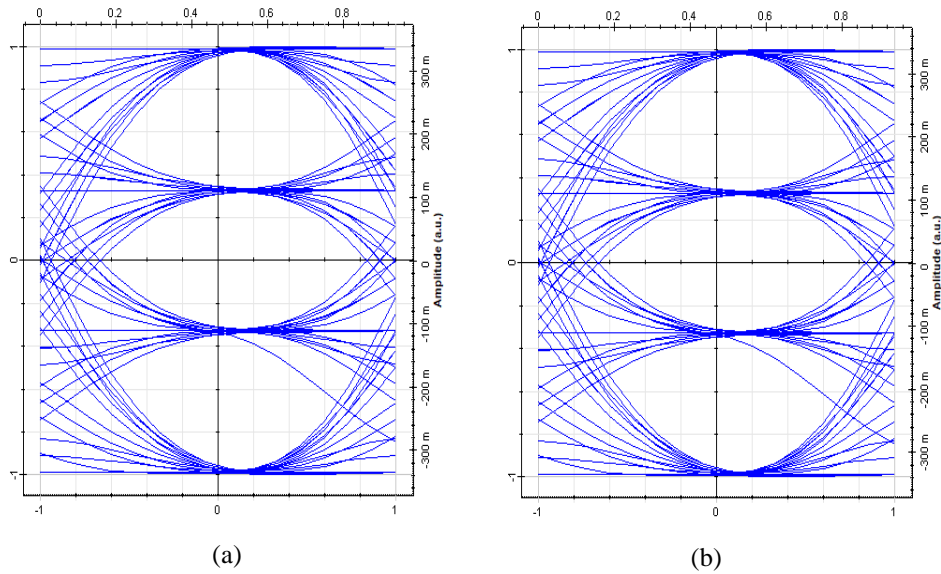


Fig. 5. 5: (a) Eye diagram for I signal; (b) Eye diagram for Q signal.

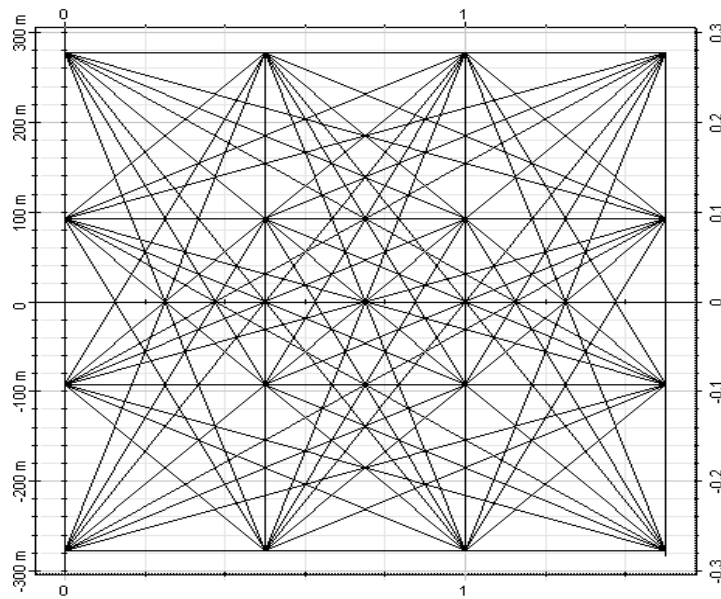


Fig. 5. 6: Symbol transitions.

Fig. 5.6 shows the example symbol transitions that are linear confirming that the QPSK modulators are biased in push-pull configuration.

Fig. 5.7 compares the BER performance to the theoretical 16-QAM. As can be seen, the proposed design has BER characteristics identical to the theoretical expectations.

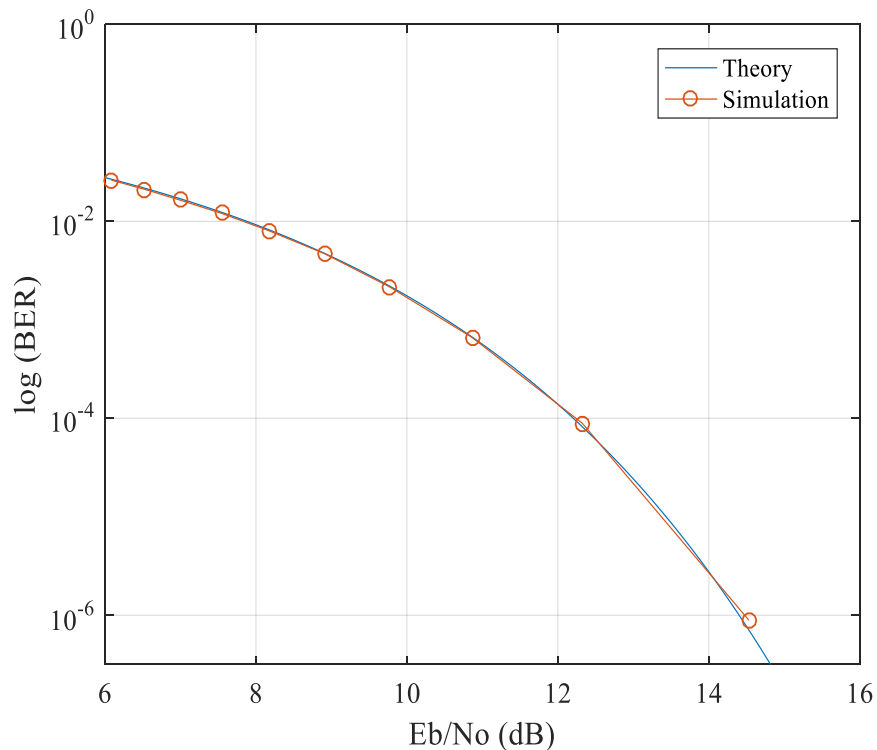


Fig. 5. 7: BER performance.

### 5.2.2. Impact of coupling ratio errors on 16-QAM performance

In practice, coupling ratio errors would occur during the fabrication process as described in Chapter 4. Since the coupling ratio,  $\alpha_1/(1 - \alpha_1)$ , is responsible for setting the power ratio at the inputs of combiner to the correct value, deviation from the correct ratio would produce constellation with unequally spaced symbols, resulting in higher BER.

Fig. 5.8a and Fig. 5.8b display the constellation diagrams for  $\mp 10\%$  and  $\pm 10\%$  coupling errors respectively (coupling ratios of 16/84 and 36/64). The collapse of the QPSK symbols in each quadrant in Fig. 5.8a is due to the decrement in  $\alpha_1$  while the expansion of the 16-QAM symbols is due to the corresponding increment of  $(1 - \alpha_1)$  as explained in Chapter 4. The opposite is true for the constellation diagram in Fig. 5.8b where  $\alpha_1/(1 - \alpha_1) = 36/64$ .

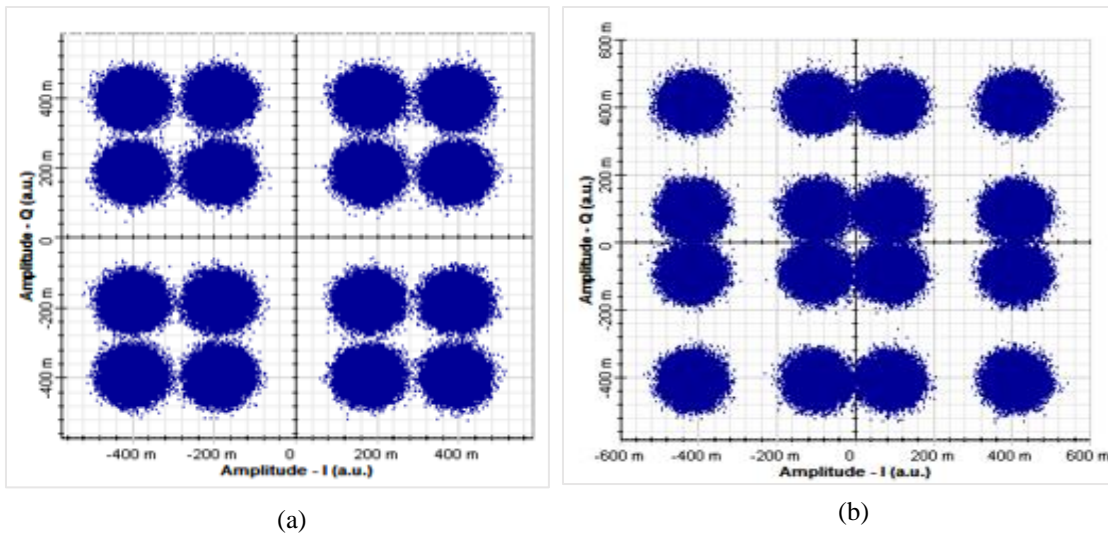


Fig. 5. 8: (a) Symbol constellation at 16/84 coupling ratio; (b) Symbol constellation at 36/64 coupling ratio.

Fig. 5.9 compares the BER performance at the correct coupling ratio (26/74) to the performance at the coupling ratios of 36/64 and 16/84. The plots show that the BER performance degrades due to incorrect coupling ratios as expected.

Fig. 5.10 shows the simulation results of the BER versus the coupling ratio at 14.5 dB Eb/No. As can be seen, the BER is minimum at the correct coupling ratio of 26/74. The BER increases as the coupling ratio deviates from the correct value since the constellation points are no longer equally spaced.

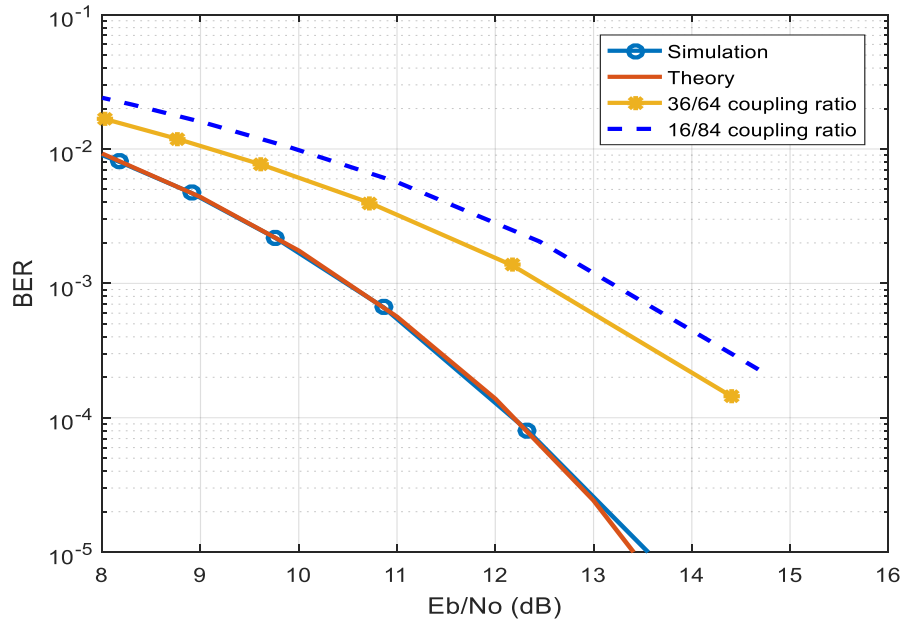


Fig. 5. 9: BER performance.

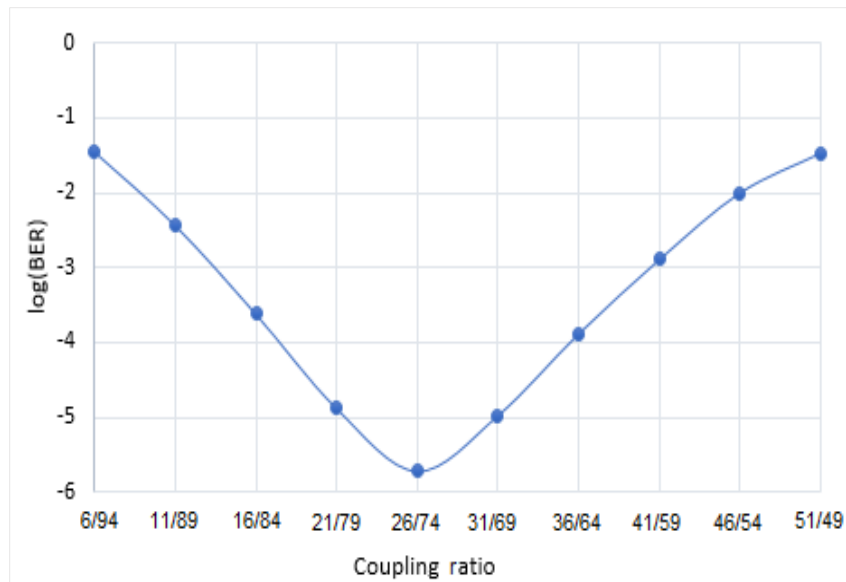


Fig. 5. 10: BER versus coupling ratio.

In practice however, the 26/74 coupler fabricated using SOI would exhibit an average error of  $\pm 2\%$  [88] thus a coupling ratio of 28/72. This small deviation in the coupling ratio would have a minor impact on the BER performance as can be seen from Fig. 5.10.

### 5.2.3. Impact of phase errors on 16-QAM performance

As explained in Chapter 4, obtaining proper 16-QAM constellation from the transmitter requires a phase shift of  $\pi/4$  between  $P_2$  and  $P_3$ . Since this is not practically possible, the phase error  $\Delta\phi_{16QAM}$  would rotate the optical carrier and displace the shifted 4-QAM symbols, causing distortion to the 16-QAM constellation.

Fig. 5.11 compares the 16-QAM constellations at 14.5 dB Eb/No with no phase errors to the constellation with  $\Delta\phi_{16QAM} = 5$  degrees. As can be seen, the displacement of the QPSK symbols in Fig. 5.11b (circle) is due to  $\Delta\phi_{16-QAM} = 5$  degrees that in turn distorts the 16-QAM constellation.

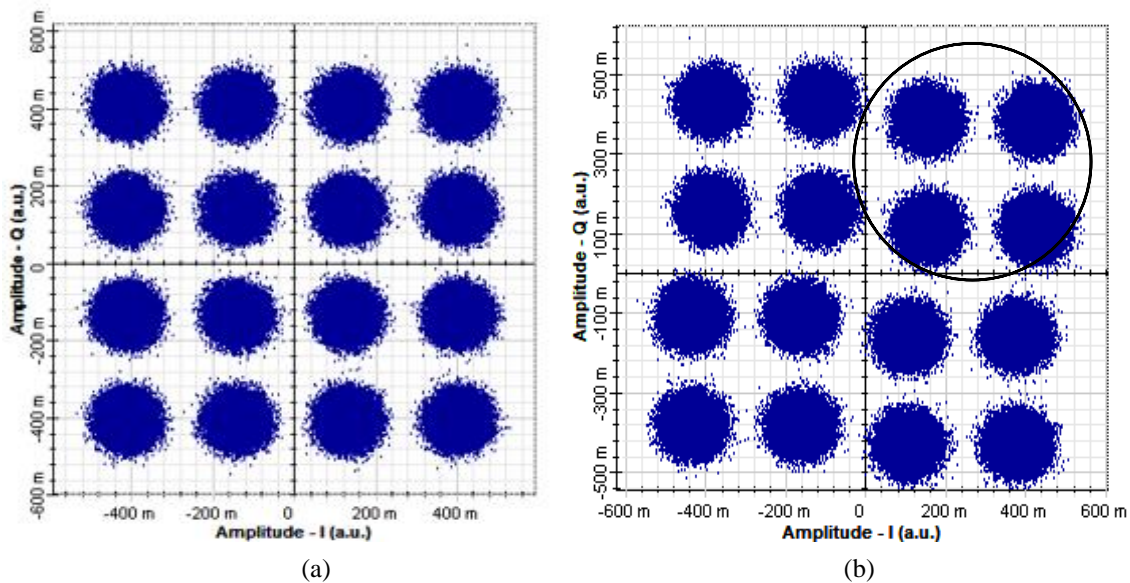


Fig. 5. 11: (a) proper 16-QAM constellation; (b) Symbol constellation at  $\Delta\phi_{16-QAM} = 5$  degrees.

Fig. 5.12 displays the BER versus  $\Delta\phi_{16-QAM}$  at 14.5 dB Eb/No. The graph shows that the BER reaches a minimum at zero phase errors and increases with the phase errors as

expected. It also indicates that a BER of  $10^{-4}$  can be achieved for phase errors of  $\pm 7$  degrees or less. The BER plots in Fig. 5.13 shows about 2 dB power penalty at  $10^{-4}$  for  $\Delta\phi_{16-QAM} = 7$  degrees.

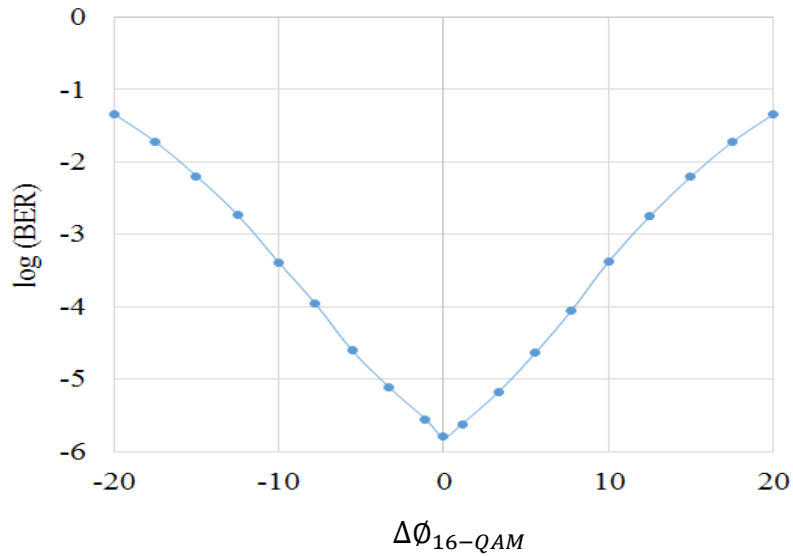


Fig. 5.12: BER versus phase error.

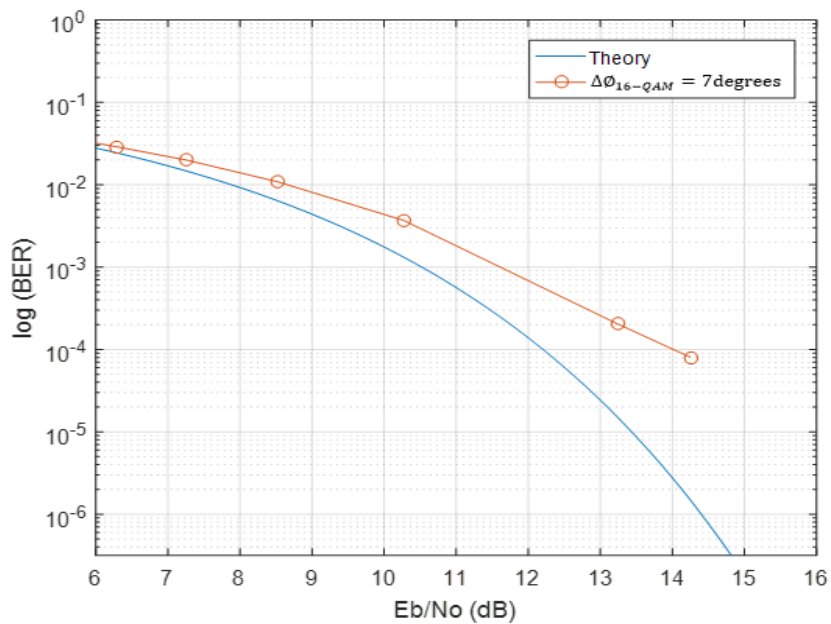


Fig. 5.13: BER performance.

### 5.3. 64-QAM simulation setup

The simulation setup for the 64-QAM transmitter is obtained by scaling the 16-QAM with another QPSK modulator in tandem as can be seen from Fig. 5.14. Similar to the 16-QAM, the precoder is implemented using mapping circuit and the output from the 64-QAM transmitter is applied to the quadrature hybrid demodulator of the coherent receiver operating under AWGN. The quadrature output is applied to I/Q threshold detector followed by 64-QAM symbol decoder. The binary output data are compared to the input data to determine the BER.

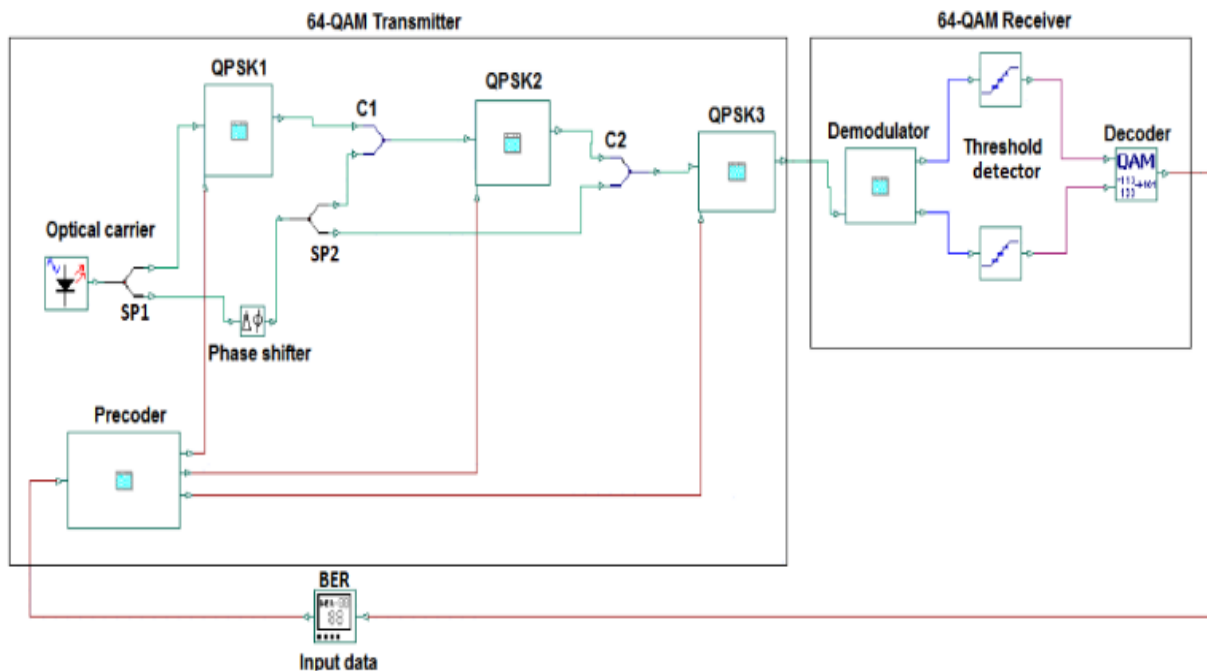


Fig. 5. 14: Simulation setup for 64-QAM transmitter.

#### 5.3.1. 64-QAM transmitter performance

The 64-QAM transmitter is designed with the assumption that  $\beta = 4.5$  dB,  $K = 3$  dB, and  $L = 1$  dB. We start the design by using (4.14) to find  $\alpha_2$  and then (4.10) to find  $\alpha_1$  as follows:

$$S2 = \frac{\alpha_2}{1 - \alpha_2} = \frac{1}{4} \left( \frac{1}{\beta L} \right) = \frac{1}{4} \left( \frac{1}{10^{-0.45} 10^{-0.1}} \right) = 0.887$$

Simplifying to

$$\alpha_2 = 0.887 - 0.887 \alpha_2 \rightarrow \alpha_2 = \frac{0.887}{1.887} = 0.47$$

Therefore, the coupling ratio of SP2 required for proper 64-QAM constellation is

$$S2 = \frac{\alpha_2}{1 - \alpha_2} = \frac{0.47}{0.53} = \frac{47}{53}$$

Now, the correct coupling ratios for S1 can be obtained from 4.10 as:

$$S1 = \frac{\alpha_1}{1 - \alpha_1} = \frac{1}{4} \left( \frac{\alpha_2 L K}{\beta} \right) = \frac{1}{4} \left( \frac{0.47 \times 10^{-0.1} \times 10^{-0.3}}{10^{-0.45}} \right) = 0.131$$

Simplifying to

$$\alpha_1 = 0.131 - 0.131 \alpha_2 \rightarrow \alpha_1 = \frac{0.131}{1.131} \approx 0.12$$

Therefore, the coupling ratio of SP1 required for proper 64-QAM constellation is

$$S1 = \frac{\alpha_1}{1 - \alpha_1} = \frac{0.12}{0.88} = \frac{12}{88}$$

The simulation setup in Fig. 5.14 is configured to reflect the values assumed in the example design.

Fig. 5.15 displays the results of the back-to-back simulation for the Gray coded 64-QAM constellation at 18 dB Eb/No. As can be seen, the resulting symbol constellation is proper

as expected. Also, the in-phase and quadrature eye diagrams are clear and uniform, reflecting the high quality of the generated 64-QAM signal as shown in Fig. 5.16.

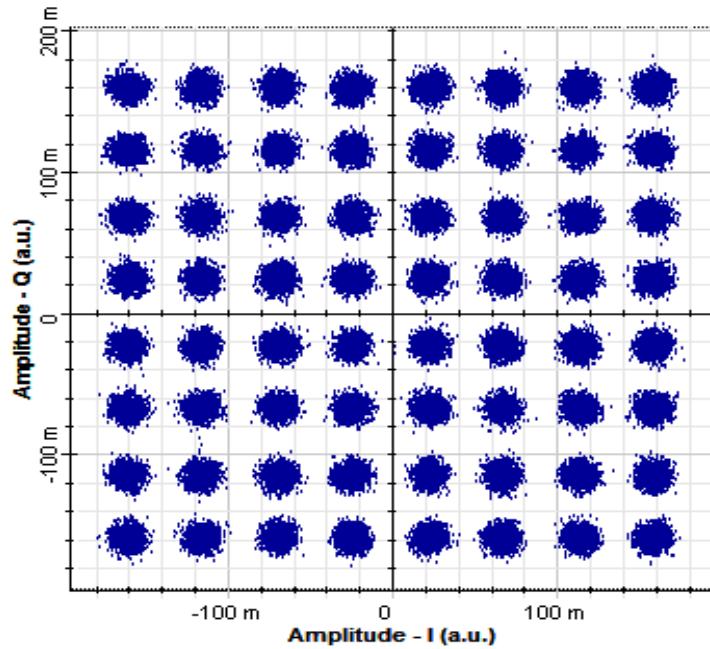


Fig. 5.15: 64-QAM constellation.

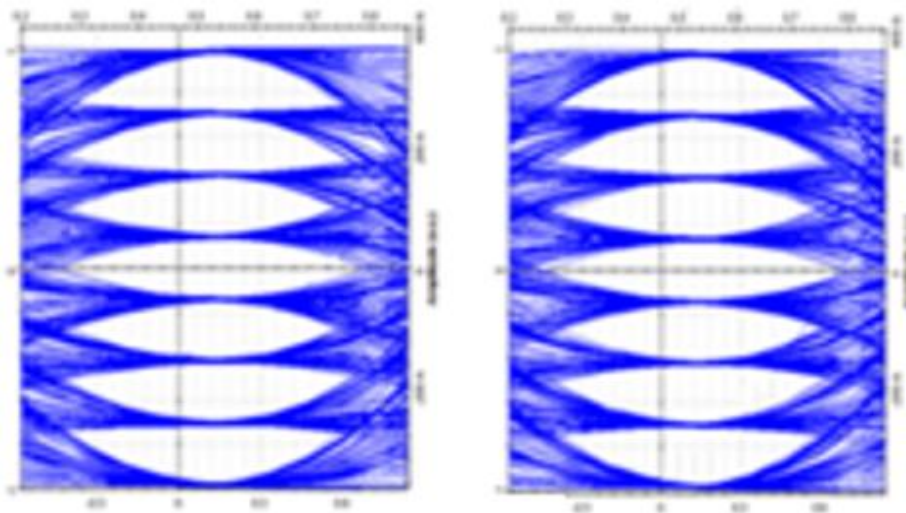


Fig. 5.16: I and Q eye diagrams.

Fig. 5.17 compares the BER performance of the proposed design to the theoretical 64-QAM. The BER plots show that the performance with the correct coupling ratios is identical to the theoretical expectations.

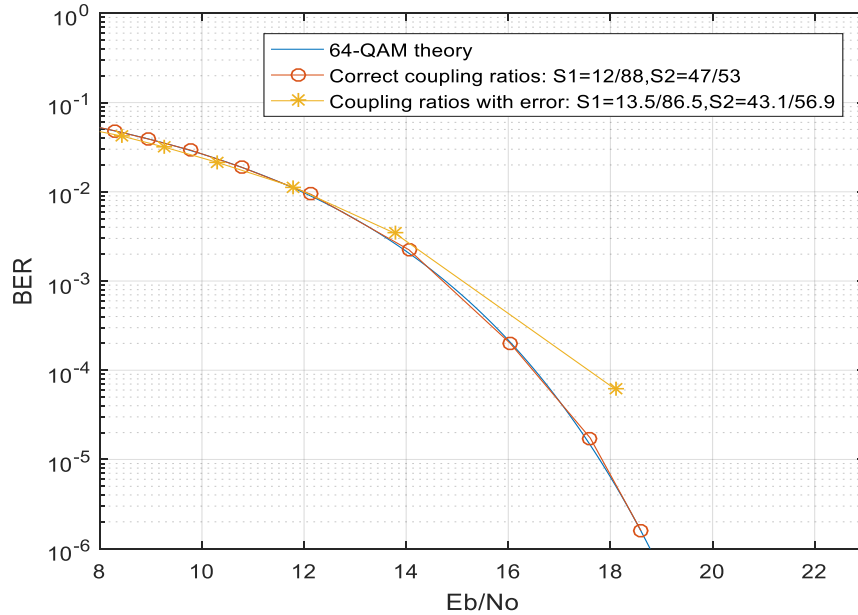


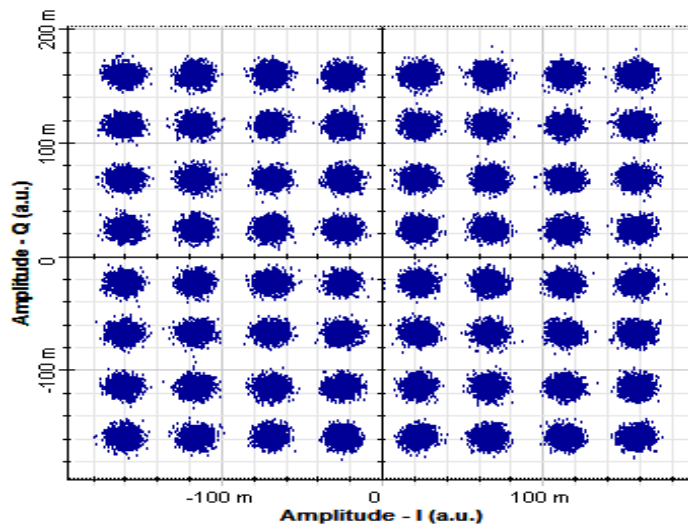
Fig. 5.17: BER performance.

### 5.3.2. Effect of coupling ratio errors on 64-QAM performance

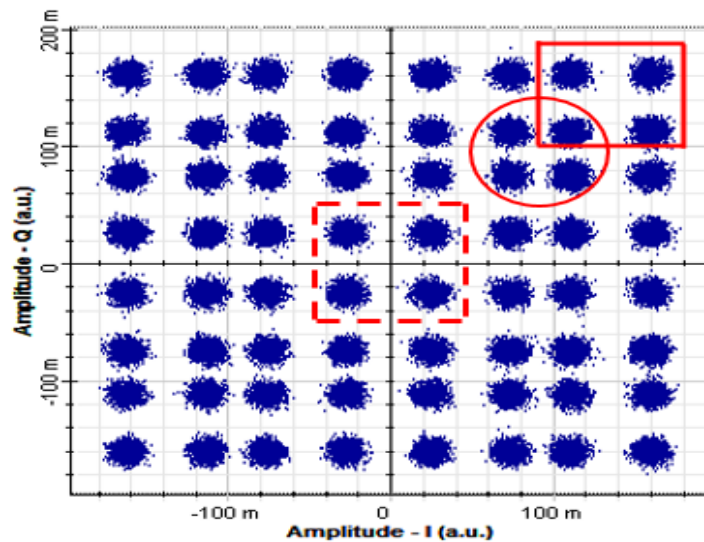
The plots in Fig. 5.17 shows that the transmitter BER performance has been degraded when the coupling ratios deviate from the correct ratio. In [88] for example, 10/90 and 50/50 couplers fabricated using SOI exhibited an average error of  $\pm 1.5\%$  and  $\mp 3.9\%$ , thus a coupling ratio of 11.5/88.5 and 46.1/53.9 respectively. Since the correct values for S1 and S2 in the above example design are close to 10/90 and 50/50, we assume that fabricating these couplers with SOI technology would result in similar tolerance:  $S1 = 12/88 \pm 1.5\%$  and  $S2 = 47/53 \mp 3.9\%$ . Therefore, the coupling ratio values for SP1 and SP2 would be

$S1=3.5/86.5$  and  $S2=43.1/56.9$  respectively, which correspond to  $\alpha_1 = 0.135$  and  $\alpha_2 = 0.431$ .

Fig. 5.17 displays the simulation results using these values [110]. The plots show that there is about 1 dB power penalty at  $10^{-4}$  BER due to the coupling ratio errors. Fig. 5.18 compares the 64-QAM constellations at 18 dB Eb/No. The improper symbol



(a)



(b)

Fig. 5. 18: Symbol constellation for (a)  $S1=12/88$ ,  $S2=47/53$ ; (b)  $S1=13.5/86.5$ ,  $S2=43.1/56.9$ .

constellation shown in Fig. 5.18b is due to the coupling errors. The clustering of the symbols in each quadrant is due to  $\alpha_1$  being higher than the correct value and  $\alpha_2$  being smaller than the correct value. For examples, the increase in  $P_2$  with  $\alpha_1$  expanded the QPSK symbols (e.g., inside the upper square in Fig. 5.18b). The corresponding reduction in  $P_3$  with  $(1 - \alpha_1)\alpha_2$  collapsed the 16-QAM symbols (e.g., inside the circle in Fig. 5.18b). At the same time,  $P_5$  remained fairly constant with  $(1 - \alpha_1)(1 - \alpha_2)$  and therefore there was no noticeable change in the symbols at the centre of the 64-QAM constellation (e.g., inside the dashed square).

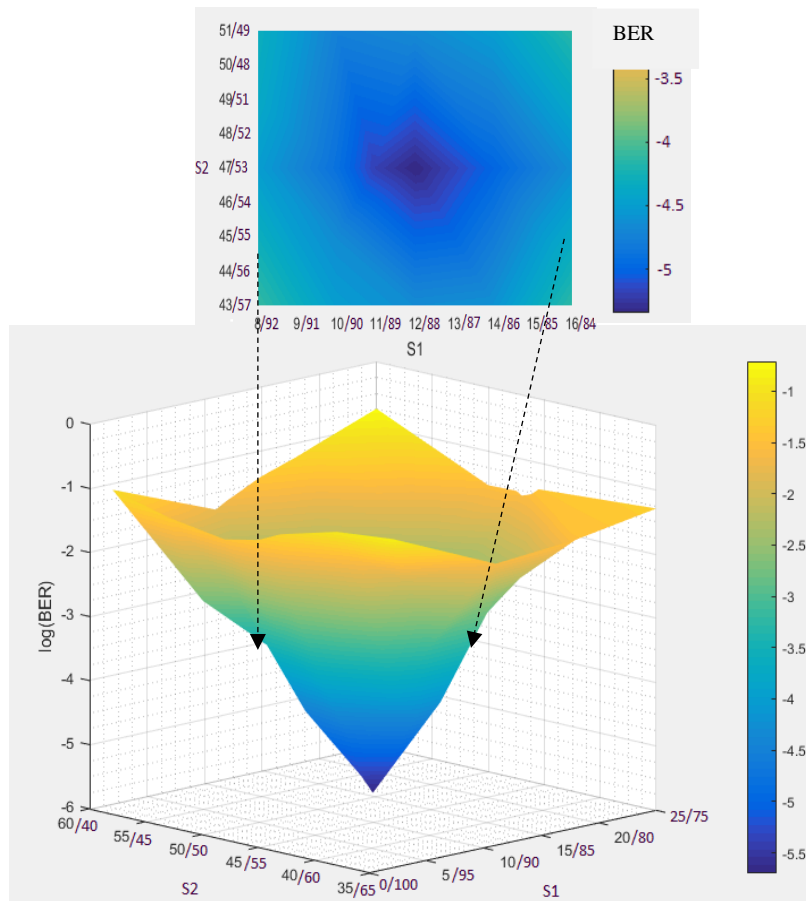


Fig. 5. 19: BER performance vs. S1 and S2; inset: coupling ratios for BER <  $10^{-4}$ .

Fig. 5.19 displays a 3D plot of the BER performance versus the coupling ratios, S1 and S2, at 18 dB Eb/No. The graph shows that the BER reaches a minimum at the correct coupling ratios and increases as they deviate from the correct values as expected. The color map inset indicates that un-coded BER better than the  $10^{-4}$  forward error correction (FEC) threshold can be achieved for coupling errors of 4% or less.

### 5.2.3. Effect of phase errors on 64-QAM performance

In order to obtain proper constellation from the 64-QAM transmitter, the phase shifts  $\Delta\phi_{16QAM}$  and  $\Delta\phi_{64-QAM}$  must be equal to zero as described in Chapter 4. Since this is not the case in practice, we study the effect of phase error on the BER performance.

Fig. 5.20 compares the 64-QAM constellations at 18 dB Eb/No for different values of phase errors. Compared to the error free constellation in Fig. 5.20a, the displacement of the QPSK symbols in Fig. 5.20b (dashed circle) is due to  $\Delta\phi_{16-QAM} = 5$  degrees that in turn distorts the 16-QAM symbols in each quadrant as well as the 64-QAM constellation. Similarly, the displacements of the 16-QAM symbols in Fig. 5.20c (dashed square) is due to  $\Delta\phi_{64-QAM} = 5$  degrees which in turn distorts the 64-QAM constellation. While  $\Delta\phi_{16-QAM}$  causes rotation of the 16-QAM in each quadrant around the quadrant center,  $\Delta\phi_{64-QAM}$  causes rotation around the 64-QAM constellation center and therefore the same distortion pattern is obtained. The presence of both  $\Delta\phi_{16-QAM}$  and  $\Delta\phi_{64-QAM}$  would worsen the effects of phase errors as can be seen in Fig. 5.20d where  $\Delta\phi_{16-QAM} = \Delta\phi_{64-QAM} = 5$  degrees.

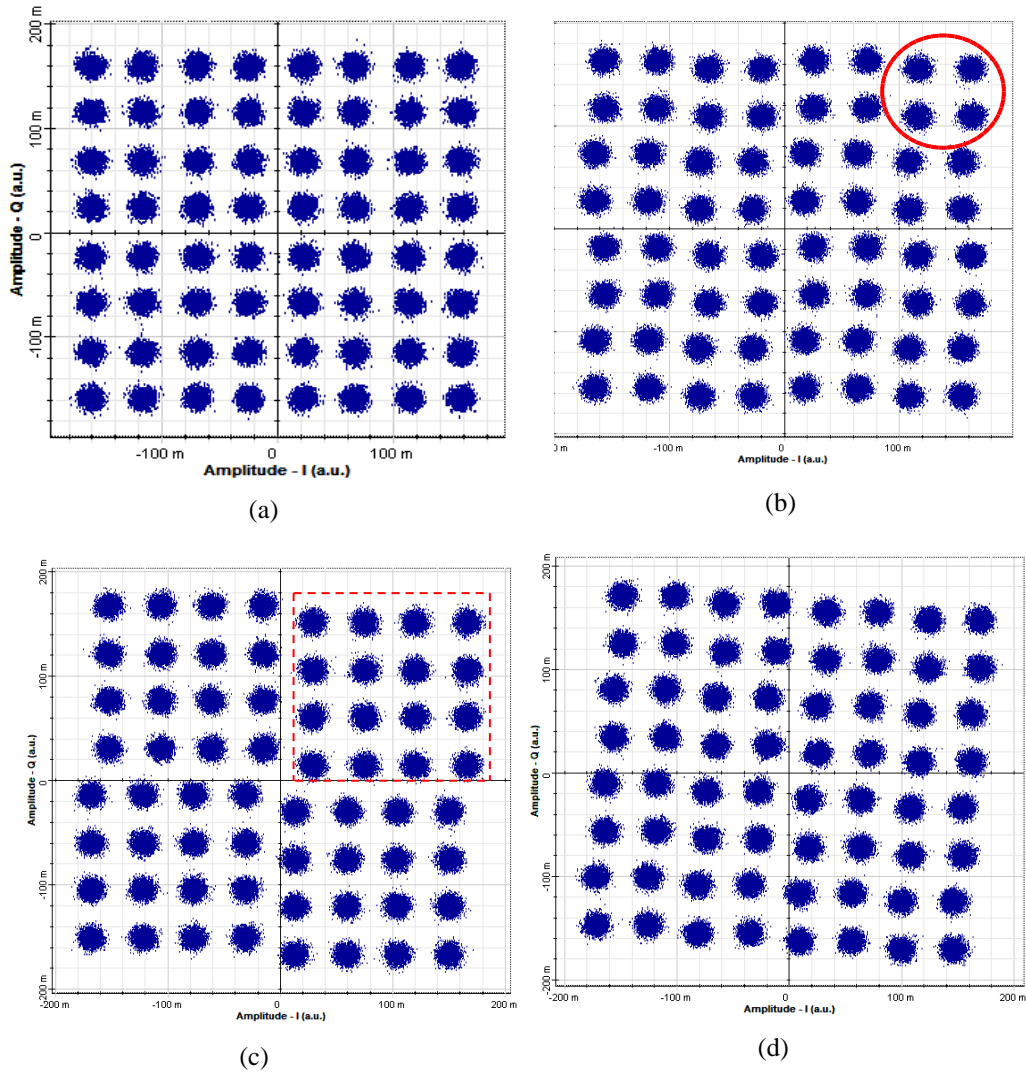


Fig. 5.20: 64-QAM constellation for: (a) No phase errors; (b)  $\Delta\phi_{16-QAM} = 5$  degrees; (c)  $\Delta\phi_{64-QAM} = 5$  degree; (d)  $\Delta\phi_{16-QAM} = \Delta\phi_{64-QAM} = 5$  degrees.

Fig. 5.21 displays a 3D plot of the BER versus  $\Delta\phi_{16-QAM}$  and  $\Delta\phi_{64-QAM}$  at 18 dB Eb/No.

The graph shows that the BER reaches a minimum at zero phase errors and increases with the phase errors as expected. The color map inset indicates that a BER of  $10^{-4}$  can be achieved for phase errors of  $\pm 2$  degrees or less. The BER plots in Fig. 5.22 show about 1 dB power penalty at  $10^{-4}$  for  $\Delta\phi_{16-QAM} = \Delta\phi_{64-QAM} = 2$  degrees.

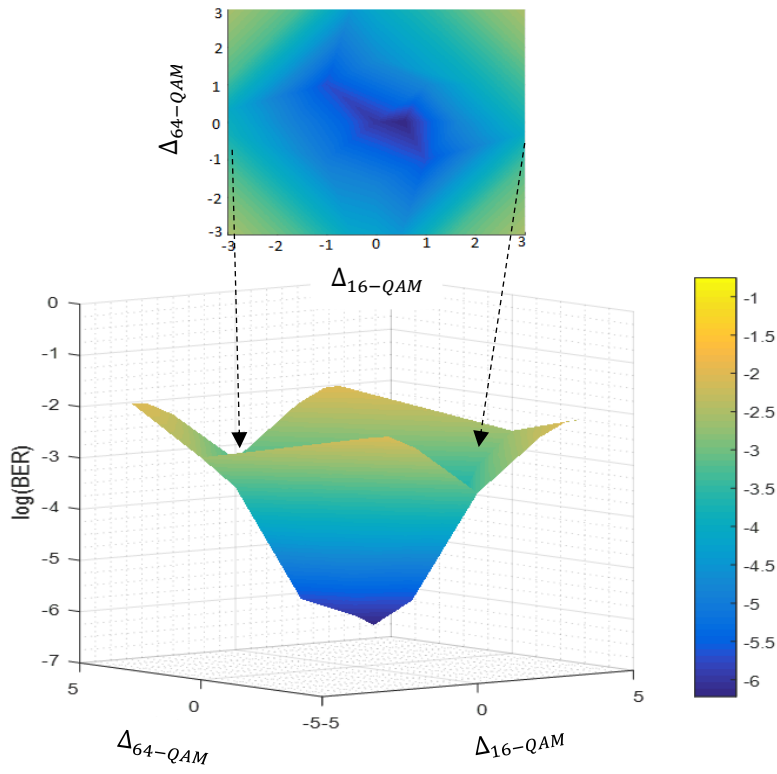


Fig. 5.21: BER performance vs.  $\Delta\theta_{16-QAM}$  and  $\Delta\theta_{64-QAM}$ ; inset: Phase errors for BER  $< 10^{-4}$ .

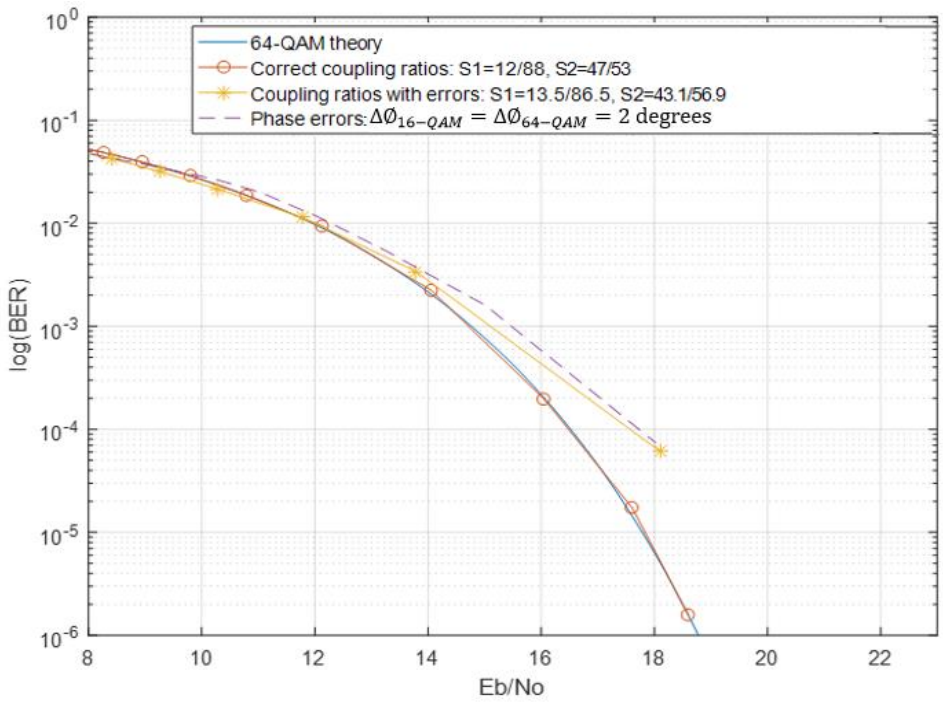


Fig. 5.22: BER performance.

#### 5.4. Conclusion

We analyzed the design and performance of a binary driven 16-QAM and 64-QAM optical transmitters. An example design demonstrated BER performance that was similar to the theoretical expectations. An analysis of the effect of coupling ratio errors as well as phase errors on the performance and constellation diagrams has been investigated. For 16-QAM, the simulation results under presence of additive white Gaussian noise (AWGN) demonstrated BER better than  $10^{-4}$  and power penalty of about 2 dB for coupling ratio errors less than 10 % or phase errors within  $\pm 7$  degrees. 64-QAM transmitter on the other hand demonstrated BER better than  $10^{-4}$  and power penalty of about 1 dB for coupling ratio errors less than 4% or phase errors within  $\pm 2$  degrees.

## CHAPTER 6: CONCLUSION

Coherent optical transmission refers to optical communication systems that apply higher order modulation format at the transmitter side and coherent detection using local oscillator laser and digital signal processing (DSP) at the receiver side. Using higher order modulation format such as M-ary QAM would allow better utilization of fiber bandwidth thus reduce the cost per bit of transmitted information. In this work, we have proposed scalable coherent optical M-ary QAM transmitter using tandem QPSK modulators driven by binary electrical signals. The main distinctive characteristics of the proposed design are as follows:

- **No need for DACs**

The proposed optical transmitters apply tandem QPSK modulators that are driven by binary electrical signals, thus eliminating the need for DACs. This allows less restriction on the linearity of both the driving amplifiers and the MZMs. Consequently, equally spaced high-quality symbol constellation can be generated by biasing each QPSK modulator in push-pull configuration resulting in linear transitions between the symbols and high quality eye diagrams.

- **Scalability**

The proposed design could be scaled on demand to accommodate the traffic growth by simply adding more QPSK modulators in tandem. Increasing the data rate of QPSK by twofold could be achieved using 16-QAM. Generating 16-QAM signal would require two QPSK modulators in tandem; each generates 4 symbols, therefore the overall number of symbols generated in this case is  $4 \times 4 = 16$  as required. Accordingly, increasing the data rate

of QPSK by three or fourfold would require using 64-QAM and 256-QAM, which can be realized using 3 and 4 QPSK modulators in tandem respectively.

- **Noise tolerant**

The design uses Gray coding where any two adjacent symbols differ in only one bit. This efficient coding would combat the noise generated by the nonlinear optical channel impairments as well as the phase noise of the optical carrier, insuring the lowest bit error rate possible during symbol recovery.

We provided the design of the coupling ratios required for a proper 16-QAM and 64-QAM constellations considering the insertion loss of the optical components. Example designs have been simulated at 50 Gbauds using OptiSystem, and demonstrated high quality signal constellations and eye diagrams. It also has demonstrated BER performance similar to the theoretical expectations. We also analyzed the transmitter and evaluated its BER performance under presence of coupling and phase errors. We found that the errors would cause constellation distortion and degradation to the BER performance. For 16-QAM, The simulation results under presence of AWGN demonstrated BER better than  $10^{-4}$  and power penalty of about 2 dB for coupling ratio errors less than 10 % or phase errors within  $\pm 7$  degrees. 64-QAM transmitter on the other hand demonstrated BER better than  $10^{-4}$  and power penalty of about 1 dB for coupling ratio errors less than 4% or phase errors within  $\pm 2$  degrees. The presented performance analysis can be extended to higher-order modulation format such as 256-QAM and 1024-QAM.

It is worthwhile to notice that the proposed transmitter only uses binary data and that restricts any type of signal conditioning which is common for spectral shaping since it is

necessary that the QPSK modulators be driven with non-square waveforms. While the single, multi-level I/Q modulator performs signal conditioning (e.g. by filtering) on the modulation waveforms for the in-phase and quadrature symbols, the proposed transmitter would perform signal conditioning on each of the (cascaded) QPSK symbol modulation waveforms that correspond to every 2 bits. As an example, for 16-QAM the 2 least significant bits of the symbol would condition the first QPSK modulator and the 2 most significant bits of the symbol would condition the second QPSK modulator. So, while the signal conditioning approach differs, we would expect the proposed transmitter to achieve symbol waveform shaping similar to the multi-level I/Q modulator. This is an intriguing subject for future work because the ability to perform signal conditioning independently on every 2 bits of a QAM symbol may bring about certain flexibilities and advantages.

This work has been published in multiple conferences and journals as follows:

Material in Chapter 3 was published in the Frontiers in Optics, Optical Society of America conference, and IEEE Avionics and Vehicle Fiber-Optics and Photonics conference:

- N. A. Albakay and L. Nguyen, "Scalable and Gray-coded optical M-ary QAM using QPSK modulators with binary electronic driving signals." Frontiers in Optics, Optical Society of America, USA, Oct. 2016.
- N. A. Albakay and L. Nguyen, "Square QAM transmitter using QPSK modulators driven by binary electrical signals." IEEE Avionics and Vehicle Fiber-Optics and Photonics Conference, USA, Nov. 2016.

Material in Chapter 4 was published in the Journal of Electronics Letters, as well as in Frontiers in Optics, Optical Society of America conference, and IEEE Avionics and Vehicle Fiber-Optics and Photonics Conference:

- N. A. Albakay and L. Nguyen, "Optical 64-QAM transmitter using binary driven QPSK modulators" *Journal of Electronics Letters*. Apr. 2017.
- N. A. Albakay and L. Nguyen, "Coupling ratios design and their impact on the performance of binary driven QAM transmitters." IEEE Avionics and Vehicle Fiber-Optics and Photonics Conference, USA, Nov. 2017.
- N. A. Albakay and L. Nguyen, " Designing the coupling ratios in a binary driven 64-QAM transmitter" Frontiers in Optics, Optical Society of America, USA, Sep. 2017.

Material in Chapter 5 was published in the IEEE Journal of Lightwave technology:

- N. A. Albakay and L. Nguyen, "Design and performance analysis for a binary driven QAM transmitter," *IEEE Journal of Lightwave Technology*, July 2018.

## REFERENCES

- [1]. DeLange, Owen E. "Wide-band optical communication systems: Part II—frequency-division multiplexing." *Proceedings of the IEEE*, Oct 1970.
- [2]. Okoshi T., and Kikuchi K. "Frequency stabilization of semiconductor lasers for heterodyne-type optical communication systems." *Electronics letters*, Feb 1980.
- [3]. Okoshi T., Kikuchi K, et al. "Computation of bit-error rate of various heterodyne and coherent-type optical communication schemes." *Journal of optical communications*, Sep 1981.
- [4]. Henry, and Charles. "Theory of the linewidth of semiconductor lasers." *Journal of quantum electronics*, Feb 1982.
- [5]. Yamamoto, and Yoshihisa. "Receiver performance evaluation of various digital optical modulation-demodulation systems in the 0.5-10  $\mu\text{m}$  wavelength region." *Journal of quantum electronics*, Nov 1980.
- [6]. Aspell, J., and Neal S. "Erbium doped fiber amplifiers for future undersea transmission systems." *Journal of quantum electronics*, Nov 1990.
- [7]. ITU Recommendation. "G. 694.1: Spectral grids for WDM applications: DWDM frequency grid." International telecommunications union, Feb 2002.
- [8]. Wu M., and Winston W. "Fiber nonlinearity limitations in ultra-dense WDM systems." *Journal of lightwave technology*, Jun 2004.
- [9]. Mizuochi, Takashi, et al. "A comparative study of DPSK and OOK WDM transmission over transoceanic distances and their performance degradations due to nonlinear phase noise." *Journal of lightwave technology*, Jun 2003.
- [10]. Kahn, Joseph M., and Keang P. "Spectral efficiency limits and modulation/detection techniques for DWDM systems." *Journal of selected topics in quantum electronics*, Mar 2004.
- [11]. Louchet, H., Anes H., and Klaus P. "Analytical model for the performance evaluation of DWDM transmission systems." *Photonics technology letters*, Sep 2003.
- [12]. Leng, L., Stulz, S., et al. "1.6-Tb/s (160 x 10.7 Gb/s) transmission over 4000 km of nonzero dispersion fiber at 25-GHz channel spacing." *Photonics technology letters*, Aug 2003.
- [13]. Van D., Jansen S., et al. "1.6-b/s/Hz spectrally efficient 40x 85.6-Gb/s transmission over 1,700 km of SSMF using POLMUX-RZ-DQPSK." Optical fiber communication conference, Mar 2006.
- [14]. Lizé, Yannick Keith, et al. "Simultaneous and independent monitoring of OSNR, chromatic and polarization mode dispersion for NRZ-OOK, DPSK and duo binary." Optical society of America conference, Mar 2007.
- [15]. Ehrhardt, A., Breuer, D., et al. "Field trial to upgrade an existing 10 Gbit/s DWDM link by 40 Gbit/s RZ-DQPSK channels." Transparent optical networks conference, Jun 2007.
- [16]. Watts, P. M., Waegemans, R. et al. "An FPGA-based optical transmitter using real-time DSP for implementation of advanced signal formats and signal predisortion." Optical communications conference, Sep 2006.
- [17]. Raybon, Greg, and Peter J. Winzer. "100 Gb/s challenges and solutions." Optical fiber communication/national fiber optic engineers conference, Feb. 2008.
- [18]. Tkach, Robert W. "Scaling optical communications for the next decade and beyond." *Bell labs technical journal*, Mar 2010.
- [19]. Winzer, Peter J. "High-spectral-efficiency optical modulation formats." *Journal of lightwave technology*, Dec 2012.
- [20]. Miyamoto, Y., et al. "Ultrahigh-capacity digital coherent optical transmission technology." *Nippon telegraph and telephone technical review*, Jan. 2012.
- [21]. Infinera. "Coherent WDM technologies." white paper, Jun 2016.
- [22]. Kikuchi, Kazuro. "Fundamentals of coherent optical fiber communications." *Journal of lightwave technology*, Jan 2016.

- [23]. Kikuchi, Kazuro. "Coherent optical communications: Historical perspectives and future directions." Springer Berlin Heidelberg, 2010.
- [24]. Reis, J., et al. "Technology options for 400G implementation." Optical internetworking forum white paper, Jul 2015.
- [25]. Savory, Seb J. "Digital signal processing for multilevel modulation formats." European conference on optical communication, Dec 2016.
- [26]. Berenguer, Pablo W., et al. "Nonlinear digital pre-distortion of transmitter components." *Journal of lightwave technology*, Apr 2016.
- [27]. Carena A., Jiang Y., et al. "Electronic dispersion pre-compensation in PM-QPSK systems over mixed-fiber links." The European conference on optical communication, Jan. 2014.
- [28]. Shen, T., Shun R., and Alan P. "Fiber nonlinearity compensation using extreme learning machine for DSP-based coherent communication systems." Opto-electronics and communications conference, Jul 2011.
- [29]. Ezra I., "Nonlinear compensation using backpropagation for polarization-multiplexed transmission." *Journal of lightwave technology*, Mar 2010.
- [30]. Rozental, Valery N., et al. "Digital-domain chromatic dispersion compensation for different pulse shapes: Practical considerations." Microwave and optoelectronics conference, Nov 2015.
- [31]. Mastropaolo, A. "On real-time implementation of 400 Gbps dual polarization 16-QAM coherent intradyne receiver." International conference on photonics in switching, Sep 2015.
- [32]. Cai, J.X., Zhang, H. , et al. "200 Gb/s and dual wavelength 400 Gb/s transmission over transpacific distance at 6.0 b/s/Hz spectral efficiency." *Journal of lightwave technology*, Feb 2014.
- [33]. Lavigne, B. "400Gb/s trials on commercial systems using real-time bit-rate-adaptive transponders for next generation networks." Optical fiber communication conference, Mar 2015.
- [34]. Torres, P., Gutiérrez, R., and Tomkos, I. "Multi-format 800–1600 Gb/s coherent transceiver for inter-data center interconnects over SMF." Transparent optical networks conference, Jul 2017.
- [35]. <http://www.ciena.com/insights/what-is/What-Is-Coherent-Optics.html>
- [36]. Akulova, A. "Advances in integrated widely tunable coherent transmitters." Optical fiber communication conference, Mar 2016.
- [37]. Koos, C., Vorreau, Koos, Christian, et al. "All-optical high-speed signal processing with silicon–organic hybrid slot waveguides." *Nature photonics journal*, Apr 2009.
- [38]. Berenguer, P. Wilke, et al. " Nonlinear digital pre-distortion of transmitter components." Optical communication European conference, Mar 2015.
- [39]. A. Carena, Y. Jiang, P. Poggiolini, G. Bosco, V. Curri and F. Forghieri, "Electronic dispersion pre-compensation in PM-QPSK systems over mixed-fiber links." European conference on optical communication, Jan 2014.
- [40]. Huang, Y., and Wu, D. "Nonlinear internal model control with inverse model based on extreme learning machine." Electric information and control engineering, May 2011.
- [41]. Shen, T., Shun, R., and Alan P. "Fiber nonlinearity compensation using extreme learning machine for DSP-based coherent communication systems." Opto-electronics and communications conference, Jul 2011.
- [42]. Ip, Ezra. "Nonlinear compensation using backpropagation for polarization-multiplexed transmission." *Journal of lightwave technology*, Mar 2010.
- [43]. Rozental, N., et al. "Digital-domain chromatic dispersion compensation for different pulse shapes: Practical considerations." Microwave and optoelectronics conference, Nov 2015.
- [44]. Laperle, Charles. "Advances in high-speed ADCs, DACs, and DSP for optical transceivers." Optical fiber communication conference and exposition and the national fiber optic engineers conference, Mar 2013.
- [45]. Schmogrow, R., et al. "150 Gbit/s real-time Nyquist pulse transmission over 150 km SSMF enhanced by DSP with dynamic precision." Optical fiber communication conference, Mar 2012.

- [46]. Châtelain, B., et al. "A family of Nyquist pulses for coherent optical communications." *Optics express*, Apr 2012.
- [47]. Xie, C., and Greg R. "Digital PLL based frequency offset compensation and carrier phase estimation for 16-QAM coherent optical communication systems." European conference and exhibition on optical communication, Sep 2012.
- [48]. Ferreira, Ricardo M., et al. "Optimized carrier frequency and phase recovery based on blind Mth power schemes." *Photonics technology letters*, Nov 2016.
- [49]. Savory, Seb J. "Digital coherent optical receivers: algorithms and subsystems." *Journal of selected topics in quantum electronics*, Sep 2010.
- [50]. Taylor, Michael G. "Phase estimation methods for optical coherent detection using digital signal processing." *Journal of lightwave technology*, Apr 2009.
- [51]. Ip, Ezra, and Joseph M. Kahn. "Feedforward carrier recovery for coherent optical communications." *Journal of lightwave technology*, Sep 2007.
- [52]. Sakaguchi, J., Yoshinari, A., and Naoya W. "Seed lightwave distribution over 1600 km for 64QAM-based coherent WDM optical networks with low DSP-complexity." European conference on optical communication, Dec 2016.
- [53]. Winzer, Peter J. "Scaling optical fiber networks: challenges and solutions." *Optics and photonics news*, Mar 2015.
- [54]. Winzer, Peter J. "High-spectral-efficiency optical modulation formats." *Journal of lightwave technology*, Dec 2012.
- [55]. Nakazawa, M., Hirooka, T., et al. "Ultrafast coherent optical transmission." *Journal of selected topics in quantum electronics*, 2012.
- [56]. Pincemin, Erwan, et al. "Challenges of 40/100 Gbps and higher-rate deployments over long-haul transport networks." *Optical fiber technology journal*, Oct 2011.
- [57]. Infinera. "Coherent WDM technologies." white paper, Jun. 2016.
- [58]. Gnauck, A., et al. "Spectrally efficient long-haul WDM transmission using 224-Gb/s polarization-multiplexed 16-QAM." *Journal of lightwave technology*, Feb 2011.
- [59]. Mitchell, Matthew, et al. "Optical integration and multi-carrier solutions for 100G and beyond." *optical fiber technology letters*, Oct 2011.
- [60]. Bennett, G., et al. "A review of high-speed coherent transmission technologies for long-haul DWDM transmission at 100G and beyond." *Communications magazine*, Oct 2014.
- [61]. Yang, Q., Abdullah, A., and William S. "Optical OFDM basics." Springer New York, 2011.
- [62]. Prasad, R. "OFDM for wireless communications systems." Artech house, 2004.
- [63]. Sun, H., Kuang, W., and Kim R. "Real-time measurements of a 40 Gb/s coherent system." *Optics express*, Jan 2008.
- [64]. Ma, Y., et al. "1-Tb/s single-channel coherent optical OFDM transmission over 600-km SSMF fiber with subwavelength bandwidth access." *Optics express*, May 2009.
- [65]. Shieh, W. "OFDM for flexible high-speed optical networks." *Journal of lightwave technology*, May 2011.
- [66]. Hsu, C., Chow, W., and Yeh, H. "Cost-effective direct-detection all-optical OOK-OFDM system with analysis of modulator bandwidth and driving power." *Photonics journal*, Aug 2015.
- [67]. Sakamoto, T., Guo, L., and Naokatsu, Y. "Full-channel parallel measurement of 4x20-Gb/s all-optical OFDM signals by using loop-assisted coherent matched detector." European conference on optical communication, Sep 2016.
- [68]. Chandrasekhar, S., et al. "Transmission of a 1.2-Tb/s 24-carrier no-guard-interval coherent OFDM super channel over 7200-km of ultra-large-area fiber." European conference on optical communication, Jan 2009.
- [69]. Hillerkuss, D., et al. "Single source optical OFDM transmitter and optical FFT receiver demonstrated at line rates of 5.4 and 10.8 Tbit/s." Optical fiber communication conference, Mar 2010.

- [70]. Armstrong, J. "Peak-to-average power reduction for OFDM by repeated clipping and frequency domain filtering." *Electronics letters*, Feb 2002.
- [71]. Nazarathy, M., et al. "Phased-array cancellation of nonlinear FWM in coherent OFDM dispersive multi-span links." *Optics express*, Sep 2008.
- [72]. Dischler, R., and Fred B. "Measurement of nonlinear thresholds in O-OFDM systems with respect to data pattern and peak power to average ratio." European conference on optical communication, Sep 2008.
- [73]. Buyankhishig, Z., Tserenlkham, B., and Orgil, J. "Comparative study on high order optical modulation formats." *Strategic technology journal*, Jun 2013.
- [74]. Barbieri, A., et al. "OFDM versus single-carrier transmission for 100 Gbps optical communication." *Journal of Lightwave Technology*, Sep. 2010.
- [75]. Cvijetic, N. "OFDM for next-generation optical access networks." *Journal of Lightwave Technology*, Feb 2012.
- [76]. Gnauck, A., et al. "Generation and transmission of 21.4-Gbaud PDM 64-QAM using a novel high-power DAC driving a single I/Q modulator." *Journal of lightwave technology*, Feb 2012.
- [77]. Sowailam, M., et al. "400-G Single carrier 500-km transmission with an InP dual polarization IQ Modulator." *Photonics technology letters*, Feb 2016.
- [78]. Yamazaki, H., et al. "Optical modulator with a near-linear field response." *Journal of lightwave technology*, Aug 2016.
- [79]. Lu, Guo-Wei, Takahide Sakamoto, and Tetsuya Kawanishi. "Flexible high-order QAM transmitter using tandem IQ modulators for generating 16/32/36/64-QAM with balanced complexity in electronics and optics." *Optics express*, Mar 2013.
- [80]. Fresi, F., et al. "Reconfigurable silicon photonics integrated 16-QAM modulator driven by binary electronics." *Journal of selected topics in quantum electronics*, Nov 2016.
- [81]. Lu, Guo-W. et al. "40-Gbaud 16-QAM transmitter using tandem IQ modulators with binary driving electronic signals." *Optics express*, Oct 2010.
- [82]. Fresi, F., et al. "Versatile low-complex 16-QAM optical transmitter driven by binary signals." Globecom workshops, Dec 2012.
- [83]. Silfvast, T. "Laser fundamentals". Cambridge university press, 2004.
- [84]. Hitz, C. Breck, J and Jeff H. "Introduction to laser technology". John Wiley & Sons, 2012.
- [85]. Paschotta, R. Telle, H. and Kelle, U. "Solid-state lasers and applications." CRC Press, 2007.
- [86]. Kikuchi, K., et al. "Degradation of bit-error rate in coherent optical communications due to spectral spread of the transmitter and the local oscillator." *Journal of lightwave technology*, Dec 1984.
- [87]. Peucheret, C. "Direct and external modulation of light." Technical university of denmark, Nov 2009.
- [88]. Djordjevic, I., William R., and Bane V. "Fundamentals of optical communication." Springer, 2010.
- [89]. Morichetti, A. Canciamilla, et al, "Roughness induced backscattering in optical silicon waveguides," *Physical review letters*, Jan 2010.
- [90]. Agrell, E., et al. "Gray coding for multilevel constellations in Gaussian noise." *IEEE Transactions on Information theory*, Jan 2007.
- [91]. [https://www.lasercomponents.com/de/?embedded=1&file=fileadmin/user\\_upload/home/Datasheets/lc/applikationsreport/ixblue/introduction-to-modulator-bias-controllers.pdf&no\\_cache=1](https://www.lasercomponents.com/de/?embedded=1&file=fileadmin/user_upload/home/Datasheets/lc/applikationsreport/ixblue/introduction-to-modulator-bias-controllers.pdf&no_cache=1)
- [92]. Kawanishi, T., Sakamoto, T., et al, "Ultra high extinction-ratio and ultra-low chirp optical intensity modulation for pure two-tone lightwave signal generation," Lasers and electro-optics conference on quantum electronics and laser science, May 2008.
- [93]. Svarny, J. "Bias driver of the Mach-Zehnder intensity electro-optic modulator, based on harmonic analysis." Advances in robotics, mechatronics and circuits, Mar 2014.

- [94]. Fu, Y., Zhang, X. et al, "Mach-Zehnder: a review of bias control techniques for Mach-Zehnder Modulators in photonic analog links," *Microwave magazine*, Nov 2013.
- [95]. <http://ece466.groups.et.byu.net/notes/smf28.pdf>.
- [96]. [http://www.thefoa.org/tech/ref/testing/test/CD\\_PMD.html](http://www.thefoa.org/tech/ref/testing/test/CD_PMD.html).
- [97]. <https://www.exfo.com/en/> "Pocket guide for chromatic dispersion at high bit rate".
- [98]. <https://www.exfo.com/en/> "Pocket guide for PMD Issues in advanced very high-speed networks".
- [99]. Gregory L., "Testing polarization mode dispersion (PMD) in the field", JDSU, 2006.
- [100]. Laperle C., O'Sullivan M." Advances in high-speed DACs, ADCs, and DSP for optical coherent transceivers." *Journal of lightwave technology*, Feb 2014.
- [101]. Zhou X, Yu J. "Digital signal processing for coherent optical communication." Wireless and optical communications conference, May 2009.
- [102]. Yamazaki E, Tomizawa M, Miyamoto Y. "100-Gb/s optical transport network and beyond employing digital signal processing." *IEEE communications magazine*, Feb 2012.
- [103]. Roberts K, Beckett D., et al. "100G and beyond with digital coherent signal processing." *IEEE Communications magazine*, Jul 2010.
- [104]. Yamazaki, H., Goh, T., et al. "Flexible-format modulator with a lattice configuration", *Journal of selected topics in optical quantum electronics*, Jul 2013.
- [105]. Albakay N., and Nguyen L., "Square QAM transmitter using QPSK modulators driven by binary electrical signals," Avionics and vehicle fiber-optics and photonics conference, Nov 2016.
- [106]. Albakay N., and Nguyen L., "Scalable and Gray-coded optical M-ary QAM Using QPSK modulators with binary electronic driving signals," *Frontiers in optics*, optical society of America, paper JW4A.2, Oct 2016
- [107]. Albakay N., and Nguyen L., "Optical 64-QAM transmitter using binary driven QPSK modulators," *Electronics Letters journal*, Apr 2017.
- [108]. Albakay N., and Nguyen L., "Designing the coupling ratios in a binary driven 64-QAM transmitter," *Frontiers in optics*, optical society of America, Sep 2017.
- [109]. Albakay N., and Nguyen L., "Coupling ratios design and their impact on the performance of binary driven QAM transmitters," Avionics and vehicle fiber-optics and photonics conference, Nov 2017.
- [110]. Albakay N., and Nguyen L., "Design and performance analysis for a binary-driven QAM transmitter," *Journal of lightwave technology*, Nov 2018.